A Study of Nuclear Fragmentation at Intermediate Energies

by

HIN HARK GAN

A Thesis submitted to the Faculty of Graduate Studies and Research of McGill University in partial fulfillment of the requirements for the degree of Doctor of Philosophy.

Department of Physics
McGill University
Montréal, Québec
Canada

March 1989

To my parents

献给我的父母

Abstract

The model of nuclear dynamics according to the Boltzmann-Uehling-Uhlenbeck (BUU) equation which incorporates fluctuations is presented. This model is employed to calculate heavy-ion reactions in the intermediate energy regime ($20 \leq E_{lab}/A \leq 200 MeV$). Using a local (Skyrme-type) interaction, the model is capable of reproducing diverse features of spectator and participant observables. A finite range interaction is introduced to generate diffuse nuclear surfaces in the Vlasov approach. The peripheral reaction of ^{40}Ar on ^{27}Al is calculated with this interaction. Characteristic features of the angular distribution of the projectile-like fragments and its correlation with the target-like fragments are in agreement with experiments.

The stability condition of self-consistent Vlasov solutions with a finite range interaction is derived. This condition is cast into an eigenvalue equation. The lowest eigenmodes correspond closely to giant vibration modes. The relationship of these eigenmodes to the time-dependent Vlasov equation is explored.

Résumé

Un modèle dynamique nucléaire incorporant des fluctuations, basé sur l'équation de Boltzmann-Uehling-Uhlenbeck (BUU) est présenté. Ce modèle est employé afin de calculer des réactions d'ions lourds dans un régime d'énergie intermédiaire ($20 \leq E_{lab}/A \leq 200 MeV$). A l'aide d'une interaction locale (de type Skyrme), ce modèle est en mesure de reproduire les divers éléments des observables de spectateur et de participant. Une interaction de portée finie est introduite afin de générer des surfaces nucléaires diffuses dans l'approche de Vlasov. La réaction périphérique $^{10}Ar + ^{27}Al$ est calculée à l'aide de cette interaction. Les traits caractéristiques de la distribution angulaire des fragments de type projectile et sa corrélation avec les fragments de type cible sont en accords avec les résultats expérimentaux.

La condition de stabilité des solutions self-consistantes de Vlasov avec une interaction de portée finie est dérivée. Cette condition est reformulée en un problème à valeurs propres. Les vecteurs propres correspondants aux plus petites valeurs propres sont analogues à des modes de vibrations géants. La relation entre ces vecteurs propres et l'équation dépendante du temps de Vlasov est explorée.

Acknowledgements

I wish to thank my thesis advisor Professor S. Das Gupta for having guided me to the completion of this thesis. In the course of this study, I enjoyed moments of excitement and even laughter in the search for the clues to answers in the field of heavy-ion reactions. This study would not have been possible without his financial assistance, and I gratefully acknowledge his generosity.

I owe an especial debt of gratitude to Dr. S J. Lee and Dr. E.D. Cooper who have assisted me in appreciating nuclear physics and for their generous efforts in instructing me in computational physics. It is a pleasure to thank Professor J. Barrette for bringing to my attention the data from GANIL, cited in Chapter 6, prior to its publication, and to Mr. J.F. Malouin for rendering the abstract in French.

The support and encouragement I received from Rana in the course of writing this thesis will be cherished and remembered.

Table of Contents

Chapter 1: General Introduction

1.1 The physics of heavy-ion collisions

The study of heavy-ion collisions as a branch of nuclear physics concerns the properties of nuclear matter subject to variation of density, pressure and excitation energy. These diverse physical conditions can be realized in the laboratory by accelerating nuclei against each other. Contemporary heavy-ion accelerator facilities encompass a broad bombarding energy range. Nuclear matter is currently probed at bombarding energy from 10 MeV/A to as high as 200 GeV/A. By subjecting nuclei to conditions far from their normal state new manifestations of nuclear matter, it is hoped, will be revealed.This optimism stems from theoretical arguments predicting the possible phases of nuclear matter according to its temperature and pressure [Mig 78, Lee 76]. Related to this search for novel phenomena is the effort to extract the nuclear equation of state describing the response of nuclear matter to variation of density. This piece of information is of vital importance to the accurate determination of the properties of neutron stars and the character of supernovae explosions [BCK 85]. To ensure the general applicability of this equation of state its validity over a large density domain ought to be mapped out. Considerable effort was exerted in the last few years in this pursuit [Sto 86, BDa 88], and the issue remains one of the principal interests in heavy-ion research.

A topic of current interest is the search for the signatures of nuclear liquid-gas phase transition. Guidance from theoretical analysis instructs us that this is a necessary property of nuclear matter by virtue of the nature of nuclear interaction as

expressed in its equation of state [GKM 84]. The expected phase change should occur at temperature around 20 MeV, which can be reached at intermediate bombarding energies ($E_{lab}/A \sim 100MeV$). This expectation represents a reasonable goal of the current heavy-ion research programme.

The preceeding enumeration of the physical phenomena that come under the purview of heavy-ion research features some of the most pertinent issues to both theoreticians and experimentalists alike. Heavy-ion physics has, in this view, extended the scope of the traditional patterns of investigation in nuclear physics. Apart from these aspirations, the elucidation of the phenomenology of heavy-ion reactions has brought together concepts from disciplines as diverse as statistical physics, thermodynamics, fluid dynamics and, of course, nuclear physics.

The study of heavy-ion reactions can be broadly classified into three distinct energy regimes made possible by the identification of the reaction mechanisms and products. Reactions at low energies ($E_{lab}/A \leq 20MeV$) are predominantly governed by the (single-particle) mean field potential. The reaction products decay according to a few well known modes such as fusion, fission, deep-inelastic scattering and evaporation [Sco 80]. Since the relevant degree of freedom is the mean field the time-dependent Hartree-Fock (TDHF) theory provides an excellent framework to account for fusion, fission and deep-inelastic scattering [Dav 85]. This is supplemented by the statistical evaporation method [FL 83] to explain the evaporative channel. The typical time scale of the reaction is about $10 - 10^6 \times 10^{-22}$ sec, which is very long on the scale of strong interactions.

At relativistic energies ($E_{lab}/A \geq 400MeV$), the mean field losses its domi-

nance over to the nucleonic and mesonic degrees of freedom. Collisions between nuclei may, in this regime, be viewed as two-body correlations between nucleons. The resulting systems attain near statistical equilibrium [CMV 81] making them a fertile ground for the employment of equilibrium concepts [DM 81]. When the systems finally disintegrate the observed products consist of light particles such as $n, p, d,^3 He, \alpha, \pi$ and K. Recent analysis of events in this energy regime using more exclusive measuring devises [Gus 84, DO 85] demonstrates that nuclei can exhibit flow behaviour characteristic of a fluid. Dynamical model as embodied in the Boltzmann-Uehling- Uhlenbeck (BUU) equation was constructed to test the sensitivity of this effect on the nuclear matter equation of state [BDa 88]. After a few years of vigorous activity, the consensus at this point in writing is that the nuclear compressibility (K) of this equation is approximately 200 MeV [Gal 87, GDa 88]. This result is compatible with calculations based on more elaborate many-body techniques [FP 81] and the extracted experimental value from monopole vibrations [Bla 80]. The search for more sensitive observables continued unabated however [BDa 88]. Collisions at ultra-relativistic energies ($E_{lab}/A \geq 10GeV$) have also made a mark in the development of heavy-ion science. Investigators in this field are principally interested in identifying the possible signatures of the transition from the nucleonic to quark and gluon degrees of freedom. This aspect of heavy-ion reactions lies at the boundary between the particle and nuclear physics.

In the preceeding discussions, each energy regime is associated with a relevant degree of freedom from which a simplifying physical picture or theory is framed. These theories are naturally specialized for a particular energy regime. The trans-

port model of the BUU type is a notable exception in that it embraces both the mean field and nucleonic degrees of freedom [BKD 84]. The older cascade model [CMV 81] lacks the mean field effect, consequently, it must be regarded as valid only in the relativistic domain. Even here, a cautionary remark ought to be added because nuclei persist in their fluid-like behaviour in the compression phase of the reaction [Gus 84, DO 85].

The number of nucleons participating in a typical reaction is usually small (≤ 200). Models based on full dynamics calculations such as the TDHF, hydrodynamics [TW 80], cascade and BUU are more adapted for this purpose because the geometry and finiteness of the interacting systems are naturally taken into account. In parallel with these developments, the beginnings of the relativistic extension of the BUU model have been witnessed [Blä 88, KLW 87]. This formalism utilizes the meson exchange models [SW 86] to substitute for more widely used Skyrme-type interaction. The trend in the theoretical development as we conclude the survey in the high and low energy regimes is clearly in favour of the dynamical approach even though it is computationally intensive.

Heavy-ion reactions in the intermediate energy regime ($20MeV \leq E_{lab}/A \leq 200MeV$) are characterized neither purely by the mean field nor nucleon-nucleon collisions. Rather, these degrees of freedom are simultaneously present, producing complex physical conditions that are not amenable to analysis by theories described previously. Elementary nucleon-nucleon collisons are frequently Pauli blocked thus failing to drive the colliding systems to an equilibrium state. However, sufficient excitation energy is imparted to the interacting system to enable it to disintegrate

into large fragments. Experiments performed at the Lawrence Berkeley Laboratory (LBL) [Jac 87] show that typical mass spectra in this energy regime span over a broad mass range. This feature distinguishes this energy regime from the relativistic (nucleus-nucleus) collisions where final states are predominantly light particles. It is often referred to as multi-fragmentation phenomenon. Alternatively, the phenomenon may be viewed as a development of dynamical instability leading to a sudden disintegration into sizable fragments. The conditions under which such a scenario can prevail for an infinite system have been analysed by authors in refs. [BS 83, PR 87]. There are further dynamical studies aimed at tracing the trajectory of the interacting zone on the phase diagram [GB 88]. These lines of thinking serve to isolate the underlying mechanisms responsible for multi-fragmentation.

Based on the general conditions presented above that are thought to prevail in the intermediate energy regime a considerable number of models have been constructed to predict specific observables. These models fall into two categories: statistical and dynamical approaches. Within the statistical approach they are several variants; some are based on phase-space simulations [Gro 84, Koo 86] and others on the idea of percolation [Bau 86]. These models are quite successful in reproducing the mass distribution [Jac 87]. They possess in common the view that the interacting systems enter a chaotic or complex state due to the intricate interplay between the mean field and collisions. The resultant system is thus dominated by statistical effects.

A chaotic state is achieved when the dynamics of the system possesses fluctuations that grow as the system evolves. This basic idea is embodied in dynamical

models of varying degrees of sophistication. In one study where quantum dynamics is solved [KS 84, KW 88] fluctuations are built into the initial system without asking how they are generated. This preliminary study shows the system is capable of disintegrating into large fragments. Provided the beam energy is sufficiently high ($E_{lab}/A \geq 50MeV$) quantum effects are rendered ineffective in the process of violent collisions. In this limit, semi-classical approaches to nuclear dynamics are considered to be adequate. This class of dynamical models has the natural advantage of being simpler computationally. Moreover, they have the attractive feature of handling the collision process, consequently, the entire reaction is completely determined by the dynamics.

The transport model referred to earlier as the BUU equation is a semi-classical reduction of quantum dynamics [KB 62]. In recent years, it has emerged as one of the standard theoretical tools for the analysis of experimental data in the intermediate energy regime. The outstanding successes of the model include the prediction of the nuclear flow effect, transverse momentum analysis and pion production [BDa 88]. To a lesser extent, it explains the basic features of proton spectra [AB 85] and photon production [Bau 86]. Numerical investigations in this approach are extensive thus existing reviews [BDa 88, GB 87, Ber 85] must be consulted for full treatment of the subject.

The BUU model as it stands is not suited for fragmentation studies because nucleon-nucleon collision effects are averaged over an ensemble of colliding systems [BKD 84]. The resultant system does not develop structural instability. In a recent re-examination of this model [BBD 87], a modified collision mechanism is proposed

to allow for the appearance of fluctuations. Substantial fragmentation is seen with this modification. The physics of incorporating the collisions self-consistently in semi-classical approaches is a non-trivial undertaking. This subject is still in its developing stage [TS 86, AG 88].

Other attemps to understand fragmentation phenomena have been made using models which are less firmly rooted in quantum many-body theories. It has been shown that certain features of the mass distribution can be analysed and reproduced by the molecular dynamics [Aic 88] and hybrid [GD 85] models. Even classical dynamics approaches [LP 86, VJP 85, SP 87] have been employed in recent studies.

This survey portrays the complexity of intermediate energy collisions and the lack of a unified approach to the subject. In the author's view, the search for an adequate theory of fragmentation needs to go beyond the reproduction of mass distributions. It is desirable at this juncture to extract more detailed information about fragmentation from the experiment to enable a more realistic evaluation of existing models' validity.

1.2 Present work

The content of this thesis is based on the semi-classical approach to nuclear dynamics. We derive, in chapter 2, the basic formulae of this approach from the many-body quantum kinetic equation upon which developments in the subsequent chapters depend. The resulting (single-particle) transport equation we propose for nuclear dynamics at intermediate energies is the BUU equation which has been extended to include single-particle fluctuations [BBD 87]. Within the context of this

model, contributions made to original knowledge in this thesis are two fold. First, we performed explicit calculations (chapters 3 and 6) using the model to confront a selected number of pertinent experimental observables over a considerable energy range. In doing so, the strengths and weaknesses of the model are evaluated. The second aspect of the thesis's contribution is on the formal development of the semi-classical description of the nuclear ground state and small amplitude vibrations. We extended the work of Madisson and Brink [MB 82] in generating self-consistent nuclear density. We took a step further by examining the stability condition of the (self-consistent) solution. The stability condition is shown to be an eigenvalue problem whose solutions are a good approximation of giant vibration modes. This led us to explore the relationship between the stability condition and nuclear vibration modes.

The BUU equation is separable into terms describing the mean field and the collision dynamics. The mean field term is shown to be derivable from the many-body Schrödinger equation in chapter 2. This derivation is made possible through the standard mean field approximation and semi-classical reduction ($\hbar \rightarrow 0$). We then derive the Uehling-Uhlenbeck collision term using physical arguments similar to those presented to derive the collision term in the Boltzmann equation [LP 81]. Numerical procedures required to solve the BUU equation are summarized in sect. 2.4. As a necessary part of numerical computation, we test the reliability of our numerical parameters in maintaining the nuclear ground state properties. Limitations and applicability of the technique are discussed in sect. 2.6. The plan of the thesis is such that specific aspects of our numerical solution that are thought

to be sensitive to the data we wish to compare with are tested in the appropriate chapters.

In chapter 3, preliminary results on spectator fragmentation are presented. We first outline the Goldhaber model of spectator fragmentation. Several improvements (sect. 3.2) to this model are also made and these results are original as well. The results from the BUU calculations are parametrized according to this model and compared to available data. We proceed to perform more central collisions at 72 and 92 MeV/A to compare with the mass distributions obtained from the Lawrence Berkeley Laboratory (LBL) [Jac 87].

We seek to refine the model used in chapter 3 in one essential way. Since previous calculations are based on the local Skyrme-type interaction the self-consistent ground state density does not possess a diffuse surface. This is certainly not satisfactory for peripheral heavy ion collisions. A finite range interaction of the BKN-type [BKN 76] is introduced. This form of interaction implies a non-trivial ground state self-consistent density. We thus embark on solving for the self-consistent solutions of nuclear ground state densities in chapter 4. This is performed thoroughly for different parameter sets and nuclear systems. A sample time propagation of the newly found ground state density is done using the collisionless BUU (or Vlasov) equation.

We cast the statement ensuring the stability of the self-consistent density into an eigenvalue problem. We call the matrix to be diagonalized the stability matrix. The eigenfunctions of this matrix are shown to correspond to giant vibration modes numerically. A formal approach is then taken to relate these eigenfunctions to the

solutions of the time-dependent Vlasov equation.

Chapter 6 is the culmination of the results established in chapters 2 and 4. The final model of nuclear dynamics with finite range interaction and diffuse surfaces for nuclei are tested. The BUU calculation is done for peripheral interaction of ^{40}Ar on ^{27}Al at 44 MeV/A. Inclusive and exclusive spectator observables are analysed in detail. The meaning of these results are interpreted and the validity and limitations of the BUU model are assessed.

Chapter 2: The model of nuclear dynamics

2.1 Introduction

This chapter delineates the content of the model of nuclear dynamics we propose for colliding nuclear systems. The concepts and formalisms introduced here form the basis for the interpretation of results in the subsequent chapters and for the extension of the model itself.

We first introduce the derivation of the BUU kinetic equation. This derivation consists of two parts. In the first part, we consider nucleons moving in the self-consistent field. The appropriate dynamical equation is the TDHF equation. Next, we define the Wigner transform of the density matrices and then cast the TDHF equation in terms of the Wigner function. When the semi-classical limit is approached, the TDHF equation reduces to the so-called Vlasov equation. In addition, we summarize the identities satisfied by the Wigner function before and after the semi-classical limit is approached.

In the second part, a source term is introduced into the Vlasov equation which represents residual interactions between nucleons. The source term is more commonly known as the Uehling-Uhlenbeck collision integral. As a way of gaining a physical understanding of the collision integral, where rigorous proof is rather involved, we show how using physical arguments alone the essentials of this term can obtained and interpreted.

The results in the preceeding discussions are standard materials in the nuclear physics literature. The numerical method used to solve the BUU equation , to be

introduced in section 2.4, is however a recent innovation. The details of the method are documented in many places [Won 82, BKD 84, BDa 88], it is thus considered sufficient to summarize its essentials in this thesis.

The model of nuclear dynamics presented in sections 2.2, 2.3, and 2.4 constitutes the BUU theory as practiced in heavy-ion physics. This thesis takes a step beyond this theory by introducing a new collision mechanism as a means to remedy where the BUU theory has failed. The content of this concept and its superiority over the BUU theory are discussed in section 2.5. For completeness, the resulting model is tested for its numerical accuracy in section 2.6. In particular, we examine the stability of a model nuclear ground state.

2.2 The Vlasov formalism

The starting point in the derivation of the kinetic equation is the many-body dynamics equation. For nuclear systems the dynamics is governed by the many-body Schrödinger equation

$$i\hbar\frac{\partial\Psi}{\partial t} = H\Psi \tag{2.2.1}$$

In the nucleus of N nucleons, the general wavefunction is

$$\Psi = \Psi(\vec{r}_1, \vec{r}_2, \vec{r}_3, ..., \vec{r}_N)$$

and the Hamiltonian, assuming only a two-body potential between nucleons, is

$$H = \sum_{i=1}^{N}\frac{p_i^2}{2m} + \frac{1}{2}\sum_{i,j=1}^{N} V(\mid \vec{r}_i - \vec{r}_j \mid) \tag{2.2.2}$$

Equivalently, eqn. (2.2.1) may also be written in terms of the density matrix. We define the single particle density matrix in the quantized notation to be

$$\rho_{ji} = \langle\Psi \mid a_i^\dagger a_j \mid \Psi\rangle \tag{2.2.3}$$

where $|\Psi)$ is the N-body state vector. The indices of the creation ($a_i^\dagger$) and annihilation (a_i) operators refer to a complete set of single-particle basis states describing the spatial (or momentum), spin and isospin nucleon coordinates. These operators are required to satisfy the usual anti-commutation relations

$$\begin{aligned} \{a_\alpha, a_\beta^\dagger\} &= \delta_{\alpha\beta}, \\ \{a_\alpha, a_\beta\} &= \{a_\alpha^\dagger, a_\beta^\dagger\} = 0 \end{aligned} \tag{2.2.4}$$

To proceed further, we introduce the following second quantized field operators [FW 71]

$$\begin{aligned} \hat{\psi}(\vec{r}) &= \sum_\alpha \psi_\alpha(\vec{r}) a_\alpha \\ \hat{\psi}^\dagger(\vec{r}) &= \sum_\alpha \psi_\alpha^*(\vec{r}) a_\alpha^\dagger \end{aligned} \tag{2.2.5}$$

where ψ_α are the single-particle wavefunctions. These field operators satisfy the same anti-commutation relations as the a-operators (suppressing the spin indices)

$$\begin{aligned} \left\{\hat{\psi}(\vec{r}), \hat{\psi}^\dagger(\vec{r'})\right\} &= \delta(\vec{r} - \vec{r'}) \\ \left\{\hat{\psi}(\vec{r}), \hat{\psi}(\vec{r'})\right\} &= \left\{\hat{\psi}^\dagger(\vec{r}), \hat{\psi}^\dagger(\vec{r'})\right\} = 0 \end{aligned} \tag{2.2.6}$$

In this notation, the Hamiltonian operator becomes

$$\hat{H} = \sum_{\alpha\beta} t_{\alpha\beta} a_\alpha^\dagger a_\beta + \frac{1}{2} \sum_{\alpha\beta\gamma\delta} V_{\alpha\beta\gamma\delta} a_\alpha^\dagger a_\beta^\dagger a_\delta a_\gamma \tag{2.2.7}$$

where the matrix elements of the kinetic energy are

$$t_{\alpha\beta} = \int d^3r \psi_\alpha^*(\vec{r}) T(\vec{r}) \psi_\beta(\vec{r}) \quad ; T(\vec{r}) = \frac{-\hbar^2}{2m} \nabla^2, \tag{2.2.8}$$

and the two-body potential

$$V_{\alpha\beta\gamma\delta} = \int d^3r d^3r' \psi_\alpha^*(\vec{r}) \psi_\beta^*(\vec{r'}) V(|\vec{r} - \vec{r'}|) \psi_\gamma(\vec{r}) \psi_\delta(\vec{r'}) \tag{2.2.9}$$

The matrix elements of the single-particle kinetic energy and the two-particle potential energy are hermitian:

$$t_{\alpha\beta} = \langle \alpha \mid T \mid \beta \rangle = t^*_{\beta\alpha} \tag{2.2.10}$$

$$V_{\alpha\beta\gamma\delta} = \langle \alpha\beta \mid V \mid \gamma\delta \rangle = V^*_{\gamma\delta\alpha\beta} \tag{2.2.11}$$

These relations imply that the Hamiltonian operator is also hermitian.

Upon using the hermicity of $\hat{H}$, we readily derive the time-dependent equation for the density matrix

$$\begin{aligned} i\hbar \frac{\partial \rho_{ji}}{\partial t} &= \langle \Psi \mid [a_i^\dagger a_j, \hat{H}] \mid \Psi \rangle \\ &= \langle \Psi \mid a_i^\dagger, [a_j, \hat{H}] + [a_i^\dagger, \hat{H}] a_j \mid \Psi \rangle. \end{aligned} \tag{2.2.12}$$

And with the help of the commutation relations (2.2.4) we obtain

$$i\hbar \frac{\partial \rho_{ji}}{\partial t} = \sum_\alpha (t_{j\alpha}\rho_{\alpha i} - \rho_{j\alpha}t_{\alpha i}) + \frac{1}{2}\sum_{\alpha\beta\gamma} (\tilde{V}_{j\alpha\beta\gamma}\rho^{(2)}_{\gamma\beta i\alpha} + \rho^{(2)}_{\gamma j\alpha\beta}\tilde{V}_{\alpha\beta\gamma i}) \tag{2.2.13}$$

after some algebraic manipulations. We have defined the anti-symmetric matrix elements of the potential energy to be

$$\tilde{V}_{j\alpha\beta\gamma} = V_{j\alpha\beta\gamma} - V_{j\alpha\gamma\beta} = -\tilde{V}_{j\alpha\gamma\beta} \tag{2.2.14}$$

and the two-particle density matrix

$$\rho^{(2)}_{\gamma\beta i\alpha} = \langle \Psi \mid a_i^\dagger a_\alpha^\dagger a_\gamma a_\beta \mid \Psi \rangle \tag{2.2.15}$$

Equation (2.2.13) expresses the time evolution of the single-particle matrix ρ_{ji} in terms of the single- and two-particle matrix elements, $\rho^{(2)}$. In a similar manner, one can also derive the time evolution of the two-particle density matrix which

will in turn depend on the next order matrix elements, $\rho^{(3)}$. This procedure can be continued until $\rho^{(N)}$. The result is a set of N coupled differential equations to be regarded as completely equivalent to the N-body Schrödinger equation (2.2.1) when they are solved simultaneously. To arrive at a tractable theory of quantum dynamics, this set of equations is usually truncated at the single- or two-particle density matrix equation. The well-known TDHF equation, proposed by Dirac, truncates this series at the single-particle level. The fundamental approximation of the TDHF equation says that it is possible to write

$$\begin{aligned} \rho^{(2)}_{\alpha\beta\gamma\delta} &= \langle \Psi \mid a^\dagger_\gamma a^\dagger_\delta a_\alpha a_\beta \mid \Psi \rangle \\ &= -\rho_{\alpha\beta\delta\gamma} = -\rho_{\beta\alpha\gamma\delta} \\ &\simeq \rho_{\alpha\delta}\rho_{\beta\gamma} - \rho_{\beta\delta}\rho_{\alpha\gamma} \end{aligned} \tag{2.2.16}$$

This is essentially the mean field approximation apart from the anti-symmetric property of the matrix that retains the two-particle correlation as required by the Pauli principle.

An important mathematical property of the matrix ρ follows from the approximation of eqn. (2.2.16) when we set index $\alpha = \delta$. We read from eqn. (2.2.16) that

$$\sum_\alpha \rho_{\beta\alpha}\rho_{\alpha\gamma} = \rho_{\beta\gamma} \tag{2.2.17}$$

where we have used $\sum_\alpha \rho_{\alpha\alpha} = N$ to arrive at this equation. More conventionally, the above statement is written in the operator form

$$\rho^2 = \rho \tag{2.2.18}$$

which evidently implies that ρ admits only eigenvalues 0 and 1. Furthermore, from the definition of the density matrix (eqn. (2.2.3)) and the anti-commutation

property of the operators $a^\dagger_\alpha$ and a_α, we conclude that statement (2.2.18) constrains the general wavefunction to be a Slater determinant

$$\mid \Psi\rangle = a^\dagger_1 a^\dagger_2 \ldots a^\dagger_N \mid 0\rangle \tag{2.2.19}$$

which is spanned by a (complete) set of single-particle basis states.

The next important quantity we would like to define is the Hartree-Fock mean field potential

$$\langle j \mid U \mid \gamma\rangle = \sum_{\alpha\delta} \tilde{V}_{j\alpha\gamma\delta}\rho_{\delta\alpha} \tag{2.2.20}$$

With the above definition the potential energy part of the equation of motion (eqn.(2.2.13)) may be written, after using the fundamental approximation, as

$$\begin{aligned} i\hbar\frac{\partial \rho_{ji}}{\partial t}\mid_{pot} &= \sum_\gamma \Big(\langle j \mid U \mid \gamma\rangle\rho_{\gamma i} - \rho_{j\gamma}\langle\gamma \mid U \mid i\rangle\Big) \\ &= \sum_\gamma \Big(\langle j \mid U \mid \gamma\rangle\langle\gamma \mid \rho \mid i\rangle - \langle j \mid \rho \mid \gamma\rangle\langle\gamma \mid U \mid i\rangle\Big) \\ &= \langle j \mid U\rho - \rho U \mid i\rangle = \langle j \mid [U,\rho] \mid i\rangle \end{aligned} \tag{2.2.21}$$

The equation of motion of ρ_{ji} can now be identified as the Heisenberg equation in the density matrix formalism

$$i\hbar\frac{\partial \rho_{ji}}{\partial t} = \langle j \mid [H_{MF},\rho] \mid i\rangle \tag{2.2.22}$$

where the mean field Hamiltonian

$$H_{MF} = T + U \tag{2.2.23}$$

We call the derived expression the TDHF equation to be consistent with literature. It is a non-linear equation in ρ due the appearance of ρ in H_{MF}. This is a general feature of the truncated many-body dynamics equation.

In the application of TDHF to heavy-ion reactions, the equations to be solved are usually not in the form written in eqn.(2.2.22) . Rather, it is most often formulated in the conventional wavefunction language. We insisted on deriving the TDHF equation in the density matrix formalism so as to permit an apparent transition to the Vlasov equation later. The success of the TDHF equation as a basis of small amplitude vibration is well documented [SF 75, GS 81]. In the last few years, extensive calculations in the low energy heavy ion reactions have further demonstrated the validity of the TDHF equation as a suitable dynamical theory for nuclear phenomena. Of specific interest to our consideration here is its success in describing low energy reactions ($\leq$ 10 MeV/A), ranging from fusion to deep-inelastic scattering phenomena [Dav 85, BKN 76].

TDHF calculations are numerically intensive, consequently, many calculations have been performed with reduced dimensionality of the problem. This is a difficulty that has hampered a systematic comparison with experiment. As an alternative to the TDHF equation, we present in the next few pages, a derivation of its semi-classical reduction with the desire to achieve a more manageable equation.

The Vlasov equation is a semi-classical reduction of the quantum mechanical TDHF (eqn.(2.2.22)). To perform this reduction the TDHF equation may be transformed into an equation describing time evolution of the Wigner function. The Wigner function is defined as

$$f(\vec{r},\vec{p},t) = \frac{\gamma}{(2\pi\hbar)^3}\int d^3s\ \exp(-i\frac{\vec{p}}{\hbar}\cdot\vec{s})\rho(\vec{r}+\vec{s}/2,\vec{r}-\vec{s}/2,t) \qquad (2.2.24)$$

where γ is spin-isospin degeneracy factor. The Wigner function is simply the Fourier transform of the relative coordinate of the off-diagonal density matrix. The Wigner

function is real but not positive definite; therefore, it is not always permissible to interpret it as the phase space density. However, it may be regarded as the quantum counterpart of the classical phase space density in the Liouville equation [Rei 84]. In addition, it is possible to define more general Wigner functions with two, three or more particle phase space variables. Since the TDHF is a single-particle dynamical equation, it suffices to consider the single-particle Wigner function (eqn. (2.2.24)) here.

From $f(\vec{r},\vec{p},t)$, single-particle physical quantities such as density, current and kinetic energy density attain their classical forms:

$$\begin{Bmatrix} \rho(\vec{r},t) \\ \vec{J}(\vec{r},t) \\ \tau(\vec{r},t) \end{Bmatrix} = \int d^3p \begin{Bmatrix} 1 \\ \frac{\vec{p}}{m} \\ \frac{p^2}{2m} \end{Bmatrix} f(\vec{r},\vec{p},t) \tag{2.2.25}$$

Similarly, a momentum space density may also be defined

$$g(\vec{p},t) = \int d^3r f(\vec{r},\vec{p},t); \tag{2.2.26)}$$

and the particle number of the system

$$\begin{aligned} N &= \int d^3p g(\vec{p},t) = \int d^3r \rho(\vec{r},t) \\ &= \int d^3r d^3p f(\vec{r},\vec{p},t). \end{aligned} \tag{2.2.27}$$

If we now take the Fourier transform of the TDHF equation, it is then expressible in terms of the Wigner function [RS 80]

$$\frac{\partial f(\vec{r},\vec{p},t)}{\partial t} + \frac{2}{\hbar} f(\vec{r},\vec{p},t) \sin(\frac{\hbar}{2}\overleftrightarrow{\Lambda}) H(\vec{r},\vec{p},t) = 0 \tag{2.2.28}$$

where the classical Liouville operator

$$\overleftrightarrow{\Lambda} = (\overleftarrow{\nabla}_r \cdot \overrightarrow{\nabla}_p - \overleftarrow{\nabla}_p \cdot \overrightarrow{\nabla}_r) \tag{2.2.29}$$

The single-particle Hamiltonian in the TDHF equation is written as

$$\begin{aligned} H(\vec{r},\vec{p},t) &= \int d^3s \, \exp(-i\frac{\vec{p}}{\hbar}\cdot\vec{s})\langle \vec{r}+\vec{s}/2,t \mid H_{MF} \mid \vec{r}-\vec{s}/2,t\rangle \\ &= \frac{p^2}{2m} + U(\vec{r},\vec{p},t) \end{aligned} \tag{2.2.30}$$

Notice that the mean field could in general be momentum dependent. When eqn. (2.2.28) is displayed in expanded form, we obtain

$$\frac{\partial f}{\partial t} + \{f,H\} - (\frac{\hbar}{2})^2 f\frac{(\overleftrightarrow{\Lambda})^3}{3!}H + ... = 0 \tag{2.2.31}$$

where $\{,\}$ is the Poisson bracket. The first and the second term together form the familiar classical Liouville equation, and the higher order terms in $\hbar$ constitute the quantum corrections to classical dynamics. Before proceeding any further, it should be clarified that though the dynamics of these terms being governed by the Liouville operator is classical the intialization of the Wigner function respects the Pauli principle. A systematic analysis of quantum correction order-by-order in $\hbar$ would be desirable to check the extent of the validity of semi-classical dynamics. This effort has largely been rendered difficult by the complexity of the Liouville operator ($\overleftrightarrow{\Lambda}$). Nonetheless, the inclusion of $\hbar^2$ term in the analysis of small amplitude vibrations (giant resonances for example) has been reported by some authors [KSS 86, BDD 86, BDi 88]. They concluded that the gross features of these vibrations are well described by the semi-classical dynamics without $\hbar$ correction. As discussed previously, the application of the TDHF to heavy ion reactions has been known for

some time [BKN 76]. So, instead of introducing a complicated quantum mechanical equation in the form of eqn.(2.2.28) the GANIL research group [Gré 87] has systematically compared their semi-classical calculations with the TDHF results. Quite remarkably. the semi-classical dynamics appears to provide good agreement with its quantum parent for both small and large amplitude motions of nuclei. This gives us added confidence to proceed using the semi-classical dynamics.

Equation (2.2.28) without quantum corrections is commonly known as the Vlasov equation

$$\frac{\partial f(\vec{r},\vec{p},t)}{\partial t} + \Big\{ f(\vec{r},\vec{p},t), H(\vec{r},\vec{p},t) \Big\} = 0 \qquad (2.2.32)$$

This equation preserves the phase space distribution f at all times which is an expression of the incompressibility of $f(\vec{r},\vec{p})$ in the frame of the moving point $(\vec{r},\vec{p})$. Accordingly, once $f(\vec{r},\vec{p},t=0)$ is initialized to respect the Pauli principle ($f \leq \gamma/(2\pi\hbar)^3$), it will be preserved at all subsequent times.

Proceeding further in our examination of the kinetic equations (eqs. (2.2.28) and (2.2.32)), we now look at the properties of the Wigner function according to these equations. When we take the Wigner transform of the product of operators [RS 80], the projector property of ρ (eqn.(2.2.18)), becomes

$$\tilde{f}(\vec{r},\vec{p},t)\cos\Big(\frac{\hbar}{2}\overleftrightarrow{\Lambda}\Big)\tilde{f}(\vec{r},\vec{p},t) = \tilde{f}(\vec{r},\vec{p},t) \qquad (2.2.33)$$

where the normalized f is

$$\tilde{f}(\vec{r},\vec{p},t) = \frac{(2\pi\hbar)^3}{\gamma} f(\vec{r},\vec{p},t) \qquad (2.2.34)$$

To the lowest order in $\hbar$, consistent with the approximation made in deriving the

Vlasov equation (2.1.26), the above condition simplifies to

$$\left(\tilde{f}(\vec{r},\vec{p},t)\right)^2 = \tilde{f}(\vec{r},\vec{p},t) \tag{2.2.35}$$

The Vlasov dynamics thus does not preserve the Slater determinant property of the wavefunctions of TDHF. It does, however, retain the Pauli principle through the condition $\tilde{f}^2 = \tilde{f}$. Equation (2.2.32) together with the above property completes our reduction of the TDHF dynamics to the semi-classical dynamics.

We may also readily prove that the Vlasov equation satisfies the following conservation laws and invariance:

(1) energy-momentum

(2) particle number

(3) Galilean invariance

These are the basic properties that a dynamical theory of heavy ion reactions ought to embody. In addition, they provide a check and constraint on attempted solutions of the Vlasov equation. The simplicity of the Vlasov equation lies in the drastic approximation we made to the many-body Schrödinger equation (2.2.1) . This equation was first reduced to a single-particle equation (2.2.22) and a further approximation was made to reduce the quantum dynamics into a semi-classical one. The non-linearity of the TDHF equation is, however, retained in the Vlasov equation as long as the single-particle potential, $U(\vec{r},\vec{p},t)$, is a self-consistent potential. This potential is often assumed to be functionally density-dependent.

In this section, we shall confine ourselves to a general consideration of the solution of the Vlasov equation in the static limit. In this limit, the Vlasov equation

reduces to a vanishing Poisson bracket:

$$\Big\{ f(\vec{r},\vec{p}), H(\vec{r},\vec{p}) \Big\} = 0 \tag{2.2.36}$$

The general solution of this equation is any functional of the Hamiltonian $f(H^n)$, where n is any positive integer. This is a severe restriction on the functional form of f that we can choose to construct solutions of eqn. (2.2.36) . Nonetheless, the possible solutions allowed by the equation are, in principle, infinite in number. For fermionic systems, we further require the occupation of particles in phase space to respect the Pauli principle

$$f(\vec{r},\vec{p},t) \leq \frac{\gamma}{(2\pi\hbar)^3}. \tag{2.2.37}$$

A possible choice of f describing the ground state nucleus is the Thomas-Fermi approximation [RS 80, BDT 86]

$$f(H) = \frac{\gamma}{(2\pi\hbar)^3}\Theta\Big(g(H)\Big). \tag{2.2.38}$$

where the Θ -function ensures that condition (2.2.37) is maintained. The argument, $g(H)$, is taken to be $(\lambda_F - H)$, where λ_F is the Fermi energy. Since $g(H)$ must be positive, energy levels can only be filled up to λ_F, which is a constant for static systems. An extension to systems with finite temperature, β, is also possible by the following choice of f

$$f(H,\beta) = \frac{\gamma}{(2\pi\hbar)^3}\Big\{1 + e^{\beta(H-\lambda_F)}\Big\}^{-1} \tag{2.2.39}$$

In the standard treatment of the Fermi system in statistical mechanics particles are considered to be non-interacting, i.e. $H = p^2/2m$, in which case eqn. (2.2.39) is

simply a Fermi-Dirac occupation probability. Because nucleons are strongly interacting, even at moderate temperatures (T$\sim$10 MeV), they can not be treated as a free nucleon gas [Lej 86, FL 83]. Of course, this statement is imprecise without specifying the density of the system which determines the average inter-nucleon distance, and therefore, the effective strength of the interaction. The solution of the Vlasov equation in the static limit (eqn. (2.2.38))is completely specified when λ_F and $U(\vec{r},\vec{p},t)$ are known. In the case of finite temperature it has to be supplemented by β. In our reduction of the linear many-body dynamics equation (2.2.1) we introduced a mean field potential that is density dependent, $U = U(\vec{r},\rho,\vec{p},t)$. If this is so eqns. (2.2.38) and (2.2.39) become non-linear integral equations in f. In other words, our choice of f must be consistent with the functional of U. The standard method of solving these non-linear equations is the iterative scheme where a guessed solution is progressively improved with increasing number of iterations. The non-linear nature of the eqns. (2.2.38) and (2.2.39) is a reflection of the retention of interaction between the nucleons, approximated at the level of mean field. From this point of view, the time-dependent Vlasov equation describes self-interacting systems.

The self-consistent solution of the time-independent eqn. (2.2.32) will be developed in chapter 4. The time-dependent solution, unlike the ground state solution, is much more involved. There are no exact solutions but approximate solutions do exist especially for small amplitude motions [BDD 86, BDi 88, KSS 86]. In chapter 6, an attempt is also made to arrive at approximate solutions of small amplitude vibrations.

2.3 The Uehling-Uhlenbeck collision integral

When the beam energy of the projectile is raised the final momenta $(\vec{p}_{1'}, \vec{p}_{2'})$ of colliding nucleons are frequently scattered out of the Fermi sea i.e. $|\vec{p}_{1'}|$ and $|\vec{p}_{2'}| > P_F$. Mean field dynamics will then have to be supplemented by two-body scattering. The effect of collision is to add a source term to the Vlasov equation (assuming a momentum-independent potential)

$$\frac{\partial \tilde{f}_1}{\partial t} + \frac{\vec{p}_1}{m} \cdot \vec{\nabla}_{r_1} \tilde{f}_1 - \vec{\nabla}_{r_1} U \cdot \vec{\nabla}_{p_1} \tilde{f}_1 = I(\vec{r}_1, \vec{p}_1, t) \tag{2.3.1}$$

where the source term [CLG 87, Ber 80, BM 86, GB 87]

$$\begin{aligned} I(\vec{r}_1, \vec{p}_1, t) = -\int \frac{d^3p_2 d^3p_{1'} d^3p_{2'}}{(2\pi\hbar)^9} \omega(\vec{p}_1\vec{p}_2 \rightarrow \vec{p}_{1'}\vec{p}_{2'}) \\ \times \left[\tilde{f}_1\tilde{f}_2(1-\tilde{f}_{1'})(1-\tilde{f}_{2'}) - \tilde{f}_{1'}\tilde{f}_{2'}(1-\tilde{f}_1)(1-\tilde{f}_2)\right] \\ \times \delta^3(\vec{p}_1 + \vec{p}_2 - \vec{p}_{1'} - \vec{p}_{2'})\delta(\epsilon_1 + \epsilon_2 - \epsilon_{1'} - \epsilon_{2'}) \end{aligned} \tag{2.3.2}$$

The $\tilde{f}_i$ is as defined in eqn.(2.2.34) with the index i refering to the momentum coordinate $\vec{p}_i$ and the single particle energies $\epsilon_i = p_i^2/2m + U(\vec{r}_1, t)$. We also denote ω to be the transition rate of the nucleon-nucleon collisions. The collision integral has the effect of widening the phase-space domain occupied by the nucleons. In nuclear fragmentation final state nuclei occupy domains far from each other. The introduction of the collision term is then a step towards a more complete theory of heavy-ion reactions. However, as we shall soon realize, the physics embodied by eqn. (2.3.1) is insufficient to describe fragmentation phenomena with precision.

It is thus necessary to re-examine the basic assumptions in the derivation of this equation (2.3.1) . We present, in the next few paragraphs, a derivation of the Uehling-Uhlenbeck collision integral based on physical arguments. Rigorous

derivations of this term may be consulted in several review articles and papers [KB 62, TS 86, YY 87].

The number of nucleons in the phase space volume $d^3r_1d^3p_1$ is

$$\tilde{f}(\vec{r}_1,\vec{p}_1)\frac{\gamma}{(2\pi\hbar)^3}d^3r_1d^3p_1$$

The collision number per unit volume and unit time between nucleons in $d^3r_1d^3p_1$ and $d^3r_1d^3p_2$ is proportional to

$$-\omega(\vec{p}_1\vec{p}_2\rightarrow\vec{p}_{1'}\vec{p}_{2'})\tilde{f}(\vec{r}_1,\vec{p}_1)\tilde{f}(\vec{r}_1,\vec{p}_2)\frac{d^3p_1d^3p_2}{(2\pi\hbar)^6}\times \delta^3(\vec{p}_1+\vec{p}_2-\vec{p}_{1'}-\vec{p}_{2'})\delta(\epsilon_1+\epsilon_2-\epsilon_{1'}-\epsilon_{2'}) \tag{2.3.3}$$

The negative sign signifies the depletion of nucleons of states $\vec{p}_1$ and $\vec{p}_2$, and ω is the rate of collision; we have also attached momentum and energy conserving delta functions. Implicit in the above expression is the assumption that two-particle correlations can be written as a product of single-particle distribution functions. Physically, this demands that the systems to be treated must be dilute [LP 81].

For many-body nucleon system the final states are Pauli blocked according to the occupation numbers of the final states, namely $\tilde{f}_{1'}$ and $\tilde{f}_{2'}$. The collision number of the forward reaction per unit time is proportional to

$$-\omega(\vec{p}_1\vec{p}_2\rightarrow\vec{p}_{1'}\vec{p}_{2'})\tilde{f}_1\tilde{f}_2(1-\tilde{f}_{1'})(1-\tilde{f}_{2'})\delta^3(\vec{p}_1+\vec{p}_2-\vec{p}_{1'}-\vec{p}_{2'})\times \delta(\epsilon_1+\epsilon_2-\epsilon_{1'}-\epsilon_{2'})\frac{d^3p_1d^3p_2d^3p_{1'}d^3p_{2'}}{(2\pi\hbar)^{12}} \tag{2.3.4}$$

The reverse reaction $\vec{p}_1+\vec{p}_2\rightarrow\vec{p}_{1'}+\vec{p}_{2'}$ may be similarly obtained, and we readily find that it is just eqn. (2.3.4) with the indices 1 and 2 interchanged for $1'$ and $2'$ respectively. We further notice, from the detailed balance, the equality between the forward and reverse transition rates [LP 81].

$$\omega(\vec{p}_1\vec{p}_2\rightarrow\vec{p}_{1'}\vec{p}_{2'})=\omega(\vec{p}_{1'}\vec{p}_{2'}\rightarrow\vec{p}_1\vec{p}_2) \tag{2.3.5}$$

This result enables us to factor ω from the forward and the reverse reaction terms. To find the rate of change of the single-particle distribution, $\tilde{f}(\vec{r}_1, \vec{p}_1, t)$, we integrate over $\vec{p}_2$, $\vec{p}_{1'}$, and $\vec{p}_{2'}$ variables to obtain the final form of the transport equation up to a proportionality constant:

$$\begin{aligned} -\frac{d^3p_1}{(2\pi\hbar)^3}\int \frac{d^3p_2 d^3p_{1'} d^3p_{2'}}{(2\pi\hbar)^9}\omega(\vec{p}_1\vec{p}_2 \to \vec{p}_{1'}\vec{p}_{2'}) \\ \times \left[\tilde{f}_1\tilde{f}_2(1-\tilde{f}_{1'})(1-\tilde{f}_{2'}) - \tilde{f}_{1'}\tilde{f}_{2'}(1-\tilde{f}_1)(1-\tilde{f}_2)\right] \\ \times \delta^3(\vec{p}_1+\vec{p}_2-\vec{p}_{1'}-\vec{p}_{2'})\delta(\epsilon_1+\epsilon_2-\epsilon_{1'}-\epsilon_{2'}) \\ \propto \frac{d^3p_1}{(2\pi\hbar)^3}\frac{d\tilde{f}_1}{dt} \end{aligned} \tag{2.3.6}$$

The transition rate is related to the cross-section whose relation in the center of mass of the colliding pair is

$$\omega(\vec{p}_i \to \vec{p}_f) \sim v_{rel}\sigma(\vec{p}_i, \vec{p}_f) \tag{2.3.7}$$

where $\vec{p}_i$ and $\vec{p}_f$ are the initial and final momenta in this frame. This transport equation has been extensively used to analyse various features of heavy-ion reactions [BKD 84, Sto 86, GBD 87, BDa 88, Dan 88]. We call it the Boltzmann-Uehling-Uhlenbeck (BUU) but it has also been known by other names in literature: the Vlasov-Uehling-Uhlenbeck equation [KJS 85], the Boltzmann-Nordheim equation [Nor 28] and the Landau-Vlasov equation [Gré 87].

The collision integral vanishes identically when the system attains statistical equilibrium. The precise statement of the condition is that

$$\left[\tilde{f}_1\tilde{f}_2(1-\tilde{f}_{1'})(1-\tilde{f}_{2'}) - \tilde{f}_{1'}\tilde{f}_{2'}(1-\tilde{f}_1)(1-\tilde{f}_2)\right] = 0 \tag{2.3.8}$$

whose solution is just the Fermi-Dirac occupation factor

$$\tilde{f}_i = \frac{1}{e^{\beta(\epsilon_i-\mu)}+1} \tag{2.3.9}$$

More specifically, the ground state solution of the Thomas-Fermi type can be seen to statisfy the equilibrium condition above.

In the numerical evaluation of the collision integral ω is treated as an input from the experiment through relation (2.3.7) . At relativistic energies, the elastic differential cross-section of the free nucleon-nucleon scattering can be assumed to take the form [Per 74]

$$\frac{d\sigma_{el}}{dt} \sim e^{-b|t|} \tag{2.3.10}$$

where the slope of the exponent is energy dependent

$$b(\sqrt{s}) = \frac{6[3.65(\sqrt{s} - 1.866)]^6}{1 + [3.65(\sqrt{s} - 1.866)]}$$

according to a parametrization [CMV 81, Mas 84, BDa 88] widely used in reaction studies. In these expressions, the s and t are the Mandelstam variables. The scattering angle in this region is highly forward peaked as opposed to a near isotropic angular distribution seen in low energy ($E_{lab}/A \leq 50MeV$) experiments. The inclusion of the inelastic cross-sections is also possible , however, due to their negligible contribution at intermediate energies they will not be discussed in this thesis.

Another question worthy of attention is the medium correction to the cross-section currently used. For a fixed density, the total cross-section approaches the free cross-section, σ^{free} above a certain energy. At high energies, nucleons may be treated as point-like particles whereby the nuclear mean potential has only negligible effect. This problem of treating medium correction has been studied by a few authors [CLG 87, BM 86, KK 68]. They replaced the transition matrix of the free

nucleon-nucleon T-matrix by the Brückner G-matrix:

$$\omega(\vec{p}_1\vec{p}_2 \rightarrow \vec{p}_{1'}\vec{p}_{2'}) = \mid \langle \vec{p}_1\vec{p}_2 \mid G \mid \vec{p}_{1'}\vec{p}_{2'} \rangle \mid^2 \tag{2.3.11}$$

suitable for scattering in the medium. With this correction they found the new cross-section to scale according to [CLG 87]

$$\alpha(p,\rho,T) = 1 + \sum_{nj} a_{nj} \frac{\rho^{j/3}}{(p/p_F)^n} \tag{2.3.12}$$

where T is the temperature and a_{nj} are fixed coefficients.

2.4 Numerical method of solution

The BUU kinetic equation is an integro-differential equation describing the time evolution of f, the distribution in phase-space. The numerical method of solving this equation consists of choosing an appropriate representation of f and then to propagate this f in time. We solve the kinetic equation in two steps. First, f is evolved for a (small) time step Δt according to the Vlasov dynamics then f is instantaneously changed by the collision integral. At all subsequent times these two steps are repeated until the simulation is completed.

Of central importance to our method is the idea of decomposing f into a set of folding functions S to be formally written as

$$f(\vec{r},\vec{p},t) = \frac{1}{\tilde{N}} \sum_{i=1}^{A\tilde{N}} S\Big(\vec{r} - \vec{r}_i(t), \vec{p} - \vec{p}_i(t)\Big) \tag{2.4.1}$$

where $\tilde{N}$ is the number of such functions per nucleon. This technique is prevalent in numerical simulations of heavy-ion reactions. Some authors take S to be a set of coherent states (or moving gaussian bases) [Gré 87, RDH 80] whereas others

assume them to be triangular or gaussian packets [Len 88]. For sufficiently large $\tilde{N}$ the folding procedure is insensitive to the choice of folding functions. In this thesis we work with delta functions or point (test) particles

$$S\Big(\vec{r}-\vec{r}_i(t),\vec{p}-\vec{p}_i(t)\Big)=\delta\Big(\vec{r}-\vec{r}_i(t)\Big)\delta\Big(\vec{p}-\vec{p}_i(t)\Big) \tag{2.4.2}$$

Suppose the configuration space is partitioned into cubic cells then the density in a cell centered at $\vec{r}_\alpha$ is

$$\begin{aligned}\rho(\vec{r}_\alpha)&=\frac{1}{V_\alpha}\int d^3r d^3p f(\vec{r},\vec{p})\\&=\frac{1}{\tilde{N}V_\alpha}\sum_{i\in V_\alpha}^{A\tilde{N}}1\end{aligned} \tag{2.4.3}$$

where V_α is the volume of the cell. Other physical quantities can be similarly evaluated.

Given the representation of f and the choice of folding functions, it can be easily shown that the Vlasov equation is satisfied when the centers of the folding functions follow the classical trajectory

$$\begin{aligned}\frac{\partial\vec{r}_i(t)}{\partial t}&=\frac{\vec{p}_i}{m}\\\frac{\partial\vec{p}_i(t)}{\partial t}&=-\vec{\nabla}_i U(\vec{r}_i).\end{aligned} \tag{2.4.4}$$

In other words, evolving f according to the Vlasov equation is equivalent to evolving a large collection of test particles according to Hamiltonian dynamics.

So far, the mean field function U has not been specified. This function is yet another essential aspect of our model. For the present exploration the simplified version of the Skyrme potential is used. The mean field function has a simple structure

$$U(\vec{r})=-124.0\rho(\vec{r})+70.5\rho^2(\vec{r})\ \ MeV \tag{2.4.5}$$

Because of the rapid rise of the repulsive term with density this U is referred to as the stiff potential. It possesses the usual saturation property with its coefficients chosen so as to minimize at the nuclear matter saturation binding energy of $-16MeV/A$. The corresponding compressibility $K = 378MeV$, which is large compared to more sophisticated nuclear matter theories [FP 81] and extracted experimental value [Bla 80].

We may now proceed to evaluate the force on each test particle. The γ-component of the force on the test particle at $\vec{r}_i$ is

$$F_\gamma(i) = -\Big[U(x_{\gamma,i+1}) - U(x_{\gamma,i-1})\Big]\Big/(x_{\gamma,i+1} - x_{\gamma,i-1}) \tag{2.4.6}$$

where i is the cell label. Having described how the density ρ and the force are determined, the coordinates of the test particles $(\vec{r}_i, \vec{p}_i)$ are propagated (stepwise) in time according to the Hamiltonian dynamics. We do this by using a . second order algorithm as follows

$$\begin{aligned} \vec{r}_i(t + \delta t/2) &= \vec{r}_i(t - \delta t/2) + \delta t \frac{\vec{p}_i(t)}{m}, \\ \vec{p}_i(t + \delta t) &= \vec{p}_i(t) - \delta t \vec{\nabla}_i U(\vec{r}_i, t + \delta t/2). \end{aligned} \tag{2.4.7}$$

Equations (2.4.6) and (2.4.7) constitute the solution to the time-dependent Vlasov equation (2.2.32) in the test particle representation.

The discretization of the configuration space and time unavoidably introduces numerical parameters to the space and time dimensions. We partitioned the configuration space into cubic cells of length $\ell = 1fm$ and discretized the time dimension in steps of $\delta t = 0.3fm/c$ $(1.0 \times 10^{-24}sec)$. Apart from these two numerical parameters there is the freedom to choose the number of test particles per nucleon, $\tilde{N}$.

We fix $\tilde{N}$ at 200 unless otherwise indicated. The statistical fluctuations of density in each cell is about 20% for this $\tilde{N}$. To further reduce the density fluctuations we have also resorted to spreading a test particle density contribution to its adjacent cells. For example, when a test particle is found in the cell at $\vec{r}_a$ we consider its contribution to the density of the cell to be $1/(3\tilde{N}V)$ and $1/(9\tilde{N}V)$ for its adjacent cells. In section 6, the reliability of these parameters will be tested.

We now summarize the test particle implementation of the BUU equation in our numerical method [BDa 88, BKD 84].

The test particles are

1. used to Monte Carlo the phase space density f of a static nucleus; they are then
2. propagated in the mean field for a time step Δt according to the classical trajectory in eqn. (2.4.7) . This is followed by
3. elastic scattering between the test particles. Two test particles are candidates for scattering when they pass the point of closest approach, and

(3a) their distance of closest approach

$$b \leq \sqrt{\sigma_T/\pi}, \tag{2.4.8}$$

where the maximum elastic cross-section σ_T is 55 mb [BDa 88].

(3b) Once they are within this distance they are allowed to scatter with a probability of

$$\sigma(\sqrt{s})/\sigma_T$$

where $\sigma(\sqrt{s})$ is an energy dependent cross-section. To simplify calculation, we chose a constant cross-section of 40 mb. We compared this choice to an energy dependent cross-section [BDa 88] and found the results to be compatible. The scattering angle is then determined by eqn. (2.3.10)

(3c) The final necessary check is to ensure that the test

particles being promoted to new momenta values do not violate the Pauli principle. The probability of blocking is determined by

$$P = 1 - (1 - \tilde{f}_{1'})(1 - \tilde{f}_{2'}) \tag{2.4.9}$$

4. Having concluded that conditions (3a,b and c) are satisfied, we repeat steps 1, 2 and 3 until the entire simulation is completed.

In principle, each test particle should be checked for scattering with all other test particles in the colliding system. If this be so, the number of comparisons at step 1 would be of the order of $\sim (\tilde{N}A)^2$ and accordingly the cross-section (step 3b) is reduced by a factor of $1/\tilde{N}^2$. For $\tilde{N} \sim A \sim 100$, this number is approximately 10^8, which would require enormous computing hours. We are then led to make a suitable approximation [BKD 84]. In this approximation, collisions between test particles are decomposed into $\tilde{N}$ sets of parallel simulations. Each simulation is composed of $\tilde{N}A_P$ test particles from the projectile and $\tilde{N}A_T$ test particles from the target. In the way, collisions are not allowed between test particles of different simulations. Hence, the number of comparisons at step 3 for symmetric colliding systems is reduced to $\tilde{N}A^2$.

2.5 Collisions and fluctuations

The theory of nuclear reaction based on the BUU kinetic theory does not generate sufficient fluctuations to account for fragmentation phenomena [BBD 87]. According to this approach each phase-space volume $d^3r_1 d^3p_1$ is a source of test particle collisions. Moreover, momenta of the scattered particles are *not correlated* i.e. they are not necessarily close in phase-space. As a result, the rate of change of f due to collisions grows in a continuous and gradual fashion without much variation

from one phase-space domain to another. This analysis on the nature of the collision integral demonstrates the weakness of the diluteness assumption mentioned earlier in its derivation. Alternatively, this feature of the BUU theory may be viewed as a superposition of $\tilde{N}$ parallel simulations. In the process of averaging a great number of simulations, the fluctuations contained in each simulation are effectively damped. This is the reason that the BUU theory does not generate sufficient fluctuations to account for the formation of fragments in nucleus-nucleus collisions.

Following Bertsch [BBD 87], we developed a model of nuclear reaction with a modified collision mechanism. The essentials of this model are motivated by physical arguments. We would like to model a collision between two nucleons in a physical way yet retain the test particle method. More precisely, when a collision between two test particles occurs we require $2\tilde{N}$ and not 2 test particles to change their momentum directions. In this manner, the final momenta of the particles are correlated. Proper counting of the collision number implies that the cross-section $\sigma(\sqrt{s})$ of collision must be suppressed by a factor of $1/\tilde{N}$.

Let us formulate the above statements in concrete terms. Suppose two test particles i and j, with isospin indices τ_i and τ_j , have statisfied the conditions for collision (steps 3a, b, c) with the cross-section $\sigma(\sqrt{s})/\tilde{N}$, we associate $(\tilde{N}-1)$ test particles, each possessing isospin τ_i, with the i^{th} particle; and similarly for the j^{th} particle. The criterion for associating the test particles to the i^{th} particle, say, is that only those test particles closest in phase space to it are chosen. This entails a definition of the phase space distance like

$$d_{ik} = (\vec{p}_i - \vec{p}_k)^2 + (p_F/R)^2(\vec{r}_i - \vec{r}_k)^2 \qquad (2.5.1)$$

where k is the index of any test particles to be compared with the i^{th} particle.

At this point, there are two groups of particles, namely the $i-$ and $j-$group. From each group, an average momentum can be defined:

$$\left\langle \vec{P}(i) \right\rangle = \sum_{k=1}^{\tilde{N}} \vec{p}_k(i) \Big/ \tilde{N} \tag{2.5.2}$$

where $\vec{p}_k(i)$'s are the momenta of those test particles that are close in phase-space to the i^{th} test particle, and similarly for the $j-$group. The average momenta of these groups of particles are allowed to scatter elastically without further Pauli blocking. The change in the momenta, $\Delta\vec{p}_i$ and $\Delta\vec{p}_j$ $(-\Delta\vec{p}_i)$, are then attributed to each test particle of the $i-$ and $j-$group respectively. This procedure treats the collision between two groups of test particles, representing two nucleons, thus mimicking a nucleon-nucleon collision. As may be easily shown, it also has the virtue of conserving the overall energy and momentum but not the angular momentum.

2.6 Numerical accuracy of the ground states

Having completed the account of the proposed numerical technique to solve the time dependent Vlasov equation, we proceed to test the reliability of this technique systematically. The solutions of the Vlasov equation known to us are those of the static solutions which correspond to the ground states of nuclei. For local interaction such as the Skyrme force, the ground state has a simple density distribution (eqn.(2.2.38)):

$$\rho(\vec{r}) = \frac{\gamma}{(2\pi\hbar)^3} \frac{4\pi}{3} P_F^3(\vec{r}) \tag{2.6.1}$$

where the Fermi momentum is given by

$$P_F(\vec{r}) = \Big[2m(\lambda_F - U(\rho))\Big]^{1/2}, \qquad r \leq R \tag{2.6.2}$$

which is a constant in the interval $0 \leq r \leq R$, where R is the cut off radius.

A proper description of the ground state in time requires the density to be stable and that the momentum and energy be conserved. For this purpose, we selected three symmetric systems for study: ^4He,^{20}Ne and ^{40}Ca nuclei. These systems were initialized with the model ground state density (2.6.1) and then evolved for a period of 100 fm/c. The density distributions of ^4He,^{20}Ne and ^{40}Ca nuclei are shown in Figs. 2.1, 2.2 and 2.3 respectively. It is quite evident that the nuclei remain bound as a system. However, in all three cases the model density at the surface could not be maintained. Moreover, this behaviour is progressively magnified as the nuclear size decreases. The feature is indicative of the use of finite grid size in configuration space. In Figs. 2.4 and 2.5 the rms radii and momenta are seen to execute oscillatory motions. For ^{40}Ca and ^{20}Ne, the amplitudes of their oscillations are small whereas rather significant oscillation is observed for ^4He nucleus.

After 100 fm/c, the CM momentum acquired a non-zero value of 1.6 to 4.5 MeV/c per nucleon in the order of decreasing mass size. For medium size ^{40}Ca nucleus, the error in the CM motion is small for beam colliding energy per nucleon greater than 50 MeV. For the same beam energy, ^4He nucleus will suffer an error exceeding 20%. The effect of coarsening the configuration space is particularly pronounced in the calculation of the total energy of the system. The rise in total energy can be as much as 20% for ^{40}Ca nucleus and up to 30% for ^4He nucleus. The dominant source of the poor energy conservation comes from the rather primitive way in which the gradient of the potential is evaluated on the grid space. Equivalently, we can express non-conserving energy in terms of the excitation energy. We

obtain excitation energy per nucleon in the range of 2.5 to 5.5 MeV. The excitation energy acquired by the nucleus goes into radial expansion hence the observed oscillatory motion and gradual increase of the rms radii and momenta (Figs. 2.4 and 2.5). Work is now in progress to improve upon the evaluation of this quantity. The conclusion we draw from this discussion is that for small nuclei (A$\leq$ 4) the numerical computation of its dynamical quantities ought to be significantly improved. For medium size nuclei $A \geq 20$, the results are quite satisfactory provided the beam energy of collision exceeds 50 MeV/A.

Chapter 3: Spectator and participant dynamics

3.1 Preliminary discussion

The spectator-participant picture of heavy-ion collisions is an accepted view at high energies. The overlapping zone of the excited nuclear matter is called the participant of the reaction and the remaining cold matter is called the spectator. As the beam energy is lowered ($E_{lab}/A \leq 100MeV$) the clean separation of two distinct regions gradually disappears due to the domination of mean field and the increase of interaction time between the ions. Keeping the limitation of the spectator-participant picture in mind, we will refer to spectators and participants in the subsequent discussions as working terminologies.

In the last few years, much of the effort in the heavy-ion physics at high energy has focused on the participant region of the reaction. This is not surprising in view of the intense interest in understanding the properties of the hadronic matter at high density. Consequently, dynamical calculations done to address the spectator physics are conspicuously scarce. This chapter is on the whole a preliminary attempt to address the relevance of spectator dynamics to the study of nuclear fragmentation.

The fragmentation of the projectile nucleus (or spectator) at high energy [Gre 75] has been successfully explained by the statistical fragmentation model of Goldhaber [Gol 74]. There has been a considerable interest in testing the validity of this model at lower energies [Day 86, Gue 83, Ste 87]. Since the reaction mechanism is expected to change as the beam energy is lowered, Goldhaber's model provides a way of measuring the effect of this change in the observable. This model

is characterized by a size-independent momentum width σ_0 (to be explained in the next section) of the projectile-like fragment. Extensive experimental studies from 20 MeV/A to 100 MeV/A [Gue 83, Gel 77, Ste 87, Kya 86, Rud 86, Biz 86] have shown that σ_0 deviates substantially from its value at high energies. The systematics of the data compiled in ref. [Ste 87] suggest that σ_0 rises rapidly from 30 MeV to 50 MeV and then saturates at higher energies. As yet, no physical interpretation has been given to this data.

Our calculation will aim at obtaining quantities that are characteristic of the Goldhaber model such as the momentum distribution and its width, σ_0. It has been remarked that our calculation is a preliminary one, and this is for a good reason. Spectator dynamics is largely a study of the interaction of nuclear surfaces of interacting ions. So a detailed comparison with experiment can only be made with dynamical models that have correctly treated the nuclear surface. Currently, our simple model of nuclear mean field (eqn.(2.4.5)) gives no diffusiveness of surface whatsoever (eq.(2.6.1)). We ought to go a step further by introducing a finite range potential to generate a self-consistent diffuse surface. This problem is an interesting one, and it requires a reformulation of our basic equations for the self-consistent density. The following chapters will be devoted to generating self-consistent densities and the exposition of its consequences.

Participant dynamics is a result of the complex interplay between the roles of the mean field and two-body collisions. Current dynamical models with varying degrees of sophistication have been devised [KS 84, GD 85, Aic 88] to obtain its mass distribution. The collision mechanism introduced in section 2.4 represents

another attempt in this direction. In section 3.4, we demonstrate in two sample calculations the capability of our approach in reproducing the mass distribution.

3.2 The theoretical model of spectator fragmentation

The Goldhaber model is a statistical , though not a thermodynamic, model of the spectator fragmentation. It was initially developed by Feshbach and Huang [FH 73] who assumed that a highly excited projectile in its rest frame emits particles or fragments randomly. It was further assumed that the nuclear mean field effects are negligible, consequently, the momentum distribution of the emitted fragments reflects the Fermi motion of the nucleons in the projectile.

The momentum distribution of the projectile-like fragment (i.e. fragment travelling close to the beam velocity) of size K observed in high energy collisions can be fitted with a Gaussian

$$g(P_K) \propto \exp\Big\{-\frac{P_K^2}{2\sigma_K^2}\Big\} \tag{3.2.1}$$

where σ_K is the width of the distribution. Feshbach and Huang [FH 73] derived this distribution for the fragmentation of a large nucleus of size A in its rest frame. They considered the fragment of size K to be a random sampling of A nucleons. The drawback of this derivation is the requirement that A be large. We thus regard the Gaussian form of the momentum distribution to be an assumption. The statistical assumptions of Feshbach and Huang were, however, taken over by Goldhaber [Gol 74] who derived a size dependent width σ_K which is in accord with the experiment. The width is directly related to the mean square of the fragment's momentum vector

$$\sigma_K^2 = \frac{1}{3}\langle \vec{p}_K^{\,2} \rangle = \frac{1}{3}\Big\langle \Big(\sum_{i=1}^{K} \vec{p}_i\Big)^2 \Big\rangle \tag{3.2.2}$$

where the average here is taken over all possible sets of K nucleons chosen from A nucleons. In the rest frame of the projectile

$$\sum_{i=1}^{A} \vec{p}_i = 0. \tag{3.2.3}$$

Upon using this constraint on the nucleons' momenta, the width in eqn.(3.2.2) is readily shown to have a parabolic dependence on K:

$$\sigma_K^2 = \frac{K(A-K)}{A-1}\sigma_0^2 \tag{3.2.4}$$

where σ_0 is independent of K and it is directly related to the Fermi momentum of the projectile

$$\sigma_0^2 = \frac{1}{3}\langle p^2 \rangle = \frac{1}{5}P_F^2 \tag{3.2.5}$$

For a typical nucleus, $P_F \approx 250 MeV/c$ which gives $\sigma_0 \approx 112 MeV/c$. A smaller σ_0 is expected when the Pauli exclusion effect is taken into account. Bertsch [Ber 81] showed that this correction narrows the width to about 90 MeV/c for ^{40}Ar projectiles.

After the projectile interacted with the target, the mean field and collision effects would have altered the velocity of the emerging projectile in both the transverse and longitudinal directions. We call $\langle \vec{P}_{ZK} \rangle$ and $\langle \vec{P}_{\perp K} \rangle$ the average shifts of the momentum of projectile-like fragments in the Z- and transverse direction respectively. The rest frame of the fragmenting nucleus will differ from the projectile frame when $\langle \vec{P}_{ZK} \rangle$ and $\langle \vec{P}_{\perp K} \rangle$ are finite. These effects are not considered in the Goldhaber model. With these modifications the differential cross-section in the laboratory frame is then given by

$$\frac{d^3\sigma}{dP_K^3} \propto \exp\left\{-\left(\vec{P}_K - \vec{P}_{0K} - \langle \vec{P}_{\perp K} \rangle - \langle \vec{P}_{ZK} \rangle\right)^2 \Big/ 2\sigma_K^2\right\} \tag{3.2.6}$$

where $\vec{P}_{0K}$ is the beam momentum of K nucleons which we take to be in the Z-direction. The above equation can also be written as follows

$$\begin{aligned}\frac{d^3\sigma}{dP_K^3} \propto & \exp\Big\{-\Big(P_K^2 + P_{0K}^2 - 2(P_{0K} + \langle P_{ZK}\rangle)P_K\cos\theta\Big)\Big/2\sigma_K^2\Big\} \\ & \times \exp\Big\{-\Big(\langle\vec{P}_{ZK}\rangle^2 + \langle\vec{P}_{\perp K}\rangle^2 + 2P_{0K}\langle P_{ZK}\rangle\Big)\Big/2\sigma_K^2\Big\} \\ & \times \exp\Big\{P_K\langle P_{\perp K}\rangle\sin\theta\cos\varphi\Big/\sigma_K^2\Big\}\end{aligned} \tag{3.2.7}$$

where φ is the angle between $\langle\vec{P}_{\perp K}\rangle$ and the component of $\vec{P}_K$ on the $\perp$ plane. In an experiment, the events at different φ's are not discriminated and so data are in fact averaged over events at all φ's. When the φ dependent piece in eqn.(3.2.7) is averaged it becomes a modified Bessel function:

$$\begin{aligned}&\Big\langle\exp\Big\{P_K\langle P_{\perp K}\rangle\sin\theta\cos\varphi\Big/\sigma_K^2\Big\}\Big\rangle \\ &\quad = \frac{1}{2\pi}\int_0^{2\pi} d\varphi\exp\Big\{P_K\langle P_{\perp K}\rangle\sin\theta\cos\varphi\Big/\sigma_K^2\Big\} \\ &\quad = J_0\Big(-iP_K\langle P_{\perp K}\rangle\sin\theta/\sigma_K^2\Big)\end{aligned} \tag{3.2.8}$$

Hence the final form of eqn. (3.2.6) in the laboratory frame has the structure

$$\begin{aligned}\frac{d^2\sigma}{dEd\Omega} \propto & E^{1/2}J_0\Big(-iP_K\langle P_{\perp K}\rangle\sin\theta/\sigma_K^2\Big) \\ & \times \exp\Big\{-\Big(P_K^2 + P_{0K}^2 - 2(P_{0K} + \langle P_{ZK}\rangle)P_K\cos\theta\Big)\Big/2\sigma_K^2\Big\} \\ & \times \exp\Big\{-\Big(\langle\vec{P}_{ZK}\rangle^2 + \langle\vec{P}_{\perp K}\rangle^2 + 2P_{0K}\langle P_{ZK}\rangle\Big)\Big/2\sigma_K^2\Big\}\end{aligned} \tag{3.2.9}$$

where E is the kinetic energy of the fragment K in the laboratory.

The simple model of Goldhaber (eqn.(3.2.1)) has been tested in the energy range $0.40 \leq E_{lab}/A \leq 2$ GeV with targets and projectiles of wide range of sizes [Gre 75]. These experiments confirmed that the Gaussian distribution is independent of target and projectile size. The validity of this model is, however, dependent on

the energy range probed [Day 86, Gue 83]. Firstly, the lower momentum side of the distribution in the longitudinal direction generally departs from the Gaussian distribution, and this is progressively magnified as the beam energy is lowered. Secondly, the compiled experimental width in the beam direction σ_{0Z} [Ste 87] shows a gradual increase within the energy range $20 \leq E_{lab}/A \leq 50$ MeV/A, and levels off to $\sigma_{0Z} \approx 85$ MeV/c thereafter. The calculations in the following section are aimed at testing the Gaussian distribution of the Goldhaber model as modified according to eqn.((3.2.6)) together with its width.

3.3 The BUU calculations

3.3a Initialization of the colliding systems

The nucleus we chose for initial exploration was a symmetric ^{20}Ne nucleus. For simplicity, the collision partner was also chosen to be the same. The colliding systems were then boosted against each other at laboratory projectile energy of 50 MeV/A in one case and 100 MeV/A in the other. At 50 MeV/A, the mean field effects are expected to dominate the dynamics whereas at 100 MeV/A the role of collisions would be significantly enhanced. If we view the interacting Fermi spheres in the CM frame where all calculations in the BUU code are performed, there is a significant overlap at 50 MeV/A and much less so at 100 MeV/A. As a quick measure of the extent of the overlapping spheres, we compare the distance between the centers of the Fermi spheres, d_F. For a small nucleus such as ^{20}Ne, the Fermi momentum can be taken to be $P_F = 230$ MeV/c so the minimum d_F for two non-overlapping spheres is roughly 450 MeV/c. This number is to be compared with d_F

= 306 MeV/c at 50 MeV/A and d_F = 431 MeV/c at 100 MeV/A.

We chose the reaction plane to be the X-Z plane with Z-axis as the beam direction. The final necessary parameter to fix the set up is the impact parameter b. This was chosen in the range $0 \leq b \leq 2R$, where R is again the defining sharp nuclear surface radius. We fixed b at an intermediate impact parameter

$$b = \frac{R}{\sqrt{3}}(1 + \sqrt{2}) = 4.31 \quad fm. \tag{3.3.1}$$

We further required that the nuclei to be mirror images of each other. This means, for a target nucleus in CM having coordinate $(\vec{r}, \vec{p})$ the projectile (also in CM) will be assigned a coordinate $(-\vec{r}, -\vec{p})$. This arrangement is by no means a necessary one.

3.3b Accuracy of the numerical method

The numerical computation of the momentum distribution and its width σ_0 requires an accurate determination of the momenta of the colliding pair. We checked the reliability of our numerical method by traversing the colliding pair in the opposite directions with b large enough so that they do not interact with each other. After a period of 100 fm/c, which is about the length in time that all subsequent calculations will be performed, the transverse momentum per nucleon acquired a non-zero value of ~2 MeV/c. This uncertainty is small (~ 1%) relative to the longitudinal momentum in the CM frame. The change in the longitudinal direction is also about the same.

Next, we tested the spread in momentum due to the mean field alone. The collision cascade was switched off and so the nuclei were allowed to interact through

their mean fields only. After a few runs were taken at $b = 4.31fm$ it was found that the spread per nucleon $\Delta p/A \approx 10$ MeV/c. Since there were no collisions this spread reflects the error in the mean field calculation. As we will see later (Fig. 3.2) this fictitious spread accounts for only 20% of the actual spread.

The spectators or more generally the fragments emerging from the region of violent collisions are in their excited states. These fragments will deexcite by ejecting energetic particles and eventually reach their respective ground states. These features were seen in numerical calculations. More precisely, we extracted the rms radius and momentum of each fragment and traced its time evolution. For example, at $E_{lab}/A = 100$ MeV with $b = 4.31$ fm/c, the collisions are over by 40 fm/c and distinct clusters are formed at time ≥ 50 fm/c. The rms radii and momenta of the fragments from $t = 50$ fm/c onwards continue to change and then saturate at $t_s \sim 80$ fm/c. So what we consider as final states of the fragments are those fragments at t_s. When the impact parameter or the beam energy is changed t_s will correspondingly change but the criteria we used in our calculations to determine t_s were always the same.

3.3c Results and interpretation

The experimental width σ_0 is extracted by fitting a Gaussian (eqn.(3.2.1)) to the observed momentum distribution. This is done for a certain fragment of size K at an angle θ from the beam direction. At a fixed impact parameter b, our model calculations will produce a distributed K values. It is a prohibitive task generate sufficient events for those fragments with a specific K. We circumvent this difficulty

by rewriting eqn. (3.2.4) as follows

$$\sigma_0^2 = \frac{A-1}{K(A-K)}\sigma_K^2 \tag{3.3.1}$$

In this form, all the K dependent factors are on the r.h.s. of the equation. Given a set of events from our simulations, σ_0 is averaged over these events found at all angles. We thus write

$$\sigma_{0_i}^2 = \left\langle \frac{K(A-1)}{A-K}(P_{iK}/K - \langle P_{iK}/K\rangle)^2 \right\rangle \tag{3.3.2}$$

where subscript i refers to the component. The quantity $\langle P_{iK}/K\rangle$ defined in this equation is the average momentum per nucleon of the given set of events in the i direction. In the rest frame of the fragmenting nucleus, the isotropy of the distribution implies σ_{0_i}'s to be the same. It is possible to test this feature of the Goldhaber model from eqn.(3.3.2) .

At impact parameter $b = 4.31$ fm we generated 21 runs which in effect gave us 42 events since the target and projectile are completely symmetrical in the CM. We further so remark that a projectile-like event is an event whereby its longitudinal momentum $P_{ZK} \geq 0.6P_{0Z}$, which is in consistent with the cut used in the experiment [Day 86]. In the laboratory frame this corresponds to 80% of its beam momentum.

The first set of runs we would now like to discuss is at $E_{lab}/A = 100$ MeV. The result in Fig. 3.1 shows a mass distribution which is peaked at mass size K = 15 with a width of less than 4 mass units. We attribute the observed mass dispersion to the collision dynamics since mean field by itself does not produce fluctuations. The momentum distribution in the Z-direction is shown in Fig. 3.2,

it exhibits a clear peak and a Gaussian-like distribution. Evidently more events are needed to establish to the shape unambiguously. Similar Gaussian distributions were also obtained for other components. A more tangible measure of the success of our model are the widths σ_{0i}. The momentum widths without the angular cut are nearly isotropic $\sigma_{0i} \approx 70$ MeV/c for $i = x, y$ and z, as shown in Table 3.1a. This value is estimated to have statistical errors of about 20% given the size of the sample (42 events). However, the systematic errors coming from the inaccuracy of the momentum vectors, whose error was quoted earlier, are small compared to the statistical errors. We compare this value with the experimental width $\sigma_{0Z} \approx 86$ MeV/c [Day 86, Gre 75] which indicates the qualitative nature of the success of our model. A quantitative agreement can not, however, be be forthcoming for other reasons. The poor description of the nuclear surface and the absence of Coulomb interaction, mentioned earlier, have contributed to the discrepancy with experiment. In addition, the calculation was done without averaging over different impact parameters. As similar calculation at $E_{lab}/A = 50$ MeV, gives σ_{0i} to be approximately 15 MeV/c smaller (Table 3.1a). The reduction of the width has been seen in experiments at lower energies ($E_{lab}/A \leq 50$ MeV) [Ste 87, Gel 77, Ege 86].

A further aspect of our results is the average downward shift of the momentum per nucleon $\langle P_{iK}/K \rangle$. The X and Z components of the momentum shift are comparable in magnitude. This observation is true for beam energies at 50 MeV/A and 100 MeV/A (see Table 3.1b). At 50 MeV/A, this value is ≈ -50 MeV/c and -30 MeV/c at 100 MeV/A. An average negative $\langle P_{XK}/K \rangle$ means that the aver-

age scattering angle of the projectile is negative. At lower beam energy, this value naturally increases as the collision dynamics weakens due to the Pauli blocking. In the Y-direction, $\langle P_{YK}/K \rangle \approx 0$ as expected from the symmetry of the initial set up. From this point onwards further discussions on the spectator properties in this section are confined to $E_{lab}/A = 100MeV$.

From the numerical simulations we can extract $\langle P_{iK}/K \rangle$ and σ_{0i}^2 which are then substituted into $d^2\sigma/dEd\Omega$ (eqn.(3.2.9)) to fixed this distribution. The graphical display of the double differential cross-section is shown in Fig. 3.3 as a function of the spectator kinetic energy in the laboratory for $\theta_{lab} = 0°, 3.5°, 7°$ and $15°$. The shapes of these curves remain Gaussian with an approximate constant full width at half-maximum (FWHM) of $\sim$ 140 MeV. This value is again comparable to the experimental value $\sim$ 160 MeV [Gue 83] but measured for $^{12}C + ^{12}C$.

Proceeding further in our test of the Gaussian conjecture, we compare the theoretical angular distribution

$$\frac{d\sigma}{d\Omega} = \int dE \frac{d^2\sigma}{dEd\Omega} \tag{3.3.3}$$

directly with our simulations. Since $\langle P_{iK}/K \rangle$ and σ_{0i}^2 for the systems considered here are not available from the experiment they are again supplied by those obtained from our simulations. The histogram shown on the left of Fig. 3.4 is the angular distribution compiled from the simulations with no Coulomb interaction. Overlapping on this histogram is the smooth curve derived from the Gaussian assumption (eqn.(3.2.6)). The curve fits the histogram rather well. This result peaks at $\theta_{lab} = 4°$ which is somewhat large compared to the existing experimental data. Though there are difficulties in measuring $\theta_{lab} \leq 2°$ in the experiment,

the data clearly indicate a peak somewhere between 0° and 2° [Day 87, Gue 83]. This discrepancy motivated us to perform a similar calculation with the inclusion of Coulomb interaction (see Appendix for details). The result is visibly different; the peak is now shifted from 4° to 2° thus bringing it closer to the experimental results. Coulomb contribution to the spectator angular distribution is thus non-negligible even at 100 MeV/A. The theoretical Gaussian distribution, as can be seen on the right of Fig. 3.4, shows once again excellent agreement with our calculations after the Coulomb correction.

We have learnt from the above evaluation of the results the capability of the BUU approach in reproducing diverse features of the spectator properties. It must be emphasized, however, a direct comparison with the experiment has not been attempted here. This subject will be pursued further in chapter 6 but this time with the object of confronting the experimental data.

3.4 Mass distribution and participant dynamics

The theoretical effort to explain the mass distribution of high energy heavy ion collision is very extensive (see ref [Hüf 85] and references therein). These efforts were spurred by the observed mass distribution [Hir 84] that has a power law character , $d\sigma/dA \sim A^{-\tau}$ where τ is a constant. This form of the mass distribution admits a simple interpretation. When a classical gas undergoes a phase transition, droplets are formed whose mass distribution is precisely described by the power law stated above [Fis 67]. In view of the similarities between the properties of the nuclear equation of state [JMZ 83, GKM 84] and the van der Waals liquid, the power law

was interpreted as evidence of a nuclear liquid-gas transition [GKM 84]. Should this conjecture be true it would have opened up fertile field of research in heavy-ion physics. This interpretation of data was countered by models based on chaotic (cold) fragmentation [CDL 84, AH 84] which are also capable of reproducing the mass distribution. The underlying assumptions about the physical mechanisms responsible for fragmentation in these approaches are irreconcilable. Added to this scene of fragmentation theories are models based on statistical [FR 82,83, Koo 86, Gro 84] arguments. It appears then the mass distribution is insensitive to the underlying physical inputs of these approaches.

In this thesis, we view fragmentation phenomena as complex processes driven by two-body nucleon correlations and mean field. The initial colliding nuclei are confined to a certain region in phase space. Collisions open up the initially unavailable phase space volume occupied by the final states. Meanwhile, the mean field tends to bind the nucleons into pockets we call nuclei. Whether or not the mean field and the two-body correlations can drive the colliding systems to a state where the variety of assumptions about fragmentation become valid is a question we are not about to address here. What we do hope to achieve here is to reproduce certain features of the mass distribution with our dynamical model.

We performed near central collisions of ^{40}Ca on ^{40}Ca at 92 MeV/A and 72 MeV/A where experimental data are available in this energy range [Jac 84]. At each bombarding energy, 30 simulations were taken in the impact parameter range $0 \leq b \leq 4.2fm$. All the calculations here were done without the additional complication of the Coulomb interaction. The precautions exercised in the last section on how

to define a final fragment were similarly taken.

The events obtained from the simulations are shown in fig. 3.5a for beam energy at 92 MeV/A . The mass distribution is characterized by a rapidly decreasing yield from A = 1 to 9 and is relatively flat beyond A≈12. The spectrum then rises to peak at A≈20. This spectrum combines the contributions of the spectator and participant fragments. The experimental data cited in the last paragraph [Jac 87] are however for fragments from the intermediate rapidity region (or the participants). We imposed the momentum cut, as described in section 3.3c, to filter the spectator contribution of the spectrum. Fig. 3.5b shows two very distinct distributions. Participant fragments populate mainly the low mass region and their yield decreases rapidly with fragment size. The spectator fragments are seen to be predominantly large clusters. Apart from its contribution to the large mass region the spectators are also seen to contribute to the very small mass region. The low yield in this region can be explained by a scenario whereby spectator fragments are occasionally destabilized by collisions and subsequently fragments into several small clusters.

More quantitatively, if we constrain ourselves to fit the participant spectrum with the power law then our calculation gives the exponent $\tau \approx 1.5$ whereas the experimental value is almost 3.0. The initial fall-off of the distribution in our model is too slow. Bauer *et al.* [BBD 87] who performed central collisions using the same model for ^{20}Ne on ^{20}Ne at 100 MeV/A found the exponent to be close to our value. This is indicative of the insensitivity of the participant spectrum to the size of the colliding systems.

As the beam energy is reduced to 72 MeV/A, the qualitative character of the

mass distribution changes (Fig. 3.6a). The contribution to the higher mass region is enhanced to compensate for the reduced yield in the intermediate mass region ($A = 6-15$). The strong peak at high mass region occurs at $A \approx 20$. Upon applying the momentum cut, as described before, the spectrum of the participant events are found to retain the character of the unfiltered spectrum (see Fig. 3.6b). Data for $A \geq 14$ are, however, not available to confirm this feature of our results at lower energy. This calculation serves to clarify the effect of lowering the beam energy on the participant observable.

Chapter 4: Nuclei with diffuse surfaces

4.1 The self-consistent density

The theoretical description of nuclear reactions at low energy requires an accurate preparation of the nuclear ground state. Such a consideration is an essential aspect of nuclear fusion studies [Dav 85] where the Hartree-Fock approach provides the basis for the construction of ground states. Realistic ground states can be achieved in this approach [VB 72, BKN 76, Neg 82]. The wavefunctions of the nucleons are determined self-consistently by the Schrödinger equation with an underlying interaction. Since the basis of nuclear dynamics presented in chapter 2 is semi-classical in content it is intrinsically satisfying to stay within the semi-classical approach in the construction of the ground states. The Thomas-Fermi approximation (TFA) as expressed in equation (2.2.38) is a solution to the lowest order truncation in the $\hbar$-expansion of the Hartree-Fock equation. This approximation is capable of generating diffuse nuclear surfaces provided the potential is finite in range. The extension of the TFA [RS 80, Coo 88] which represents a truncation of the next order in the $\hbar$-expansion (eqn. 2.2.31) will improve the nuclear surface. This alternative, however, requires the extension of the Vlasov equation. A method of solving the time propagative solution of the next order in the $\hbar$-expansion is not known, even numerically. Consequently, we will only consider ground states derivable from the TFA.

The approach taken in this chapter to generate the nuclear surface is an extension of Maddison and Brink's work [MB 82]. They considered a simple Skyrme

type interaction with a Yukawa term in one dimension. This form of interaction is precisely the so-called BKN interaction [BKN 76]. We extend this work to three dimensions and consider cases with and without the Coulomb interaction. In fact, their work (MB) came to our attention only after the completion of our calculations.

The conventional form of the mean field potential used in heavy-ion reactions is a zero range potential with three adjustable constants:

$$U_s(\rho) = A\rho(\vec{r}) + B\rho^{\sigma}(\vec{r}), \tag{4.1.1}$$

and it is derivable from the Skyrme forces. Within the TFA (eqn. 2.2.38) the self-consistent equation to be solved is

$$\rho(\vec{r}) = \frac{\gamma}{(2\pi\hbar)^3}\frac{4\pi}{3}\Big[2m(\lambda_F - U(\rho))\Big]^{3/2}\Theta\Big(\lambda_F - U(\rho)\Big) \tag{4.1.2}$$

When $U = U_s$, this equation is an algebraic equation in ρ whose solution for a finite nucleus of radius R is

$$\begin{aligned} \rho(\vec{r}) &= \rho_0 \quad r \leq R \\ &= 0 \quad r > R \end{aligned} \tag{4.1.3}$$

where ρ_0 is a constant. Zero-range potentials in the TFA thus do not generate diffuse surfaces. Let us now consider the BKN potential

$$U(\vec{r},\rho) = A\rho(\vec{r}) + B\rho^{\sigma}(\vec{r}) + \int d^3r' v(\vec{r},\vec{r'})\rho(\vec{r'}) \tag{4.1.4}$$

The finite range interaction, $v(\vec{r},\vec{r'})$, has the familiar Yukawa form

$$\begin{aligned} v(\vec{r},\vec{r'}) &= V_0\frac{e^{|\vec{r}-\vec{r'}|/a}}{|\vec{r}-\vec{r'}|/a} \\ &= 4\pi V_0\sum_{\ell,m} f_\ell(r,r',a)Y_{\ell m}(\theta,\phi)Y^*_{\ell m}(\theta',\phi') \end{aligned} \tag{4.1.5}$$

where a is the range of the force and V_0 determines its strength. The radial function in the above expansion has the structure

$$f_\ell(r, r', a) = i_\ell(r_</a)k_\ell(r_>/a) \tag{4.1.6}$$

where $i_\ell(r_</a)$ and $k_\ell(r_>/a)$ are modified spherical Bessel functions. For spherically symmetric ground state nuclei only the $\ell = 0$ term in the expansion survives. Thus only the following functions need to be considered:

$$i_0(r) = \frac{\sinh r}{r} \quad \text{and} \quad k_0(r) = \frac{e^{-r}}{r} \tag{4.1.7}$$

The potential of the spherically symmetric system then simplifies to become

$$U(r, \rho) = U_s(\rho(r)) + U_y(r) \tag{4.1.8}$$

where U_s is given in eqn.(4.1.1) and the finite range Yukawa potential is

$$\begin{aligned} U_y(r) &= \int v(\vec{r}, \vec{r'})\rho(\vec{r'})d^3r' \\ &= 4\pi V_0 \Big[\frac{e^{-r/a}}{r/a} \int_0^r dr' r'^2 \frac{\sinh(r'/a)}{r'/a} \rho(r') \\ &\quad + \frac{\sinh(r/a)}{r/a} \int_r^\infty dr'\, r'^2 \frac{e^{-r'/a}}{r'/a} \rho(r') \Big] \end{aligned} \tag{4.1.9}$$

When U of the expression above is inserted into the TFA (eqn.(4.1.2)) we find that it is no longer an algebraic equation in $\rho(\vec{r})$, hence constant density is not a solution. The self-consistent equation with the BKN potential reads

$$\frac{5}{3} C\rho^{2/3}(r) + U_s(\rho(r)) = \lambda_F - U_y(r); \qquad \lambda_F - U(r, \rho) \geq 0 \tag{4.1.10}$$

where

$$C = \frac{3}{10m} \Big(\frac{3}{4\pi} \frac{(2\pi\hbar)^3}{\gamma} \Big)^{2/3} \tag{4.1.11}$$

This equation is the semi-classical counterpart of the Hartree-Fock self-consistent equation for the nuclear ground state. The self-consistency condition for the wave-function has been replaced by the density function. Semi-classical method further constrains the range of the density to lie within a cut-off radius R through the condition $\lambda_F - U(\vec{r}, \rho) \geq 0$. The space of solutions, ρ, allowed must satisfy the particle number constraint

$$N = \int d^3 r \rho(r). \tag{4.1.12}$$

For the moment we will consider spin-isospin saturated system ($\gamma = 4$) with no Coulomb interaction.

The iterative procedure of solving eqn.(4.1.10) begins with a guessed density and λ_F. From these initial values

(1). we evaluate $U_y(r)$ (eqn.(4.1.9)), the Yukawa potential.

(2). Using the known λ_F and U_y from step (1) a unique function ρ in the interval $0 \leq r \leq R$ is evaluated from eqn.(4.1.10) . To avoid double valuedness of ρ, the parameters of the BKN interaction must be chosen such that the l.h.s. of eqn.(4.1.10) is single valued.

(3). We now check to ensure that the new $\rho(r)$ gives the correct particle number to a prescribed accuracy. If this is not fulfilled λ_F is adjusted using the particle number constraint

$$\begin{aligned} N &= \int d^3 r \rho(r) \\ &= \frac{4\pi}{3} \frac{\gamma}{(2\pi\hbar)^3} \int_0^R d^3 r \Big[2m(\lambda_F - U(r, \rho))\Big]^{3/2}. \end{aligned} \tag{4.1.13}$$

Once a new λ_F is obtained, steps (2) and (3) are repeated until the solution converges.

(4). Steps (2) and (3) iterate for correct λ_F and ρ with a fixed U_y given at step (1). U_y must then be updated with a new ρ. Having updated U_y, steps (2) and (3) are repeated. The self-consistent procedure converges when λ_F, ρ and U_y simultaneously converge. In practice, the convergence of λ_F is sufficient to ensure ρ and U_y converge also.

In the numerical procedure, outlined above, the functions were placed on sufficiently fine grid size $\Delta r = 0.0125$ fm and the λ_F value was calculated to 10 figures of accuracy. We further performed all the calculations with the grid size (or spacing) doubled but keeping the accuracy of λ_F unchanged. The self-consistent densities from these two cases agreed to 6 significant figures at each point on the grid. An additional test was also done to determine the uniqueness of the converged density. A necessary though not a sufficient test is to ensure uniqueness of the solution starting with drastically different initial densities. We took a square and a smooth Myers' density (see next paragraph) for this purpose. The solutions were found to be identical up to 6 figures at each point on the grid.

The self-consistent calculation was perfomed for ^4He, ^{16}O and ^{40}Ca nuclei with the BKN force parameters unaltered:

$$\begin{aligned} &A = -373.3 MeV fm^3, \qquad B = 3238.1 MeV fm^6, \qquad \sigma = 2 \\ &V_0 = -363.0 MeV \qquad a = 0.45979 fm \end{aligned} \tag{4.1.14}$$

The self consistent densities for these nuclei are shown in the first column of Fig. 4.1 . We have also overlapped an analytic density distribution given by the Myers' formula shown in dotted lines. This form of the density has a reasonable surface behaviour and we thus regard it as representing the experimental density distribution.

The Myers' density distribution for a nucleus of size A is given by [Mye 78]

$$\begin{aligned}\rho(r) &= \rho_0\left[1-(1+\frac{R}{\tilde{a}})e^{-R/\tilde{a}}\frac{\sinh(r/\tilde{a})}{r/\tilde{a}}\right] \quad r<R \\ &= \rho_0\left[\frac{R}{\tilde{a}}\cosh(R/\tilde{a})-\sinh(R/\tilde{a})\right]\frac{e^{-r/\tilde{a}}}{r/\tilde{a}} \quad r>R.\end{aligned} \tag{4.1.15}$$

where $R = 1.18A^{1/3}$ fm and $\tilde{a} = 1/\sqrt{2}$ fm. This density distribution has the property that its density gives the right number of particles $4\pi\int drr^2\rho(r) = \frac{4\pi}{3}\rho_0 R^3$ with the choice of R above and $\rho_0 = 0.145fm^{-3}$.

In all three nuclei (Fig. 4.1) the BKN force parameters give poor characterization of the nuclear surface. The central density is always higher than the Myers' distribution and the surface density decreases too rapidly. We contrast this to realistic surfaces obtained by Bonche, Koonin and Negele [BKN 76] where the self-consistent calculations were done in the Hartree-Fock approach. Evidently, the truncation of the kinetic equation at the lowest order in the $\hbar$-expansion has resulted in self-consistent densities that have poor characterization of nuclear surfaces. Since our approach to self-consistent solutions is quite different from the Hartree-Fock's, we have the freedom to choose a different set of parameters for self-consistent calculation. This freedom will be exploited in section 4.3 to improve upon the nuclear surface.

Even if the self-consistent density obtained is unique it does not follow that the energy of the system is minimized by this density. We are thus led to examine the stability of our solution to eqn. (4.1.10) . This is analogous to the question of stability of the Hartree-Fock solutions [Tho 61].

4.2 The variational principle and stability matrix

The solution we seek for the ground state must minimize the total energy of the system. The problem of obtaining an extremum and determining that it is a minimum of the total energy can be understood from the variational principle. The starting point is to construct an energy functional of the system and then take the first variation to obtain an extremum condition from which a solution is found. From the extremum solution the second variation is evaluated. Stability of the solutions requires the second variation to be positive definite.

The kinetic energy of a system of N nucleons is

$$T = \int d^3r d^3p \frac{p^2}{2m} f(\vec{r}, \vec{p}). \tag{4.2.1}$$

Upon using the Thomas-Fermi ansätz of the Wigner function, the kinetic energy functional becomes

$$T[\rho] = \int d^3r\, \tau(\vec{r}) = C \int d^3r \rho^{5/3}(\vec{r}) \tag{4.2.2}$$

where the coefficient C is given by

$$C = \frac{3}{10m}\left(\frac{3}{4\pi}\frac{(2\pi\hbar)^3}{\gamma}\right)^{2/3}, \tag{4.2.3}$$

and $\tau(\vec{r})$ is the kinetic energy density. The corresponding potential energy functional is

$$V[\rho] = \int d^3r \mathcal{V}[\rho(\vec{r})] \tag{4.2.4}$$

where the potential energy density is

$$\begin{aligned} \mathcal{V}[\rho(\vec{r})] &= \int_0^\rho U_s(\rho) d\rho + \frac{1}{2}\rho(\vec{r}) \int d^3r' \rho(\vec{r'}) v(\vec{r}, \vec{r'}) \\ &= \sum_{i=1}^{2} \frac{1}{\sigma_i + 1} C_i \rho^{\sigma_i + 1}(\vec{r}) + \frac{1}{2}\rho(\vec{r}) \int d^3r' \rho(\vec{r'}) v(\vec{r}, \vec{r'}) \end{aligned} \tag{4.2.5}$$

In line number two above, A and B Skyrme parameters have been relabelled as C_1 and C_2 respectively; and $\sigma_i \geq 1$. The sought-for energy functional, from eqns.(4.2.2) and (4.2.4) , is

$$\begin{aligned} E[\rho] =& T[\rho] + V[\rho] \\ =& C \int d^3r \rho^{5/3}(\vec{r}) + \\ & \sum_{i=1}^{2} \frac{1}{\sigma_i + 1} C_i \int d^3r \rho^{\sigma_i+1}(\vec{r}) + \frac{1}{2} \int d^3r d^3r' \rho(\vec{r'}) v(\vec{r}, \vec{r'}) \rho(\vec{r}) \end{aligned} \tag{4.2.6}$$

The variational parameter of $E[\rho]$ is the density itself.

When E[ρ] is expanded in Taylor series about the ground state ρ_0, we obtain [PN 62]

$$\begin{aligned} E[\rho] = E[\rho_0] + & \int d^3r h(\vec{r}) \delta\rho(\vec{r}) \\ & + \frac{1}{2} \int d^3r d^3r' \delta\rho(\vec{r'}) S(\vec{r}, \vec{r'}) \delta\rho(\vec{r}) + \ldots \end{aligned} \tag{4.2.7}$$

where the Hamiltonian can be identified to be

$$h(\vec{r}) = \frac{\delta E[\rho_0]}{\delta\rho(\vec{r})} \tag{4.2.8}$$

and the interaction energy matrix as

$$S(\vec{r}, \vec{r'}) = \frac{\delta^2 E[\rho_0]}{\delta\rho(\vec{r}) \delta\rho(\vec{r'})}. \tag{4.2.9}$$

At the moment $\delta\rho$ is an arbitrary small variation from ρ_0, the ground state density. The extremum condition for $E[\rho]$ subject to the particle number constraint is formally written as

$$\delta \Big\{ E[\rho] - \lambda \int d^3r \rho(\vec{r}) \Big\} = 0, \tag{4.2.10}$$

where λ is the Lagrange multiplier. From the second term of the Taylor expansion (eqn.(4.2.7)) this equation implies that

$$\int d^3r(h(\vec{r}) - \lambda)\delta\rho(\vec{r}) = 0 \tag{4.2.11}$$

We thus arrive at the extremum condition

$$h(\vec{r}) - \lambda = 0 \tag{4.2.12}$$

where the Hamiltonian (of eqn. (4.2.8)) is

$$h(\vec{r}) = \frac{5}{3}C\rho^{2/3}(\vec{r}) \quad + \sum_i C_i\rho^{\sigma_i}(\vec{r}) + \int d^3r' v(\vec{r},\vec{r'})\rho(\vec{r'}). \tag{4.2.13}$$

(from here on the subscript '0' of ρ_0 is suppressed). Now compare the extremum condition (eqn. (4.2.12)) to the self-consistent equation (4.1.10) we solved previously. With the identification $\lambda = \lambda_F$ they are seen to be identical. Hence, the self-consistent density obtained before corresponds to an extremum of the energy functional $E[\rho]$. Stated differently, the vanishing of the Poisson bracket (eqn. 2.2.36), from which the self-consistent solution was derived, is equivalent to the solution of the extremum condition (eqn.(4.2.12)). These two statements are equivalent because they are simply stating the equilibrium condition of the ground state in different forms.

The construction of the energy functional which enables the derivation of the self-consistent equation from the variational principle has served to reproduce known results. However, we can proceed a step further by examining the stability of the self-consistent solution. The derivation of the extremum condition requires the

explicit introduction of a Lagrange multiplier to constrain the particle number of the system. Alternatively, we can also explicitly state the constraint simply as

$$\delta N = \int d^3 r \delta\rho(\vec{r}) = 0 \tag{4.2.14}$$

From the extremum condition, $h(\vec{r}) = \lambda_F$, the first variation of the energy functional (eqn.(4.2.7)) vanishes due to the particle number constraint. So to guarantee that $E[\rho]$ evaluated at the ground state is a minimum the second variation must be positive definite

$$\frac{1}{2}\int d^3 r d^3 r' \delta\rho(\vec{r}) S(\vec{r},\vec{r'}) \delta\rho(\vec{r'}) > 0 \tag{4.2.15}$$

This condition may be physically interpreted as the excitational energy resulting from small departures from the ground state density ρ. A condition ensuring the stability condition (4.2.15) to hold is that the following eigenvalue equation

$$\int d^3 r' S(\vec{r},\vec{r'}) \delta\rho(\vec{r'}) = \epsilon \delta\rho(\vec{r}) \tag{4.2.16}$$

has only positive eigenvalues, $\epsilon > 0$. Upon performing the functional differentiation, the explicit form of the S-matrix reads

$$S(\vec{r},\vec{r'}) = \Big[\frac{10}{9} C \rho^{-1/3}(\vec{r'}) + \sum_i C_i \sigma_i \rho^{\sigma_i - 1}(\vec{r'})\Big] \delta(\vec{r} - \vec{r'}) + v(\vec{r},\vec{r'}) \tag{4.2.17}$$

We call this the stability matrix in view of its role in determining the stability of the self-consistent density. This is a (real) symmetric matrix due to the symmetric property of the Yukawa potential. It is curious that the second variation of the kinetic energy term is actually singular outside the nucleus. This ill-behaved S-matrix calls for special care in solving the eigenvalue equation (4.2.16) .

For each eigenvalue ϵ_i there is a corresponding eigenfunction ρ_i. Stability of the ground state requires that $\epsilon_i > 0$ for i's. Each $\delta\rho_i$ represents a variation away from the ground state. It is then possible to relate these eigenfunctions to the physical vibrational modes of the nucleus. We must, however, add a word of caution here since the eigenvalues, ϵ_i, do not have the dimension of energy instead they have the dimension of $MeVfm^3$. Nevertheless, this connection can be made, and the following chapter is exclusively devoted to the extraction of the solutions of stability equation (4.2.16) . These solutions will then be compared in detail with physical vibration modes. For this reason we have deferred the method employed to solve eqn. (4.2.16) . Suffice it now to mention that ϵ_i's are positive definite and that they are bounded from below.

4.3 Self-consistency with Coulomb interaction

Let us recall the parameters in the phenomenological BKN interaction. The BKN interaction is

$$U(\vec{r},\rho) = A\rho(\vec{r}) + B\rho^{\sigma}(\vec{r}) + V_0 \int d^3r' \frac{e^{-|\vec{r}-\vec{r'}|/a}}{|\vec{r}-\vec{r'}|/a}\rho(\vec{r'}) \qquad (4.3.1)$$

Parameters A and V_0 are negative which implies the interaction associated with them gives rise to attractive force. The interaction associated with parameter B, being positive, provides a repulsive force. The combination of the attractive and repulsive forces, which are the basic aspects of the nuclear forces, gives rise to the saturation of nuclear matter. In the nuclear matter limit this interaction reduce to the usual Skyrme interaction form

$$U(\rho_0) = (A + 4\pi V_0 a^3)\rho_0 + B\rho_0^{\sigma} \qquad (4.3.2)$$

where ρ_0 is the nuclear matter density. The Yukawa interaction, in this limit is proportional to ρ_0 and thus has been absorbed into the first term of the eqn. (4.3.1) . We observe that only in the case of finite systems has the Yukawa interaction brought any modifications to the Skyrme interaction.

Parameters A, B, V_0 and a can be adjusted to improve upon the properties of the nuclear system. It is, however, preferable to restrict the parameter space so as to retain the nuclear matter properties of the BKN interaction. The BKN interaction fixes the parameter combination $(A + 4\pi V_0 a^3)$, this results in a reduced parameter space of only two dimensions. Suppose the strength of A is increased, the binding energy would increase whereas increasing the range parameter a would increase the thickness of the nuclear surface and thereby reduces the binding energy. A proper choice of parameters should then optimize our demand for a reasonable binding energy and a good surface behaviour.

With these desired features in mind, we conducted a parameter search and concluded that the BKN interaction without the Coulomb interaction over-binds the nucleus. For example, the ^{40}Ca system with any reasonable parameters would give $E_b/A \approx -11$ MeV. To compare with experimental binding energy (see Table 4.2) we need to extend the BKN interaction to include the Coulomb interaction.

The Coulomb interaction removes the isospin degeneracy. This necessitates the distinction between the proton (ρ_p) and neutron (ρ_n) densites with $\rho = \rho_p + \rho_n$. The modified Wigner function with the degeneracy removed is given by

$$f(\vec{r},\vec{p}) = \frac{\gamma}{(2\pi\hbar)^3} \sum_{q=p,n} \Theta\Big(\lambda_q - U_q(\vec{r}) - \frac{p^2}{2m}\Big) \qquad (4.3.3)$$

where γ equals to 2 and q refers to the proton or neutron index. Protons and

neutrons now feel different potentials, and they are concisely written as

$$U_q(\vec{r}) = U_s(\vec{r}) + U_y(\vec{r}) + U_c(\vec{r})\delta_{qp} \tag{4.3.4}$$

The last term on the right of this equation is the Coulomb potential

$$U_c(\vec{r}) = e^2 \int d^3r' \frac{1}{|\vec{r} - \vec{r'}|} \rho_q(\vec{r'}) \tag{4.3.5}$$

The corresponding self-consistent equation for either the proton or neutron density is

$$\frac{5}{3} C \rho_q^{2/3}(\vec{r}) + U_s(\rho(\vec{r})) = \lambda_q - U_y(\vec{r}) - U_c(\vec{r})\delta_{qp}; \qquad \lambda_q - U_q(\vec{r}) \geq 0 \tag{4.3.6}$$

Equation (4.3.6) couples ρ_n and ρ_p through the Skyrme potential (i.e. the ρ-dependent terms). These coupled equations must be solved simultaneously. The calculational scheme is condensed in the flow chart attached. Initially we simply guess the values of λ_q and ρ_q from which the potentials $U_q(\vec{r})$ are evaluated. From these potentials we proceed to iterate eqn.(4.3.6) for ρ_q's until they converge; and we call this set of calculations loop A. Loop B adjusts the proton and neutron numbers separately, which results in new λ_q's. Loop A is an internal loop of B so it is iterated each time the λ_q's in loop B need to be adjusted. Having computed the densities ρ_q with the correct proton and neutron number, the potentials U_q are again updated. The outermost loop C ensures simultaneous convergence of ρ_q, λ_q and U_q. We performed this calculation with the same degree of accuracy as the previous self-consistent calculation.

We again conducted a parameter search with the new potential $U_q(\vec{r})$. The search was done for both the stiff ($\sigma = 2$) and soft ($\sigma = 7/6$) potentials. The stiff

potentials that optimize our desire for improved surface and reasonable binding energy are the STIFF1 and STIFF2 in Table 4.1. The attractive component of the STIFF1 potential is entirely absorbed in the Yukawa potential whereas the STIFF2 potential has a large range for parameter a with non-zero A parameter. Its surface behaviour is very similar to the STIFF1 (see Fig. 4.1 column 2 and 3) and the central density lies between those obtained with the BKN and STIFF1 potentials.

We have also displayed the proton and neutron self-consistent densities of the STIFF1 in Fig. 4.2 and their potentials for ^4He,^{16}O and ^{40}Ca in Fig. 4.3. Due to the presence of Coulomb repulsion the central density of the proton is always lower than neutron density, and the reverse is true at the surface. This behaviour at the surface is accidental for nuclei having equal number of protons and neutrons. Had we chosen an asymmetric system such as ^{208}Pb $(N > Z)$ the proton density would always be lower that the neutron density. It is worth noting that the lack of quantum effects has completely smoothed out the central density (see also ref [RS 80]) . Physically the ^{16}O nucleus is known to have maximum density not at the origin. This feature is, of course, beyond the scope of the Vlasov formalism. The potentials in Fig. 4.3 are likewise monotonically smooth. They display expected behaviours. Due to the finite range interaction, the potentials extend beyond the cut-off radius R. For the ^{40}Ca nucleus, the central potential's depth for protons is about $-40MeV$ and vanishes at 6 fm. From then onwards the Coulomb contribution completely dominates. The neutron potential is very similar to the proton potential apart from a shift in its depth due to the absence of Coulomb interaction. The depth reaches $-50MeV$ and the force extends as far as 8 fm.

The self-consistent density generated by the BKN interaction represents an improvement in the description of ground state nuclei over the conventional Skyrme interaction. The readjustment of the BKN interaction parameters further improve upon the surface density and gives good fits to the experimental binding energy.

4.4 Time evolution of the self-consistent density

In the preceeding section, the self-consistent densities were obtained for ground states possessing spherical symmetry. This allowed significant simplification in the extraction of the self-consistent densities. The method of generating the ground states will be used in chapter 6 to initialize colliding systems in heavy-ion reactions. In course of the reaction, the symmetry possessed by the ground states is destroyed by nucleus-nucleus interactions. Under such a circumstance, the dynamics must be solved in 3-D. The exercise of this section is to show how accurately the newly found ground states can be maintained with the numerical method outlined in chapter 2. In other words, we are testing the accuracy of the Vlasov dynamics. We perform this test for the ^{40}Ca nucleus in full 3-D computation.

Given the self-consistent proton and neutron densities of ^{40}Ca nucleus, we can Monte Carlo these distributions using the test particle method just as described in chapter 2. The momenta of the test particles are determined by the self-consistent densities through the relation $P_F(\vec{r}) \sim \rho^{1/3}(\vec{r})$. With 200 test particles per nucleon it is possible to map the self-consistent density very well as can be seen in Fig. 4.5 at t = 0 fm/c. Similarly, the rms radii and momenta of the nuclei were found to be almost exactly mapped.

From the self-consistent densities mapped by the test particles the potential energy is evaluated. The Yukawa and Coulomb potentials are respectively given by

$$U_y(\vec{r}) = V_0 \int d^3r' \frac{e^{-|\vec{r}-\vec{r'}|/a}}{|\vec{r}-\vec{r'}|/a} \rho(\vec{r'}) \tag{4.4.1}$$

and

$$U_c(\vec{r}) = e^2 \int d^3r' \frac{1}{|\vec{r}-\vec{r'}|} \rho_p(\vec{r'}) \tag{4.4.2}$$

Since the positions of all the test particles are known it might at the first glance be possible to compute the potentials directly. In practice, this straightforward method of evaluating the potentials is prohibitively long because the number of evaluations is proportional to the square of the number of test particles. A more efficient way is by solving for the potentials in their differential forms. The Yukawa potential is the solution of the equation

$$\left(\nabla^2 - \frac{1}{a^2}\right) U_y(\vec{r}) = -4\pi a V_0 \rho(\vec{r}) \tag{4.4.3}$$

and the Coulomb potential is the solution of the Poisson equation

$$\nabla^2 U_c(\vec{r}) = -4\pi e^2 \rho_p(\vec{r}) \tag{4.4.4}$$

These differential equations are solved by a standard numerical method (see Appendix). The above equation must also be supplemented by specified boundary conditions $U_y(\vec{r}_{bp})$ and $U_c(\vec{r}_{bp})$, where $\vec{r}_{bp}$ are the boundary points.

The total energy of the system can now be calculated and it is given by

$$\begin{aligned} E_T = & \frac{1}{\tilde{N}} \sum_{i}^{A\tilde{N}} \frac{p_i^2}{2m} \quad + \\ & \int d^3r V_s(\rho) + \frac{1}{2} \int d^3r \Big[U_y(\vec{r})\rho(\vec{r}) + U_c(\vec{r})\rho_p(\vec{r}) \Big] \end{aligned} \tag{4.4.5}$$

where $V_s(\rho)$ is the potential energy density of the Skyrme interaction (first term of eqn.(4.2.5)). Because of the local density fluctuations due to finite number of test particles used the nucleus is mildly excited. This excitational energy is approximately 2 MeV/A just as found in section 3.3.

The time evolution of the density at 0 , 30, 60 and 90 fm/c are exhibited in Fig. 4.5 . The surface of the nucleus is seen to be distorted somewhat but it retains much of its original character. At all times, it is more diffuse than the self-consistent density. This feature is an indication of the limitations in the use of numerical parameters and it is also reflected in the case with square density.

Chapter 5: The stability matrix and vibration modes

5.1 Introduction

The theoretical issues to be developed in this chapter are a direct extension of the last chapter. To recapitulate, it was found necessary to ensure the stability of the solutions of self-consistent equation (eqn. 4.2.12). The necessary condition for this to hold is that the eigenvalues of the stability matrix $S(\vec{r},\vec{r'})$ be positive definite, as expressed in eqn. (4.2.16). The equation in question is a linear integral equation whose solution is standard. In section 5.2, this equation will be solved by an expansion method. The eigenvalues will be shown to be positive definite for a chosen set of parameter called the STIFF1. This confirms that the self-consistent density obtained in the last chapter for this parameter set indeed minimizes the energy functional of the system.

The eigenfunctions corresponding to these eigenvalues display behaviours characteristic of giant (or collective) vibration modes as found in liquid drop and scaling models [BM 75]. We will show graphically the extent of agreement with these models. Having shown this we take a formal approach to the issue raised by the physical origin of the vibration modes seen in the eigenfunctions of the stability matrix. The mean field dynamics of the thesis is based on the time-dependent Vlasov equation (TDVE), so it seems entirely natural to develop the eigenmodes of nuclear vibrations from TDVE. The resulting solutions can then be compared with the eigenfunctions of the stability matrix. An exact solution of the TDVE is formidable, thus various approximations are invoked to solve it.

5.2 Eigen-solutions of the stability matrix

The stability equation to be solved is the linear integral equation

$$\epsilon g(\vec{r}) = \int d^3r' S(\vec{r},\vec{r'}) g(\vec{r'}) \tag{5.2.1}$$

where ϵ is the eigenvalue corresponding to eigenfunction $g(\vec{r})$ which was called the transition density in the last chapter. This eigenfunction is required to satisfy the particle number conservation

$$\int d^3r g(\vec{r}) = 0 \tag{5.2.2}$$

Eqn. (5.2.1) together with the constraint (5.2.2) forms the statement of our problem. We construct solutions of the multipole type

$$g(\vec{r}) = \tilde{g}_\ell(r) Y_{\ell m}(\theta,\phi) \qquad \ell = 0,1,2,... \tag{5.2.3}$$

where the radial function $\tilde{g}_\ell(r)$ is determined by the stability equation. Physical vibrations possessing this structure are well known in the nuclear liquid drop model [RS 80, BM 75]. We distinguish two types of solutions corresponding to $\ell = 0$ and $\ell \geq 1$:

$$\begin{aligned} g(\vec{r}) &= \tilde{g}_0(r) \qquad \ell = 0 \\ &= \tilde{g}_\ell(r) Y_{\ell m}(\theta,\phi) \qquad \ell \geq 1 \end{aligned} \tag{5.2.4}$$

These two kinds of solution are inherently distinct. Due to constraint (5.2.2) , $\tilde{g}_0(r)$ solution becomes a compressional mode whereas $\tilde{g}_\ell(r)$ ($\ell \geq 1$) solutions could be interpreted as surface modes of different multipole orders.

The solutions for the case $\ell \geq 1$ satisfies the constraint (5.2.2) automatically due to the presence of the spherical harmonics $Y_{\ell m}$. For $\ell = 0$ case, $\tilde{g}_0$ itself has

to be constructed to fulfill this constraint. We shall first discuss how to construct $\tilde{g}_0$ and then $\tilde{g}_\ell$. The technique to be employed throughout this section to solve eqn.(5.2.1) is the expansion of the radial functions in terms of a complete set of functions. We write

$$\tilde{g}_0(r) = \sum_{n=1}^{\infty} b_n^0 \varphi_n(r) \tag{5.2.5}$$

where b_n^0 are unknown coefficients to be determined by the stability equation. The basis functions φ_n are constructed from the product of spherical Bessel functions:

$$\begin{aligned} \varphi_n(r) &= j_0(k_0 r) j_0(k_n r) \qquad 0 \le r \le R \\ &= 0 \qquad r > R \\ k_n &= \frac{(n+1)\pi}{R}, \qquad n = 1, 2, \ldots \end{aligned} \tag{5.2.6}$$

where R is the cut-off radius. In this choice of R, we have confined the variation of $\tilde{g}_0(r)$ within the nucleus. This set of functions ensures $\tilde{g}_0$ will satisfy condition (5.2.2) . Since $\{j_0(k_n r)\}$ is a complete set of functions, the effect of multiplying a weighting factor $j_0(k_0 r)$ to the elements of this set does not change its completeness property.

The φ_n's are independent but not orthonormal to each other. They can be orthonormalized using the Gram-Schmidt procedure. We call the orthonormalized functions $\tilde{\varphi}_n$, so $\tilde{g}_0$ can now be written as

$$\tilde{g}_0(r) = \sum_{n=1}^{\infty} a_n^0 \tilde{\varphi}_n(r) \qquad \ell = 0 \tag{5.2.7}$$

where a_n^0's are the new coefficients. Since $\tilde{g}_0$ can only be determined up to a normalization constant we have the freedom to normalize it to unity:

$$\int d^3 r [\tilde{g}_0(r)]^2 = \sum_{n}^{\infty} [a_n^0]^2 = 1 \tag{5.2.8}$$

The construction of basis functions for $\ell \geq 1$ case is much simpler. We expand

$$\tilde{g}_\ell(r) = \sum_{n=1}^{\infty} a_n^\ell \tilde{\varphi}_n^\ell(r) \qquad \ell \geq 1 \tag{5.2.9}$$

where

$$\begin{aligned} \tilde{\varphi}_n^\ell(r) &= \frac{k_n}{\sqrt{2\pi R}} j_0(k_n r) \qquad r \leq R \\ &= 0 \qquad r > R \\ k_n &= \frac{n\pi}{R} \qquad n = 1, 2, ... \end{aligned} \tag{5.2.10}$$

With this choice of basis functions, $\{\tilde{\varphi}_n^\ell\}$ is a complete set of orthonormal functions. We also require the norm of $\tilde{g}_\ell$ be normalized to unity as in eqn.(5.2.8) . The unknowns in $\tilde{g}_0$ and $\tilde{g}_\ell$ are now contained in the coefficients a_n^0 and a_n^ℓ respectively. They are determined by the stability eqn.(5.2.1) .

When the multipole solution $\tilde{g}_\ell Y_{\ell m}$ is substituted into the stability equation the radial function $\tilde{g}_\ell$ satisfies an integral equation of the structure ($\ell \geq 0$)

$$\epsilon \tilde{g}_\ell(r) = v_s(r)\tilde{g}_\ell(r) + 4\pi V_0 \int dr' r'^2 \tilde{g}_\ell(r') f_\ell(r, r', a) \tag{5.2.11}$$

where the radial function of the Yukawa potential is given by

$$f_\ell(r, r', a) = i_\ell(r_</a) k_\ell(r_>/a): \tag{5.2.12}$$

and the kinetic plus the Skyrme potential part of the $S(\vec{r}, \vec{r'})$ matrix is

$$v_s(r) = \frac{10}{9} C \rho^{-1/3}(r) + \sum_{i=1}^{2} C_i \sigma_i \rho^{\sigma_i - 1}(r) \tag{5.2.13}$$

Upon substituting the expansions of $\tilde{g}_\ell$ ($\ell \geq 0$) in eqns.(5.2.7) and (5.2.9) , we obtain

$$\sum_{n=1}^{\infty} a_n^\ell \Big(\epsilon \tilde{\varphi}_n^\ell(r) - v_s(r)\tilde{\varphi}_n^\ell(r) - 4\pi V_0 \int dr' r'^2 \varphi_n^\ell(r') f_\ell(r, r', a) \Big) = 0 \tag{5.2.14}$$

Now multiply this expression by $\tilde{\varphi}^{\ell}_{m}$ and perform the volume integral with respect to the r variable to get

$$\sum_{n}\Big(\epsilon\delta_{nm} - S_{nm}\Big)a^{\ell}_{n} = 0 \tag{5.2.15}$$

where we have defined a stability matrix on the function space to be

$$\begin{aligned} S_{nm} = &\int dr r^2 \tilde{\varphi}^{\ell}_{n}(r) v_s(r) \tilde{\varphi}^{\ell}_{m}(r) + \\ &4\pi V_0 \int dr' dr (rr')^2 \tilde{\varphi}^{\ell}_{n}(r') f_{\ell}(r, r', a) \tilde{\varphi}^{\ell}_{m}(r) \end{aligned} \tag{5.2.16}$$

In matrix notation, the eigenvalue equation reads

$$\mathbf{S}\hat{a}^{\ell} = \epsilon^{\ell}\hat{a}^{\ell} \tag{5.2.17}$$

where the eigenvector $\hat{a}^{\ell} = (a^{\ell}_{1}, a^{\ell}_{2}, ...)$ and the eigenvalue for ℓ multipole is now labelled ϵ^{ℓ}. We have thus transformed the eigenvalue problem in the integral form (eqn.(5.2.1)) into a regular matrix diagonalization problem.

For each ℓ we have a different set of eigenvectors $\{\hat{a}^{\ell}\}$ corresponding to eigenvalues $\{\epsilon^{\ell}\}$. In this manner, each multipole mode ℓ has, in principle, an infinite number of solutions for an infinite size matrix. Before interpreting the eigenvalue ϵ^{ℓ} and eigenfunction $\tilde{g}_{\ell}$, the reliability of our diagonalization procedure ought to be considered. The only relevant spatial dimension in constructing S_{nm} is the radial coordinate. The basis functions $\tilde{\varphi}^{\ell}_{n}$ were placed on 1-D grid space of even grid size $\Delta r = 0.0125$ fm (the same grid size was used in the last chapter to find the self-consistent density). On the same grid space, the matrix elements S_{nm} were evaluated. S_{nm} is symmetric with respect to its indices so only those elements with $n \geq m$ need be evaluated. In the matrix diagonalization, the eigenvalue of interest for each ℓ is the lowest one. This permits us to truncate the dimension

(N) of S since the size of the matrix will determine the accuracy of this lowest eigenvalue or equivalently its eigenfunction as N is successively increased. In fact, there are two numerical parameters N and Δr. Convergence of a solution can only be secured by increasing N and refining Δr simultaneously. The parameter set we selected for study was STIFF1. We tried N from 25 to 200 and Δr in the interval $0.0125 - 0.050$ fm. Sufficient convergence of the eigenvalues was found for $N = 100$ with $\Delta r = 0.0125$ fm. The error in the eigenvalues in Table 5 is less then 0.5 $MeVfm^3$.

The stability of three symmetric systems was studied: ^{16}O,^{40}Ca and ^{208}Pb. Evaluation of S_{nm} requires that the self-consistent densities for these systems be known. The method of obtaining these densities has been extensively discussed in the last chapter. Table 5.1 displays the eigenvalues of the stability matrix for multipoles $\ell = 0 - 5$. The eigenvalues are indeed positive definite except for small (negative) values of the lowest eigenvalues seen in $\ell = 1$ case. These eigenvalues can be shown analytically to be zero from the stability equation because $\ell = 1$ case corresponds to the translational mode of the nucleus. Non-zero eigenvalues obtained here reflect the error in our numerics of approximately 0.3 $MeVfm^3$.

The eigenvalues of the stability matrix for $\ell = 0 - 5$ are summarized in Table 5.1. For each ℓ there are N number of eigenvalues but only the first four are displayed. They are characterized by the number of nodes of their corresponding eigenfunctions. For a fixed ℓ, the eigenvalue increases with the number of nodes of its eigenfunction. The $\ell = 0$ mode does not possess a zero-node eigenfunction in contrast to $\ell \geq 1$ modes. Apart from this difference, the eigenvalues of all ℓ's

are seen to increase with ℓ values. By inspection, they are seen to decrease with the size of the system. The dependence of the lowest eigenvalues on the size of the system and the number of nodes they possess are indicative of the physical vibration modes. We plotted the eigenfunctions corresponding to the lowest (first) eigenvalue for $\ell = 0$, 1 and 2 cases in Fig. 5.1. Striking characteristics of the lowest eigenfunctions are observed here. The first eigenfunction of the $\ell = 0$ case exhibits characteristics of a monopole transition density which has only one node. For $\ell = 1$, the lowest eigenfunction corresponds to the translational mode; and for $\ell = 2$ it corresponds to quadrupole surface vibration. As a measure of the agreement of these eigenfunctions with the physical transition densities we compare them to better known giant vibration modes.

Nuclear vibration can be viewed as a drop of classical fluid oscillating about its spherically symmetric equilibrium density ρ. For multipole mode vibrations $\ell \geq 1$, the fluid motion is assumed to be irrotational and incompressible:

$$\vec{\nabla} \times \vec{V}(\vec{r}) = 0; \qquad \vec{\nabla} \cdot \vec{V}(\vec{r}) = 0 \tag{5.2.18}$$

where $\vec{V}(\vec{r})$ is the velocity field of the fluid at $\vec{r}$. If we write $\vec{V}$ in terms of the velocity potential ϕ for irrotational fluid, $\vec{V}(\vec{r}) = -\vec{\nabla}\phi$, the incompressibility condition becomes

$$\nabla^2 \phi = 0 \tag{5.2.19}$$

The general solution of ϕ satisfying proper boundary conditions is a linear combination of $r^\ell Y_{\ell m}(\theta, \phi)$ functions. From the continuity equation, we have

$$\frac{\partial}{\partial t}\delta\rho = -\vec{\nabla} \cdot \left(\rho \vec{V}\right) = \vec{\nabla} \cdot \left(\rho \vec{\nabla}\phi\right) \tag{5.2.20}$$

The transition density for multipole vibration is obtained from this equation by substituting the solution of ϕ and assuming normal mode vibration. We obtain

$$\delta\rho_\ell(\vec{r}) \propto \ell r^{\ell-1}\rho'(r)Y_{\ell m}(\theta,\phi) \qquad \ell = 1,2,... \tag{5.2.21}$$

with $\rho'(r) = \frac{\partial}{\partial r}\rho(r)$. The radial dependence in $\delta\rho_\ell(\vec{r})$ can be identified with $\tilde{g}_\ell(r)$ in eqn.(5.2.9) . In fact, $\tilde{g}_\ell(r)$ can be shown directly from the stability equation to be proportional to r^ℓ in the vicinity of the origin. However, it is not obvious how the $\rho'(r)$ factor can be extracted from the same equation. In Fig. 5.2, the lowest eigenfunctions of the stability equation for $\ell = 2$ and 3 cases are compared to the transition densities of the liquid drop model (eqn.(5.2.21)). With the same equilibrium density ρ, comparisons are made for ^{16}O,^{40}Ca and ^{208}Pb nuclei. The agreement between them is almost perfect in the interior region and at the surface of the nucleus. The intermediate region of $\delta\rho_\ell(r)$ shows a slight deviation from $\tilde{g}_\ell(r)$.

Monopole mode involves the compression of nuclear density. The incompressible assumption $\vec{\nabla}\cdot\vec{V} = 0$ must certainly be relaxed in the derivation of its transition density. The velocity potential ϕ_0 for this mode is usually taken to be r^2. From the continuity equation, the monopole transition density with this velocity potential is

$$\delta\rho(r) \propto \Big(3\rho(r) + r\rho'(r)\Big) \tag{5.2.22}$$

Alternatively, if nucleon density distribution is scaled by a coordinate transformation $r \rightarrow \alpha r$, $\delta\rho$ again yields the expression above. Hence, $\delta\rho$ of this form is called the scaling transition density.

As can be seen in Fig. 5.3, the scaling density deviates substantially from $\tilde{g}_\upsilon$, the solution obtained from the stability equation. This deviation is particularly severe in the interior of the nucleus. $\tilde{g}_0$ shows almost no change in its character with nuclear size. It is flat throughout the nuclear interior but the scaling density changes significantly. Curiously enough, it seems to approximate $\tilde{g}_0$ very well for ^{208}Pb nucleus.

The monopole mode is not as well reproduced by $\tilde{g}_0$, but we must remark that the scaling density is an approximation of the eigenfunction of this mode. The similarity between the multipole mode solutions $\tilde{g}_\ell$ and $\delta\rho_\ell$ of the liquid drop model is particularly impressive. This remarkable similarity warrants a systematic examination of the physical origin of the eigenfunctions of the stability equation. Before doing so, we add the following comments. In the limit of small amplitude motion, $\rho = \rho_0 + \delta\rho(t)$, the density matrix form of the TDHF equation can be linearized to read [RS 80]

$$(\mathcal{S} - \hbar\omega_\nu)\delta\rho_\nu = 0 \tag{5.2.23}$$

The stability matrix $\mathcal{S}$ is precisely the R.P.A. matrix used to find the eigenmodes of physical vibrations. This is entirely similar in structure to the stability equation ((5.2.17)). It should be stressed that our stability equation is derived from static considerations but eqn.(5.2.23) is deduced from the TDHF dynamics. To show the full analogy between the semi-classical and the quantum approaches, we have to derive a similar statement to eqn.(5.2.23) from the TDVE in the small amplitude limit. This derivation will be followed in the next section. The algebra involved will be considerable. Chapters 6 is independent of the results of this section.

5.3 Vibration modes in the linearized Vlasov approach

Various approximations of the Vlasov equation have been advanced by several authors to understand nuclear vibration modes within the semi-classical method. Significant progress in this area has been achieved by authors in refs. [BDD 86, BDi 88]. In their most recent work [BDi 88] the linearized Vlasov equation is solved self-consistently with separable forces. Works with externally induced forces [KSS 86] have also been discussed. The connection of vibrations in the nuclear matter limit within the semi-calssical approach to the Fermi liquid parameters of the Landau theory has been explored [JJ 80].

Our aim is to compare as closely as possible the solution of the linearized Vlasov equation to the eigenfunctions of the stability equation. The works cited do not have the desirable approximation for our purpose. In particular, we seek to retain the residual interaction $\delta U(\vec{r},t)$ without making any assumption about its structure. The transition density is then solved self-consistently with this δU.

The linearized continuity equation for small departures from the equilibrium configuration

$$f(\vec{r},\vec{p},t) = f_0(\vec{r},\vec{p}) + \delta f(\vec{r},\vec{p},t) \tag{5.3.24}$$

is written as

$$\frac{\partial}{\partial t}\delta\rho(\vec{r},t) = -\vec{\nabla}\cdot\delta\vec{J}(\vec{r},t) \tag{5.3.25}$$

The transition current in this equation takes the form

$$\delta\vec{J}(\vec{r},t) = \int d^3p \frac{\vec{p}}{m}\delta f(\vec{r},\vec{p},t) \tag{5.3.26}$$

If we take the second order time derivative of the continuity equation, we get

$$\frac{\partial^2}{\partial t^2}\delta\rho(\vec{r},t) = -\vec{\nabla}\cdot\frac{\partial}{\partial t}\delta\vec{J}(\vec{r},t) \tag{5.3.27}$$

The time derivative of $\delta\vec{J}(\vec{r},t)$ in its explicit form reads

$$\frac{\partial}{\partial t}\delta\vec{J}(\vec{r},t) = \int d^3p\frac{\vec{p}}{m}\frac{\partial}{\partial t}\delta f(\vec{r},\vec{p},t)$$

We appeal to the Vlasov equation to substitute for $\frac{\partial}{\partial t}f$ from which we obtain

$$\frac{\partial}{\partial t}\delta\vec{J}(\vec{r},t) = \int d^3p\frac{\vec{p}}{m}\Big(-\frac{\vec{p}}{m}\cdot\vec{\nabla}\delta f + \vec{\nabla}U_0\cdot\vec{\nabla}_p\delta f + \vec{\nabla}\delta U\cdot\vec{\nabla}_p f_0\Big) \tag{5.3.28}$$

where U_0 is the (self-consistent) ground state potential. After performing a few integrals this equation simplifies to become

$$\frac{\partial}{\partial t}\delta\vec{J}(\vec{r},t) = -\Big(\frac{2}{m}\vec{\nabla}\cdot\delta\overleftrightarrow{T} + \frac{\delta\rho}{m}\vec{\nabla}U_0 + \frac{\rho}{m}\vec{\nabla}\delta U\Big) \tag{5.3.29}$$

where ρ is the ground state density and the kinetic energy tensor of the vibrating system is

$$\delta\overleftrightarrow{T}(\vec{r},t) = \int d^3p\frac{\vec{p}\vec{p}}{2m}\delta f(\vec{r},\vec{p},t) \tag{5.3.30}$$

Time dependence is now contained in δU, $\delta\rho$, $\delta\overleftrightarrow{T}$ and of course δf. Equation (5.3.27) , from the results above, becomes

$$m\frac{\partial^2}{\partial t^2}\delta\rho = 2\vec{\nabla}\vec{\nabla}:\delta\overleftrightarrow{T} + \vec{\nabla}\cdot\Big(\delta\rho\vec{\nabla}U_0 + \rho\vec{\nabla}\delta U\Big) \tag{5.3.31}$$

where : denotes the tensor product. The kinetic energy term may be written in a more transparent way. We write

$$\begin{aligned}\vec{\nabla}\vec{\nabla}:\delta\overleftrightarrow{T} &= \frac{1}{2m}\int d^3p(\vec{p}\cdot\vec{\nabla})(\vec{p}\cdot\vec{\nabla})\delta f \\ &= \frac{1}{3}\nabla^2\int d^3p\frac{p^2}{2m}\delta f + \frac{1}{3m}\int d^3p\Big(\frac{3\vec{p}\cdot\vec{\nabla}\vec{p}\cdot\vec{\nabla} - p^2\nabla^2}{2}\Big)\delta f\end{aligned} \tag{5.3.32}$$

If we define the change in the kinetic energy of the system due to small variation as

$$\delta T(\vec{r},t) = \int d^3p \frac{p^2}{2m}\delta f \tag{5.3.33}$$

and the tensor components of the quadrupole moment (in the momentum space) as

$$Q_{ij}(\vec{r},t) = \frac{1}{m}\int d^3p(3p_ip_j - p^2\delta_{ij})\delta f(\vec{r},\vec{p},t) \tag{5.3.34}$$

then eqn. (5.3.31) becomes

$$m\frac{\partial^2}{\partial t^2}\delta\rho = \frac{2}{3}\nabla^2\delta T + \frac{1}{3}\vec{\nabla}\vec{\nabla} : \overleftrightarrow{Q} + \vec{\nabla}\cdot(\delta\rho\vec{\nabla}U_0 + \rho\vec{\nabla}\delta U) \tag{5.3.35}$$

This is the general result of the linearized Vlasov equation. Specific approximations will be made to this equation in subsequent developments. The equation of motion for the displacement function $\delta\rho$ depends on both the variation of the kinetic and potential functions. Kinetic contributions come in parts: the first term depends on the diagonal or P_0 deformation of Fermi sea in δf whereas the second term depends on its quadrupole moment. Evaluation of $\overleftrightarrow{Q}$ poses some difficulty as we will encounter shortly. Therefore, specific approximations will be made to this equation.

To maintain consistency with the last chapter we must take the nuclear ground state to be

$$f_0(\vec{r},\vec{p}) = \frac{\gamma}{(2\pi\hbar)^3}\Theta\Big(p - p_F(\vec{r})\Big) \tag{5.3.36}$$

We restrict the variation from f_0 to the Fermi surface

$$\delta f(\vec{r},\vec{p},t) = \delta F(\vec{r},\hat{p},t)\delta(p_F(\vec{r}) - p) \tag{5.3.37}$$

In the single-particle shell model this approximation is equivalent to confining transition of levels in the vicinity of the Fermi surface.

The transition density and kinetic energy in this approximation are respectively

$$\delta\rho(\vec{r}) = p_F^2(\vec{r}) \int d\Omega_p \delta F(\vec{r}, \hat{p}, t) \tag{5.3.38}$$

and

$$\begin{aligned} \delta T(\vec{r}, t) &= \frac{5}{3} C \rho^{2/3}(\vec{r}) \delta\rho(\vec{r}, t) \\ C &= \frac{3}{10m} \Big(\frac{3}{4\pi} \frac{(2\pi\hbar)^3}{\gamma} \Big)^{\frac{2}{3}} \end{aligned} \tag{5.3.39}$$

Let us focus on the following terms of equation (5.3.35)

$$\frac{2}{3} \nabla^2 \delta T + \vec{\nabla} \cdot \Big(\delta\rho \vec{\nabla} U_0 + \rho \vec{\nabla} \delta U \Big) \tag{5.3.40}$$

The first term in the above equation can be written as

$$\vec{\nabla} \cdot \Big(\frac{10}{9} C \rho^{-1/3} \delta\rho \vec{\nabla}\rho \Big) + \vec{\nabla} \cdot \Big(\rho \vec{\nabla} (\frac{10}{9} C \rho^{-1/3} \delta\rho) \Big) \tag{5.3.41}$$

To evaluate the second term, we use the extremum condition (eqn.(4.2.12))

$$U_0 = \lambda_F - \frac{5}{3} C \rho^{2/3} \tag{5.3.42}$$

to get

$$\vec{\nabla} \cdot \Big(\delta\rho \vec{\nabla} U_0 \Big) = -\vec{\nabla} \Big(\frac{10}{9} C \rho^{-1/3} \delta\rho \vec{\nabla}\rho \Big) \tag{5.3.43}$$

This term cancels the first term of eqn.(5.3.41) so eqn.(5.3.40) simplifies to

$$\vec{\nabla} \cdot \Big(\rho \vec{\nabla} \delta h \Big) \tag{5.3.44}$$

The variation of the hamiltonian in this expression is

$$\delta h(\vec{r}, t) = \frac{10}{9} C \rho^{-1/3}(\vec{r}) \delta\rho(\vec{r}, t) + \delta U(\vec{r}, t) \tag{5.3.45}$$

When the residual potential δU is written explicitly, it reads

$$\delta U(\vec{r},t) = \sum_{i=1}^{2} C_i \sigma_i \rho^{\sigma_i - 1}(\vec{r}) \delta\rho(\vec{r},t) + \int d^3r' v(\vec{r},\vec{r'}) \delta\rho(\vec{r'},t) \tag{5.3.46}$$

From here, we can cast δh in terms of the stability matrix

$$\delta h(\vec{r},t) = \int d^3r' S(\vec{r},\vec{r'}) \delta\rho(\vec{r'},t) \tag{5.3.47}$$

Our final form of the approximated linearized Vlasov equation is

$$m\frac{\partial^2}{\partial t^2}\delta\rho = \vec{\nabla}\cdot(\rho\vec{\nabla}\delta h) + \frac{1}{3}\vec{\nabla}\vec{\nabla} : \overleftrightarrow{Q} \tag{5.3.48}$$

The first term is a functional of $\delta\rho$ but the second term is not. To evaluate Q_{ij} the structure of δf must be known. For this reason eqn.(5.3.48) describing oscillations of finite systems is not an eigenvalue equation with $\delta\rho$ as its eigenfunction. If the quadrupole deformation of the Fermi sea can be regarded as small the contribution of Q_{ij} term may be neglected. This approximation is certainly compatible with the liquid drop model. Even in the stability equation ($\epsilon\delta\rho = \vec{\nabla}\delta h$) no information of the P_2 deformation is required. With this additional approximation eqn.(5.3.48) simplifies to

$$-m\omega^2\delta\rho = \vec{\nabla}\cdot\left(\rho\vec{\nabla}\delta h\right) \tag{5.3.49}$$

This equation is now linear in $\delta\rho$ and therefore it is an eigenvalue equation that can be solved in a similar manner to that used to solve stability equation. Notice the difference in structure between the stability and this equation. In the nuclear matter limit, we recover an old result [JJ 80]

$$(\nabla^2 + k^2)\delta\rho(\vec{r}) = 0 \tag{5.3.50}$$

where k is a constant.

The lowest eigenfunctions for different ℓ values of eqn.(5.3.49) are compared to the eigenfunctions of the stability equation and the transition densities of the liquid drop model in Fig. 5.2. ℓ equals 2 and 3 cases are shown; the agreement between the eigenfunctions of eqn.(5.3.49) and stability matrix is almost exact. Fig. 5.2 shows their eigenfunctions are exactly overlapped thereby giving us the assurance of the intimate connection between eqn.(5.3.49) and the stability equation. The monopole ($\ell = 0$) displays character quite different from the stability equation for all the systems evaluated (see Fig. 5.3). Moreover, the eigenfunctions show little or no change in character with the size of the system unlike the scaling transition density.

Further progress in the evaluation of the monopole mode is made by keeping the quadrupole term. Lee and Cooper [LC 88] suggested expanding δf in the form

$$\delta f(\vec{r},\hat{p},t) = \delta(p - p_F(r)) \sum_l F_l(r,t) P_l(\cos\theta_{\vec{r}\cdot\vec{p}}) \qquad (5.3.51)$$

which includes all higher order deformations in the Fermi sea. F_l are now the unknowns to be determined by eqn.(5.3.49) . Because of the gradient operation on the quadrupole term the deformations of different orders are coupled leading to an infinite set of equations to be solved self-consistently. They truncated this set of equations at $l = 3$ and found a slight change in the eigenfunctions of the monopole mode. Truncating this set of equations at higher l considerably complicates the problem. Thus it is not certain how closely the monopole mode of the Vlasov approach can reproduce the eigenfunction $\tilde{g}_0$ of the stability equation.

Chapter 6: Peripheral interactions of ^{40}Ar on ^{27}Al

6.1 Preliminary discussion

The specific reaction selected for detailed study in this chapter is

$$^{40}Ar(44MeV/A) +^{27} Al \rightarrow^{34} X + others$$

where ^{34}X is any projectile-like fragment (PLF) of size A = 34. We singled out this reaction because the properties of its PLF and TLF (target-like fragments) have been extensively measured [Day 86, Heu 87, Day 89]. We will examine the validity of the elements of our model using both the inclusive and exclusive data measured. Authors in ref. [Gré 87] have performed calculations of this reaction with the standard BUU model [BKD 84]. Because of the lack of fluctuation mechanism in this model the authors confined their findings to the averaged properties of the PLF.

The model of nuclear dynamics to be tested in this chapter represents the culmination of the successive stages of theoretical development pursued in chapters 2 and 4. This model consists of four basic elements; they are the collision mechanism responsible for the generation of fluctuations, nucleon-nucleon cross-section, mean field and nuclear surface. In the following, we make a few minor changes in the ingredients of our model and state the specific mean field parametrization to be employed. It is known that the low energy ($E_{lab}/A \leq 50MeV$) free nucleon-nucleon cross-sections show the lack of angular dependence. This permits us to replace the cross-section used in chapter 3 (eqn. 2.3.10) by an isotropic one. We further set the total cross-section to be 55 mb.

The potential of the BKN-type with the STIFF1 parametrization (see Table 4.1) will be used. This potential is used in conjunction with the Coulomb potential. The resultant self-consistent ground state densities associated with this potential (BKN plus Coulomb) were obtained for various systems in chapter 4.

6.2 Initialization and error analysis

The colliding nuclei were initially set up in the CM frame with the reaction plane defined by the X and Z axes. We chose the Z-direction to be the direction of the beam momentum. Before the nuclei interact through their nuclear potentials they were initialized to be on a Coulomb trajectory. At a distance R_i between the centers of the nuclei, sufficiently far for the nuclear potentials not to interact, the components of the beam momentum are altered by the Coulomb potential according to

$$P_x = P_t \cos\theta_i - P_r \sin\theta_i \tag{6.1.1}$$

$$P_z = P_t \sin\theta_i + P_r \cos\theta_i \tag{6.1.2}$$

where θ_i is the angle between the vector $\vec{R}_i$ and the Z-axis. The tangential and radial components of the momentum are derived from the conservation of the total angular momentum ℓ and kinetic energy E_{cm} in the CM

$$P_t = \frac{\ell}{R_i} \tag{6.1.3}$$

$$P_r = \left[2\mu\left(E_{cm} - \frac{\ell^2}{2\mu R_i^2} - \frac{\alpha}{R_i}\right)\right]^{\frac{1}{2}} \tag{6.1.4}$$

where μ is the reduced mass and $\alpha = Z_T Z_P e^2$. Angle θ_i is obtained from the solution of the equation of motion [Gol 81], it is given by

$$\theta_i = \cos^{-1}(\frac{1}{\epsilon}) - \cos^{-1}\left[\left(\frac{\ell^2}{\mu\alpha R_i} + 1\right)/\epsilon\right] \tag{6.1.5}$$

where ϵ is the eccentricity

$$\epsilon = \left[\left(\frac{2E_{cm}b}{\alpha}\right)^2 + 1\right]^{\frac{1}{2}} \tag{6.1.6}$$

Having initialized the nuclei to be on a Coulomb trajectory the subsequent motion was determined numerically.

We performed this calculation using configuration space grid size of 1 fm, time discreteness (δt) of 0.5 fm/c and a total of 100 test particles per nucleon. To ensure numerical stability with these parameters, we calculated time evolved quantities of the ground state ^{40}Ar and ^{27}Al. The diffuse surfaces of the nuclei were found to be maintained for at least 150 fm/c. We then tested the effectiveness of the Pauli blocking routine; it was found to block 95% of the attempted collisions. In a typical simulation for systems considered here there are about 200 attempted collisions. Therefore the number of spurious collisions is approximately 10. The effect of this error could be reflected in the deformation of the nucleus in configuration and momentum space, and the loss of particles. We quantified the extent of the deformation by evaluating $\langle r_i^2 \rangle$ and $\langle p_i^2 \rangle$ where i is the component index. The sphericity of the ground state measured by these quantities was preserved to a good accuracy after 80 fm/c - a period after which the ions would have ceased to interact. The loss of particles in the same period was 0.5 nucleons for both argon and aluminium nuclei.

Our objective is to study $^{40}Ar + ^{27}Al \rightarrow ^{34}X + others$. Restricting to ^{34}X only requires prohibitive computing to generate enough statistics hence we will consider masses between 32-36, and compare with experimental results. This corresponds to integrating the impact parameter in the range 5.76-7.76 fm. In fact, our calculation shows an almost linear relationship between the average size of the PLF and impact parameter, as shown in Fig. 6.1. In this range, the collision rate diminishes after a period of 80 fm/c and the final state spectator nuclei approached their respective Coulomb trajectories by 150 fm/c. An accurate determination of the projectile (or target) trajectory is required to ensure precision in the angular distribution. We performed a test calculation in CM with ^{40}Ar and ^{27}Al nuclei sufficiently far from each other so as to prevent their nuclear forces from interacting. To avoid long range interaction the Coulomb was not included in this calculation. The magnitudes of their momenta were changed by less than 1 MeV/c per nucleon. which is indeed accurate.

The BUU code with fluctuations generates an event for each simulation. We compiled 110 simulations in the impact parameter range specified. Of these events, 81 were accepted after applying the momentum and mass cut. To be consistent with the experimental cut in the PLF momentum, we accepted only those events with $P_z \geq 0.8P_0$ in the lab, where P_0 is its beam momentum. The average value of the mass for nuclei in the mass range 32-36 is 34.4. Fig. 6.2 shows the mass distribution of the PLF and TLF. It can be seen that the spectrum is divided between the PLF and TLF. The mass distribution of PLF is sharply peaked at 34-35 whereas the TLF distribution shows more dispersion.

6.3 Results and interpretation

The angular distribution of the PLF from our model and experiment [Day 86] are shown in Fig. 6.3. Both results show a rapid drop of yield in the angular range $2° - 10°$, in the lab. All angles of the PLF from our calculations are negative which signifies the domination of the mean field over the collision dynamics. This information can not be extracted from the experiment however. The experimental distribution is more forwardly peaked than our result. The correlated TLF angular distribution is shown in Fig. 6.4. Experimentally, this distribution is obtained by selecting only those TLF that are in coincidence with the PLF at 3.1° [Heu 87]. It is clearly beyond our computational ability to duplicate this result, consequently, the model calculation shown in histogram of Fig. 6.4 corresponds to TLF in coincidence with all PLF in Fig. 6.3. This amounts to allowing some angular spread in the PLF. Our model shows a Gaussian-like distribution similar to the experimental data and with the correct peak position (experimental plot here is for A=32; A=36 case shows similar behaviour but with its peak located at an angle higher by $\approx 10°$). The full width at half-maximum (FWHM) of the histogram is about $20° - 30°$ compared to the exprimental value of 50°. Thus our model underpredicts the FWHM of TLF angular distribution and it also shifts the maximum in the yield of the angular distribution of PLF.

It is instructive to calculate the scattering angle of the PLF without the contamination of the collision dynamics. This was done by switching off the collision routine of our program. The spectrum of the scattering angles of PLF is plotted in Fig. 6.5 for scattering in the impact parmeter range 0-11 fm. The scattering

angles are negative for $b < 9.5$ fm and positive beyond this impact parameter. At $b = 9.5$ fm, the Coulomb repulsion exactly cancels the attractive nuclear mean field. The highest scattering angle obtained is $-11.5°$, and it occurs at $b = 5.0$ fm. Similar curves can be obtained with more sophisticated dynamical approach such as the TDHF. There is, however, no such existing calculation for the specific reaction considered here. In the full calculation, events were obtained from collisions in the impact parameter range 5.76-7.76 fm. Within this range the result of the potential scattering gives angles ranging from $-4°$ to $-11°$. Comparing this result to the angular distribution of the PLF of full calculation (Fig. 6.3) we find the collision effects have advanced the scattering to the front region by $\sim 2°$. The yield in the forward region, however, remains low in comparison to the experiment.

The TLF angular distribution in Fig. 6.4 contains more relevant information. Potential scattering, discussed in the last paragraph, gives a FWHM of the angular distribution of TLF of only 10° in the impact parameter range 5.76-7.76 fm; its peak lies somewhere between 60° and 70°. Comparing these results with those of the full calculation (i.e. with collisions) in Fig. 6.4, we infer two measurable effects of collisions. The peak of the TLF angular distribution is down shifted by $\approx 20°$. This effect is explained by the additional momentum transfer from the projectile to the target due to collisions. As remarked before, the peak of the TLF angular distribution (Fig. 6.4) is positioned close to the observed peak.

At a fixed impact parameter potential scatterings do not generate any angular dispersion. The small FWHM (10°) seen in the potential scattering is due to integration over the impact parameter. The increase in FWHM due to collisions

is about 20°. This amount of FWHM increase measures the extent of weakening in the target-projectile correlations due to collisions. Data from GANIL [Heu 87, Day 89] show a gradual increase of FWHM with the number of particle loss in the projectile. In other words, larger FWHM is associated with more central collisions hence more nucleon-nucleon collisions.

From the interpretation given to the FWHM of the TLF angular distribution, we attribute its smallness obtained in our model to the lack of fluctuations or randomness generated by the collision dynamics. The model's collision dynamics is constructed from two basic ingredients, namely the nucleon-nucleon cross-section and the treatment of fluctuations as explained in chapter 2. Present calculations do not permit the separation of the effects of each factor of the collision dynamics. More systematic investigations are required to test especially the sensitivity of nucleon-nucleon cross-section to observables presented in this chapter.

For peripheral interactions more realistic nuclear density profiles than those obtained (in chapter 4) might be needed. This would entail the introduction of more refined interactions in our self-consistent density calculation or to go beyond the Thomas-Fermi approximation. These considerations are worth exploring.

Results of correlations between the TLF and PLF are shown in Figs. 6.6 and 6.7. Figure 6.6 shows the correlation between the angles of the TLF and masses of the PLF. In Fig. 6.7, the correlation between their masses are exhibited. In both figures, the experimental points are obtained for the TLF in coincidence with the PLF at 3.1° [Heu 87]. This angular cut has not been imposed on the results of model calculation. Comparison with data in Figs. 6.6 and 6.7 should be made in

the mass range 32-36 of the PLF because of the limitation in the range of impact parameter spanned in model calculation. Within this mass range of the PLF, the model data points follow the experimental points rather well in both Figs. 6.6 and 6.7. The physics contained in the overall features of these results are readily interpreted. As the PLF mass increases the corresponding impact parameter also increases (see Fig. 6.1). Collisions at higher impact parameters tend to impart less longitudinal momentum to the target than those at lower impact parameters. It is clear that larger momentum transfer to the target implies that its remnants (TLF) will emerge into more forward angles. In Fig. 6.7 the mass loss in the projectile is measured against the corresponding mass loss in the target. This relationship is not linear and it is borne out by our model.

In summary, the BUU based model with fluctuations has enabled us to analyse and interpret the properties of the PLF and its correlated TLF. The basic features of their angular distributions are reproduced. The dependence of the angle and mass of TLF on the mass of PLF is very well described by the model.

Chapter 7: Conclusion

In the present chapter, the relevance of this work to the intermediate energy collisions is assesed and its significance in the wider context of heavy-ion research is exposed. We will also provide indications for the future development of the BUU model with fluctuations. Results derived from the semi-classical analysis of the nuclear vibrations are summarized.

The objective of this thesis is to use the BUU model fluctuations in describing aspects of intermediate energy collisions. We performed the calculations at 44, 72, 92 and 100 MeV/A, concentrating on experimental observables such as the mass distribution, momentum distribution of the projectile-like fragments, and target-projectile correlations. The exploratory calculations in chapter 3 involving the properties of spectator fragments (angular and momentum distributions) provided qualitative agreements with the experiments. This suggests that the BUU model has combined the essential elements necessary to explain these observables. The BUU model, we reiterate, combines both the mean field and collision dynamics, and at all times the fermion statistics is obeyed.

We proceeded from there to examine the quality of the mass distributions of the spectator and participant fragments. The trend of the participant mass distribution was reproduced but the production of light particles ($A \leq 10$) was underpredicted. This discrepancy is attributable in part to non-conservation in energy in the numerical computation (see section 2.4) and shell effects. The latter consideration clearly lies beyond the scope of our semi-classical treatment but the energy non-conservation can be remedied by abandoning the point (test) particles

in the decomposition of the phase-space for particles with finite spatial extent [Len 88]. The work on the influence of this factor to the quality of mass distribution is in progress [Gal 88]. This effect is purely numerical in origin and it has no connections with the essentials of the BUU model.

In chapter 6, we introduced refinements into the model by propagating a finite range mean field and using an isotropic nucleon-nucleon cross-section appropriate for lower energy reactions. Formalism developed in chapter 4 showed that this finite range interaction generates ground state densities with adequate surface diffusiveness. With these refinements, we embarked on calculations aimed at detailed comparison with the experiments. Characteristic features of the inclusive and exclusive spectator observables were successfully reproduced. For the purpose of future development of the BUU model, we shall now emphasize the main weaknesses of the model.

The quality of the angular distribution of projectile-like fragments and its correlated target-like fragments need to be improved. These aspects of the data are related to two competing factors: the mean field and collision dynamics. The uncertainties lie chiefly in the nucleon-nucleon cross-section, and possibly in the way the fluctuations are generated (section 2.4). The present study is not sufficiently systematic to enable us to disentangle the influence of each factor on observables. Further studies in this direction are called for.

The determination of corrections to free nucleon-nucleon cross-section in the medium would be in its own right a valuable contribution to nuclear physics. The major in medium modification, namely the Pauli blocking, is already taken into ac-

count in our model. Furthermore, theoretical investigations on the nature of single-particle fluctuations in the reaction process would greatly enrich our understanding of non-equilibrium phenomena. These aspects of heavy-ion studies highlight the scope offered by the field.

On the whole, this thesis demonstrates the strength of the BUU model with fluctuations in explaining diverse aspects of the participant and spectator observables. Contemporary complementary models for nuclear fragmentation based on statistical ideas [FR 82, 83, Koo 86] are incapable of providing a unified approach to these observables in the manner the BUU model has. From a wider perspective, the sample calculations of this thesis complement the success of the model at higher energies ($0.4 \leq E_{lab}/A \leq 1GeV$) [BDa 88].

The development of the semi-classical theory of nuclear ground states in chapter 4 and nuclear vibrations in chapter 5 provides an alternative view of the subject to more complicated quantum mechanical TDHF and RPA theories. We first extracted the nuclear ground state densities from the extremum condition of the energy functional of the system. In this calculation, Coulomb contribution was explicitly built into the energy functional and the entire problem was solved in 3-D with spherical symmetry. This piece of work is a direct extension of Maddison and Brink's work [MB 81]. The stability of our ground state solutions was then examined through the stability matrix. We showed their stability implies that the stability matrix must possess only positive eigenvalues. The content of this statement is analogous to the stability of the ground state solutions of the Hartree-Fock equation. Proceeding further in our semi-classical approach, the eigenfunctions of our stability matrix

were shown to possess the character of giant vibration modes which includes the monopole and multipole modes.

Further advance was made in section 5.3 when the eigenfunctions of the multipole modes ($\ell \geq 1$) of the linearized Vlasov equation were shown to be the same numerically to the ones obtained by diagonalizing the stability matrix. The formal equivalence of the these appoaches remains to be proven however. The development of semi-classical theory of nuclear ground state and nuclear vibration modes in this thesis parallels those in quantum theories.

Appendix

Numerical solution of the Yukawa and Coulomb potentials

The Yukawa and Coulomb potentials are respectively

$$\phi_y(\vec{r}) = V_0 \int d^3r_1 \frac{e^{-|\vec{r}-\vec{r}_1|/a}}{|\vec{r}-\vec{r}_1|/a}\rho(\vec{r}_1)$$

and

$$\phi_c(\vec{r}) = e^2 \int d^3r_1 \frac{1}{|\vec{r}-\vec{r}_1|}\rho_p(\vec{r}_1)$$

The nucleon and charge (proton) density distributions are ρ and ρ_p reaspectively. These potentials are special cases of the solution of the differential equation

$$-\left(\frac{\partial^2}{\partial x^2} + \frac{\partial^2}{\partial y^2} + \frac{\partial^2}{\partial z^2} + k^2\right)\phi(x,y,z) = S(x,y,z) \tag{1}$$

where $S(x,y,z)$ is the source function. The coordinate system in which we choose to solve this equation is the cartesian coordinate system. For the case of the Yukawa potential, the constant

$$k^2 = -\frac{1}{a^2} \tag{2}$$

which is proportional to the inverse square of its range. The source function is directly dependent on the nucleon density:

$$S(x,y,z) = 4\pi a V_0 \rho(x,y,z) \tag{3}$$

The Coulomb potential satisfies the Poisson equation so $k^2 = 0$, and its source function is

$$S(x,y,z) = 4\pi e^2 \rho_p(x,y,z) \tag{4}$$

Equation (1) can be rewritten to read

$$-\Big(\frac{\partial^2}{\partial x^2}+\frac{k^2}{3}\Big)\phi(x,y,z)=\Big(\frac{\partial^2}{\partial y^2}+\frac{\partial^2}{\partial z^2}+\frac{2k^2}{3}\Big)\phi(x,y,z)+S(x,y,z) \qquad (5)$$

The form of this equation suggests an iterative method of solving for ϕ, the potential function. If we call ϕ^m the potential at the m^{th} step of the iteration then it can be used to find $\phi^{m+1/3}$, the potential at a step further in the iteration. The iterative equation takes the form

$$-\Big(\frac{\partial^2}{\partial x^2}+\frac{k^2}{3}\Big)\phi^{m+1/3}(x,y,z)=\Big(\frac{\partial^2}{\partial y^2}+\frac{\partial^2}{\partial z^2}+\frac{2k^2}{3}\Big)\phi^{m}(x,y,z)+S(x,y,z) \qquad (6)$$

where the fractional superscript signifies iteration in one direction, namely the x direction. Similarly, we can write iterative equations in the y and z directions as follows:

$$-\Big(\frac{\partial^2}{\partial y^2}+\frac{k^2}{3}\Big)\phi^{m+2/3}(x,y,z)=\Big(\frac{\partial^2}{\partial x^2}+\frac{\partial^2}{\partial z^2}+\frac{2k^2}{3}\Big)\phi^{m+1/3}(x,y,z)+S(x,y,z) \qquad (7)$$

$$-\Big(\frac{\partial^2}{\partial z^2}+\frac{k^2}{3}\Big)\phi^{m+1}(x,y,z)=\Big(\frac{\partial^2}{\partial x^2}+\frac{\partial^2}{\partial y^2}+\frac{2k^2}{3}\Big)\phi^{m+2/3}(x,y,z)+S(x,y,z) \qquad (8)$$

To be consistent, eqns. (6), (7) and (8) must be solved simultaneously. We first guess ϕ^1 and specify the source function S to begin the iteration. At the m^{th} step, eqn. (6) allows $\phi^{m+1/3}$ to be evaluated. This function is then substituted into eqn. (7) to find $\phi^{m+2/3}$. Similarly, ϕ^{m+1} is obtained from known $\phi^{m+2/3}$ evaluated in eqn. (7). This procedure is repeated at each step in the iteration scheme until ϕ converges. In the following, we will show how any one of the eqns. (6), (7) and (8) is evaluated for the ϕ on the l.h.s. We call the ϕ to be evaluated ϕ^{m+1} and its preceeding step ϕ^m.

We now introduce three acceleration parameters R_x, R_y and R_z. These parameter will increase the rate of convergence of ϕ. In the i direction the iterative equation (can be either eqn. (6), (7) or (8)) reads

$$-\Big(\frac{\partial^2}{\partial x_i^2}+\frac{k^2}{3}+R_i\Big)\phi^{m+1}=\Big(\frac{\partial^2}{\partial x_j^2}+\frac{\partial^2}{\partial x_k^2}+\frac{2k^2}{3}-R_i\Big)\phi^m+S \qquad (9)$$

R_i's are to be appropriately chosen and the converged solution is independent of them. The iterative equation is solved on discretized space with even spacing in each direction. To facilitate writing our formulae, we introduce the symbol x_i^l to denote the coordinate in the i direction and at the l^{th} position of the grid space. The superscript l can take the values $\{1,2,....N_i-1,N_i\}$, where N_i is the maximum number of grid points in the i direction. The i-component Laplacian on the discretized space is

$$\frac{\partial^2}{\partial x_i^2}\phi^m(x_i^n)=\frac{1}{(\Delta x_i)^2}\Big[\phi^m(x_i^{n+1})-2\phi^m(x_i^n)+\phi^m(x_i^{n-1})\Big] \qquad (10)$$

where Δx_i is the size of the grid in the i direction. The coordinates of the other directions are kept fixed in this equation. The l.h.s. of eqn. (9) now reads

$$-\frac{1}{(\Delta x_i)^2}\Big[\phi^{m+1}(x_i^{n+1})+\alpha_i\phi^{m+1}(x_i^n)+\phi^{m+1}(x_i^{n-1})\Big] \qquad (11)$$

where we have set $\alpha_i=(\Delta x_i)^2(\frac{k^2}{3}+R_i)-2$. In the matrix notation this expression becomes

$$-\frac{1}{(\Delta x_i)^2}\begin{pmatrix}1\\ \alpha_i\\ 1\end{pmatrix}^T\begin{pmatrix}\phi^{m+1}(x_i^{n+1})\\ \phi^{m+1}(x_i^n)\\ \phi^{m+1}(x_i^{n-1})\end{pmatrix} \qquad (12)$$

where T stands for transpose operation on the matrix.

We labelled the r.h.s of eqn. (9) as

$$S^m(x_i^n)=\Big(\frac{\partial^2}{\partial x_j^2}+\frac{\partial^2}{\partial x_k^2}+\frac{2k^2}{3}-R_i\Big)\phi^m(x_i^n)+S(x_i^n) \qquad (13)$$

In this expression, functions ρ^m ans S^m are evaluated at x_i^n and the second derivatives are written as in eqn. (10). This equation has only ϕ dependent terms at the m^{th} step. Our final equation from eqns. (12) and (13) is

$$S^m(x_i^n) = -\frac{1}{(\Delta x_i)^2}\begin{pmatrix} 1 \\ \alpha_i \\ 1 \end{pmatrix}^T \begin{pmatrix} \phi^{m+1}(x_i^{n+1}) \\ \phi^{m+1}(x_i^n) \\ \phi^{m+1}(x_i^{n-1}) \end{pmatrix} \tag{14}$$

This is a three-point equation in ϕ^{m+1} at x_i^{n+1}, x_i^n and x_i^{n-1}.

The boundary condition of the potential ϕ determines S^m and ϕ^{m+1} at x_i^1 and $x_i^{N_i}$. Consider S^m at x_i^2 in eqn. (14). This value is related to ϕ^{m+1} at x_i^1, x_i^2 and x_i^3. Since $\phi^{m+1}(x_i^1)$ is known, $\phi^{m+1}(x_i^2)$ is proportional to $\phi^{m+1}(x_i^3)$. At the next grid point x_i^3, S^m is related to ϕ^{m+1} at x_i^2, x_i^3 and x_i^4. Since ϕ^{m+1} at x_i^2 and x_i^3 are already known to be proportional to each other from the previous step, ϕ^{m+1} at x_i^3 and x_i^4 are then also proportional to each other. This process can be continued until S^m at $x_i^{N_i-1}$. Thus the general relationship between the unknown functions (ϕ^{m+1}'s) of eqn. (14) can be written in terms of the two point recursion formula

$$\phi^{m+1}(x_i^{n+1}) = A(x_i^{n+1}) + B(x_i^{n+1})\phi^{m+1}(x_i^n) \tag{15}$$

Here, we have introduced two coefficient functions A and B. The problem has now been delegated to solving for these coefficients. Let us see how they are solved.

At the boundary points x_i^{bp} where matter density is assumed to vanish, $\rho(x_i^{bp}) = 0$, it is legitimate to make the following approximation

$$\phi^{m+1}(x_i^{bp}) = \phi^{m+1}(x_i^{bp} \pm \Delta x_i) \tag{16}$$

(the + sign is used when $x_i^{bp} = x_i^1$ and − sign when $x_i^{bp} = x_i^{N_i}$) This means the potential varies slowly at the boundary. For the short range Yukawa potential this

approximation is quite adequate. In the case of the long range Coulomb potential the boundary has to be chosen sufficiently far from the charge distribution. Equation (16) enables us to find A and B at the boundary points; $A(x_i^{bp}) = 0$ and $B(x_i^{bp}) = 1$. To find A and B at other points we need to find recursion formulae for them.

We insert recursion formula for ϕ^{m+1} in eqn. (15) into eqn. (14) to get

$$\left[B(x_i^{n+1}) + \alpha_i\right]\phi^{m+1}(x_i^n) = -(\Delta x_i)^2 S^m(x_i^n) - A(x_i^{n+1}) - \phi^{m+1}(x_i^{n-1}) \qquad (17)$$

which we can write as

$$\phi^{m+1}(x_i^n) = \tilde{A}(x_i^n) + \tilde{B}(x_i^n)\phi^{m+1}(x_i^{n-1}) \qquad (18)$$

with the coefficients given by

$$\tilde{A}(x_i^n) = -\frac{A(x_i^{n+1}) + (\Delta x_i)^2 S^m(x_i^n)}{\alpha_i + B(x_i^{n+1})} \qquad (19)$$

$$\tilde{B}(x_i^n) = \frac{-1}{\alpha_i + B(x_i^{n+1})} \qquad (20)$$

Upon comparing eqn. (18) to eqn. 15 we find the $\tilde{A}$ and $\tilde{B}$ coefficient functions above to be A and B respectively. Given their values at the boundary points, recursion formulae (19) and (20) determine their values elsewhere inside the boundary. Having found these coefficients, $\phi^{m+1}(x_i^{n+1})$ is obtained through relation (15). This calculation must be repeated for j and k components as remarked previously.

References

[AB 85] J. Aichelin and G.F. Bertsch, Phys. Rev. **C31**, 1730 (1985).

[AG 88] S. Ayik and C. Grégoire, Phys. Lett. **212**, 269 (1988).

[AH 84] J. Aichelin and J. Hüfner, Phys. Lett. **136B**, 15 (1984).

[Aic 88] J.A. Aichelin, G. Peilert, A. Bohnet, A. Rosenhauer, H. Stöcker, and Greiner, Phys. Rev. **C37**, 2451 (1988).

[Bau 86] W. Bauer, W Cassing, U. Mosel, M Tohyama and R. Cusson, Phys. Rev. **C34**, 2127 (1986). W. Bauer, G.F. Bertsch, W. Cassing and U. Mosel Phys. Rev. **C34**, 35 (1986).

[BBD 87] W. Bauer, G.F. Bertsch and S. Das Gupta, Phys. Rev. Lett. **58**, 863 (1987). G.F. Bertsch, Michigan State University Cyclotron Laboratory preprint, MSUCL-544 (1985).

[BCK 85] E. Baron, S. Cooperstein and Kahana, Nucl. Phys. **A440**, 744 (1985).

[BDD 86] D.M. Brink, A. Dellafiore and M. Di Toro, Nucl. Phys. **A457**, 205 (1986).

[BDa 88] G.F. Bertsch and S. Das Gupta, Phys. Rep. **160**, 191 (1988).

[BDi 88] G.F. Burgio and M. Di Toro, Nucl. Phys. **A476**, 189 (1988).

[Ber 80] G.F. Bertsch, Prog. in Part. and Nucl. Phys., Vol **4**, 483 (1980).

[Ber 81] G.F. Bertsch, Phys. Rev. Lett. **46**, 472 (1981).

[Ber 85] G.F. Bertsch, Frontiers of Nuclear Dynamics, eds. R. Broglia and C.H. Dasso, 277 (1985), Plenum Press.

[Biz 86] G. Bizard et al., Phys. Lett. **172B**, 301 (1986).

[BKD 84] G.F. Bertsch, H. Kruse and S. Das Gupta, Phys. Rev. **C29**, 673 (1984).

[BKN 76] P. Bonche, S.E. Koonin and J.W. Negele, Phys. Rev. **C13**, 1226 (1976).

[Bla 80] J.P. Blazoit, Phys. Rep. **64**, 171 (1980).

[Blä 88] B. Blätell, V. Koch, W. Cassing and U. Mosel, Phys. Rev. **C38**, 1767 (1988).

[BM 86] W. Botermans and R. Malfliet, Phys. Lett. **171B**, 22 (1986).

[BM 75] A. Bohr and B.R. Mottelson, **Nuclear Structure**, Vol. 2, (Massachusets, 1975), Benjamin .

[BS 83] G.F. Bertsch and P.J. Siemens, Phys. Lett. **126B**, 9 (1983).

[CDL 84] X. Campi, J. Desbois and E. Lipparini, Phys. Lett. **142B**, 8 (1984).

[CLG 87] J. Cugnon, A. Lejeune and P. Grangé, Phys. Rev. **C35**, 861 (1987).

[CMV 81] J. Cugnon, T. Mizutani and J. Vandermeulen, Nucl. Phys. **A352** 505 (1981).

[Coo 88] E.D. Cooper, private communication.

[Dan 88] P. Danielewicz et al., Phys. Rev. **C38**, 120 (1988).

[Dav 85] K.T.R. Davies, K.R.S. Devi, S.E. Koonin and M.R. Strayer, **Treatise on Heavy Ion Science**, Vol. 3, Ed. D.A. Bromley, 1 (1985).

[Day 86] R. Dayras et al., Nucl. Phys. **A460**, 299 (1986).

[Day 89] R. Dayras et al., Phys. Rev. Lett. **62**, 1017 (1986).

[DM 81] S. Das Gupta and A.Z. Mekjian, Phys. Rep. **72**, 131 (1981).

[DO 85] P. Danielewicz and G. Odyniec, Phys. Lett., **157B**, 146 (1985).

[Ege 86] Ch. Egelhaaf, G. Bohlen, H. Fuchs, A. Gamp, H. Homeyer and H. Kluge, Phys. Rev. Lett. **46**, 813 (1986).

[FH 73] H. Feshbach and K. Huang, Phys. Lett. **47B**, 300 (1973).

[Fis 67] M.E. Fisher, Physica (N.Y.) **3**, 255 (1967).

[FL 83] W.A. Friedman and W.G. Lynch, Phys. Rev. **C28**, 950 (1983).

[FP 81] B. Friedman and V.R. Pandharipande, Nucl. Phys. **A361**, 502 (1981)

[FR 83] G. Fai and J. Randrup, Nucl. Phys. **A404**, 551 (1983).

[FR 82] G. Fai and J. Randrup, Nucl. Phys. **A381**, 557 (1982).

[FW 71] A.L. Fetter and J.D. Walecka, **Quantum Theory of Many Particle. Systems**. (New York, 1971) McGraw Hill.

[Gal 87] C. Gale, Phys. Rev. **C36**, 2152 (1987). C. Gale, Ph.D. thesis, McGill University, (1986) unpublished.

[Gal 88] J. Gallego, private communication (1988).

[GB 87] C.K. Gelbke and D.H. Boal, Prog. in Part. and Nucl. Phys., **19**, Ed. A. Faessler (1987).

[GBD 87] C. Gale, G.F. Bertsch and S. Das Gupta, Phys. Rev. **C35**, 1666 (1987).

[GD 85] C. Gale and S. Das Gupta, Phys. Lett. **162B**, 35 (1985).

[Gel 77] C.K. Gelbke et al., Phys. Lett. **70B**, 415 (1977).

[GKM 84] L. Goodman, J.I. Kapusta and A.Z. Mekjian, Phys. Rev. **C30**, 851 (1984).

[Gol 74] A.S. Goldhaber, Phys. Lett. **53B**, 306 (1974).

[Gol 81] H. Goldstein, **Classical Mechanics**, second edition. 1981, p. 95

[Gré 87] C. Grégoire, B. Remaud, F. Sebille and L. Vinet, Phys. Lett.

186, 14 (1987). C. Grégoire, B. Remaud, F. Sebille, L. Vinet and Y. Raffray, Nucl. Phys. **A465**, 317 (1987) .

[Gre 75] D.E. Greiner, P.J. Lindstrom and H.H. Heckman, B. Cock and F.S. Biesser, Phys. Rev. Lett. **35**, 152 (1975).

[Gro 84] D.H.E. Gross, Nucl. Phys. **A428**, 313c (1984).

[GS 81] K. Goeke and J. Speth, Ann. Rev. Nucl. and Part. Sci., **32**, 65 (1981).

[Gus 84] H.A. Gustafasson et al., Phys. Rev. Lett. **52**, 1590 (1984).

[Gue 83] C. Guet, Nucl. Phys. **A400**, 191c (1983).

[Heu 87] B. Heusch, Frontiers of Heavy-ion Physics: Proceedings of the 6th Ariatic Intern. Conf. on Nuclear Physics, Eds. N. Cindro, W. Greiner and R. Čaplar, (Singopore. 1987), World Scientific .

[Hir 84] S. Hirch et al., Phys. Rev. **C29**, 508 (1984).

[Hüf 85] J. Hüfner, Phys. Rep. **125**, 129 (1985).

[Jac 87] B.V. Jacak et al., Phys. Rev. **C35**, 1751 (1987).

[JJ 80] B.K. Jennings and A.D. Jackson, Phys. Rep. **66**, 141 (1980).

[JMZ 83] H. Jaqaman, A.Z. Mekjian and L. Zamick, Phys. Rev. **C27** 2728 (1983).

[KB 62] L.P. Kanadoff and G. Baym, **Quantum Statistical Mechanics**, (1962) Benjamin.

[KJS 85] H. Kruse, B.V. Jacak and H. Stöcker, Phys. Rev. Lett. **54**, 289 (1985).

[KK 68] K. Kikuchi and M. Kawai, **Nuclear Matter and Nuclear Reactions**

(North-Holand, Ansterdam, 1968) chpt. 2.

[KLM 87] C.M. Ko, Q. Li and R. Wang, Phys. Rev. Lett. **59**, 1084 (1987).

[Koo 86] S.E. Koonin, Proceedings of the Second Intern. Conf. on Local Eqiulibrium in Strong Interaction Physics, Eds. P. Carruthers and D. Strottman, (Singapore, 1986) World Scientific.

[KS 84] J. Knoll and B. Strack, Phys. Lett. **149B**, 45 (1984).

[KSS 86] H. Kohl, P. Schuck and Stringari, Nucl. Phys. **A459**, 265 (1986).

[KW 88] J. Knoll and J. Wu, Nucl. Phys. **A481**, 173 (1988).

[Kya 86] A. Kyanowski et al., Phys. Lett. **181B**, 43 (1986).

[LC 88] S.J. Lee and E.D. Cooper, private communication.

[Lee 76] T.D. Lee, Rev. Mod. Phys. **47**, 267 (1976).

[Lej 86] A. Lejeune, P. Grangé and M. Martzolff and J. Cugnon, Nucl. Phys. **A453**, 189 (1986).

[Len 88] R. Lenk, private communication (1988).

[LP 86] R.J. Lenk and V.R. Pandharipande, Phys. Rev. **C34**, 177 (1986).

[LP 81] E.M. Lifshitz and L.P. Pitaevskii, **Physical Kinetics**. Pergamon Press (1981).

[Mas 84] C. Maso, Ph.D. thesis, McGill University (1984), unpublished.

[MB 82] G.P. Maddison and D.M. Brink, Nucl. Phys. **A378**, 566 (1982).

[Mig 78] A.B. Migdal, Rev. Mod. Phys. **50**, 107 (1978).

[Mye 78] W.D. Myers, Nucl. Phys. **A296**, 177 (1978).

[Neg 82] J.W. Negele, Rev. Mod. Phys. **54**, 913 (1982).

[Nor 28] L.W. Nordheim, Proc. Roy. Soc. **A119**, 689 (1928).

[Per 74] M. Perl, **High Energy Hadron Physics**, (New York, 1974) Wiley.

[PN 66] D. Pines and P. Nozieres, **The Theory of Quantum Liquids**, Vol 1, p. 30 (New York, 1966), W.A. Benjamin.

[PR 87] C.J. Pethick and D.G. Ravenhall, Nucl. Phys. **A471**, 19c (1987).

[RDH 80] B. Remaud, C. Dorso and E.S. Hernandez, Physica **112A**,192 (1980)

[Rei 84] L.E. Reichl, **A Modern Course in Statistical Physics**, (Austin, 1984) Uinversity of Texas Press.

[Rém 86] B. Rémaud, C. Grégoire, F. Sebille and L. Vinet, Phys. Lett. **180B**, 198 (1986).

[RS 80] P. Ring and P. Schuck, **The Nuclear Many-Body Problem**, (New York, 1980), Springer-Verlag.

[Rud 86] G. Rudolf et al., Phys. Rev. Lett. **57**, 2905 (1986).

[Sco 80] D. Scott, Prog. in Part. and Nucl. Phys., Vol. 4, 5 (1980).

[SF 74] Amos de Shalit and H. Feshbach, **Theoretical Nuclear Physics**, Vol. 1. John Wiley and Sons. (1974).

[SP 87] T.J. Schlagel and V.R. Pandharipande, Phys. Rev. **C36**, 162 (1987).

[Ste 87] G.S.F. Stephens, RV.F. Janssens, D.G. Konar and B.D. Wilkins, Phys. Rev. **C35**, 64 (1987).

[Sto 86] R. Stock, Phys. Rep. **135**, 259 (1986).

[Tho 61] D.J. Thouless, **The Quantum Mechanics of Many-Body Systems**, Academic Press (1961).

[SW 86] B.D. Serot and J.D. Welecka, **The Relativistic Nuclear Many-Body Problem**, in Advances in Nuclear Physics, Vol **16**, (New York, 1986),

Plenum Press.

[TS 86] H.H.K. Tang and P.J. Siemens, Nucl. Phys. **A453**, 251 (1986).

[TW 80] H.H.K. Tang and C.Y. Wong, Phys. Rev. **C21**, 1846 (1980).

[Van 79] K. Van Bibber et al., Phys. Rev. Lett. **43**, 840 (1979).

[VB 72] D. Vautherin and D.M. Brink, Phys. Rev. **C5**, 626 (1972).

[VJP 85] A. Vicentini, G. Jacucci and V.R. Pandharipande, Phys. Rev. **C31**, 1783 (1985).

[Won 82] C.Y. Wong, Phys. Rev. **C25** 1460 (1982).

[YY 87] B.J. Yang and S.G. Yao, Phys. Rev. **C36**, 667 (1987).

Figure Captions: Chapter 2

Fig. 2.1 The model self-consistent density (full line) derived from the density-dependent interaction is compared to the evolved density distributions (dashed line) at various times.

Fig. 2.2 Same as in Fig. 2.1 but for ^{20}Ne nucleus.

Fig. 2.3 Same as in Fig. 2.1 but for ^{4}He nucleus.

Fig. 2.4 The time-dependent rms radii of the ground state nuclei in the Vlasov dynamics.

Fig. 2.5 Same as in Fig. 2.4 but for the rms momenta.

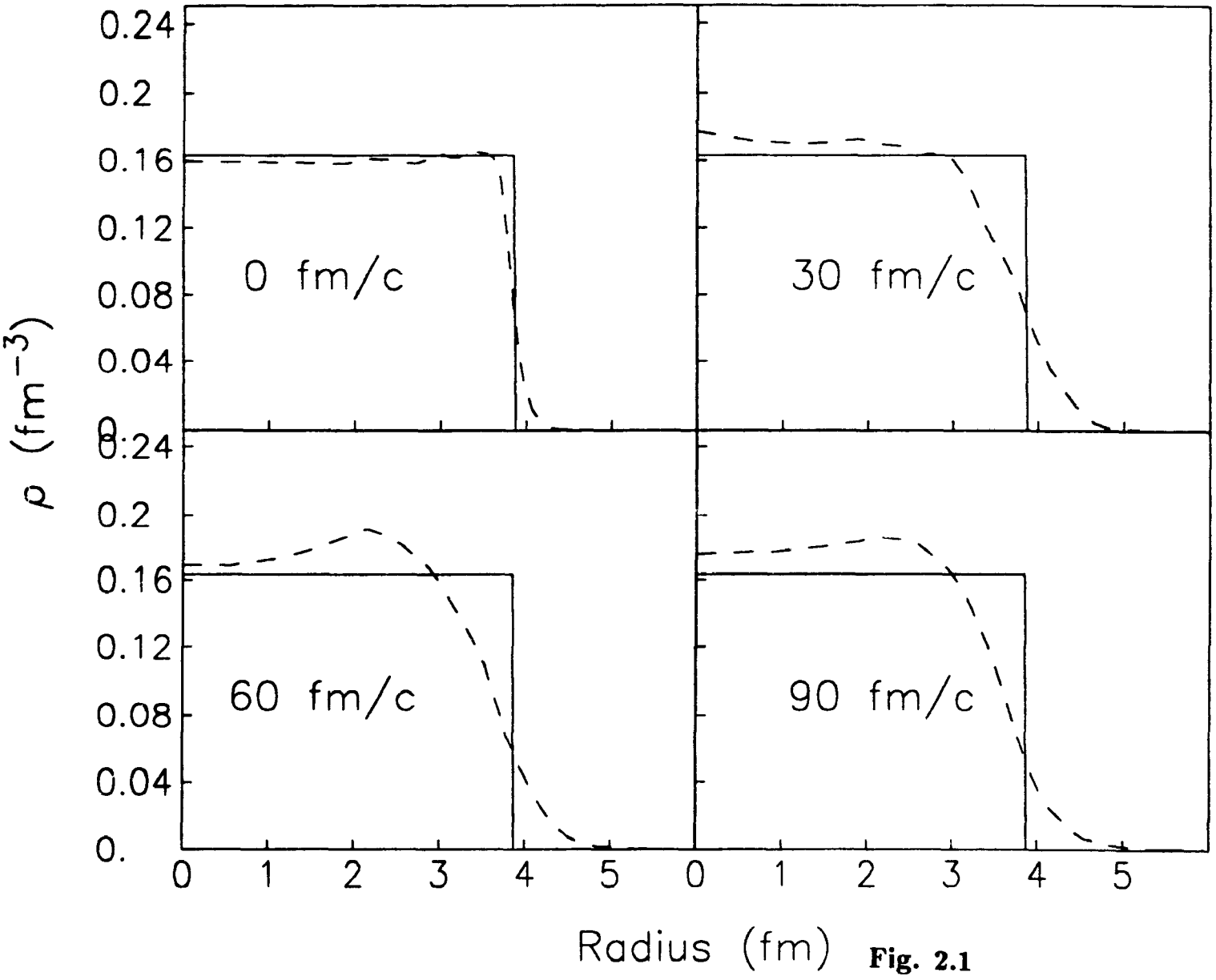
0.24
0.2
0.16
0.12
0.08
0.04
0
ρ (fm⁻³)
0 fm/c
30 fm/c
60 fm/c
90 fm/c
0 1 2 3 4 5
Radius (fm)

Fig. 2.1

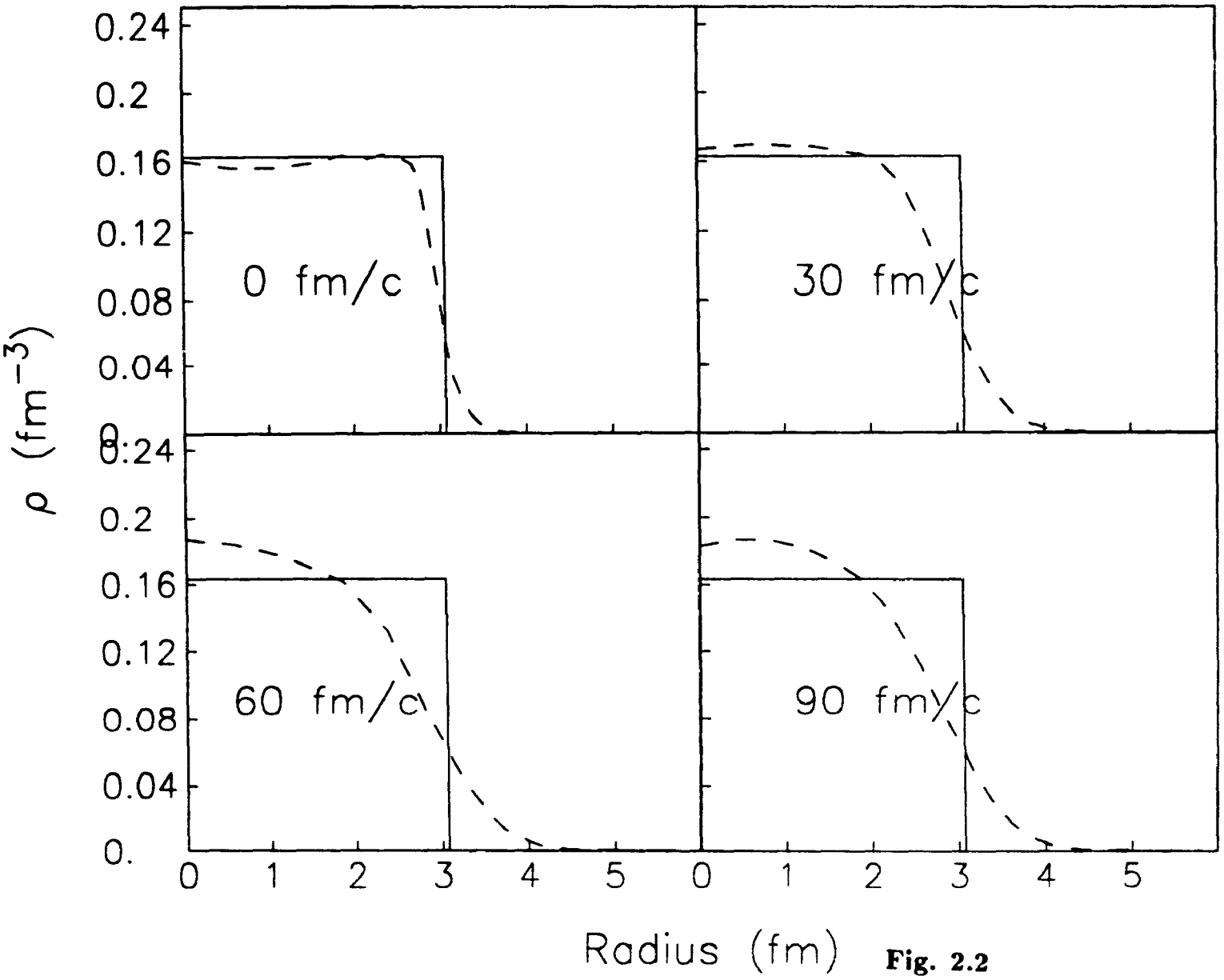
0.24
0.2
0.16
0.12
0.08
0.04
0
0 fm/c
30 fm/c
60 fm/c
90 fm/c
ρ (fm⁻³)
0 1 2 3 4 5
Radius (fm)

Fig. 2.2

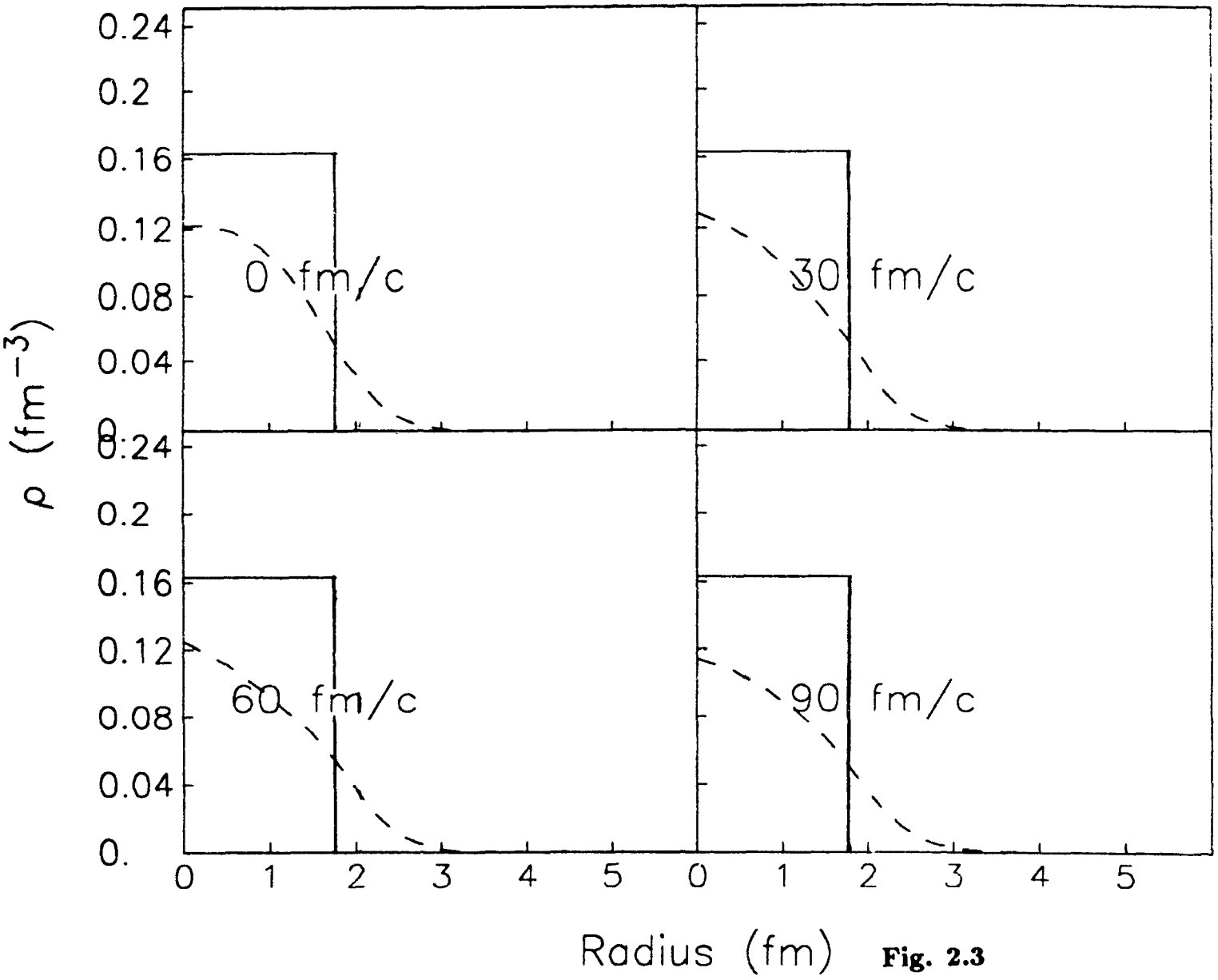
0.24
0.2
0.16
0.12
0.08
0.04
0
0 fm/c
30 fm/c
60 fm/c
90 fm/c
ρ (fm⁻³)
0 1 2 3 4 5
Radius (fm)

Fig. 2.3

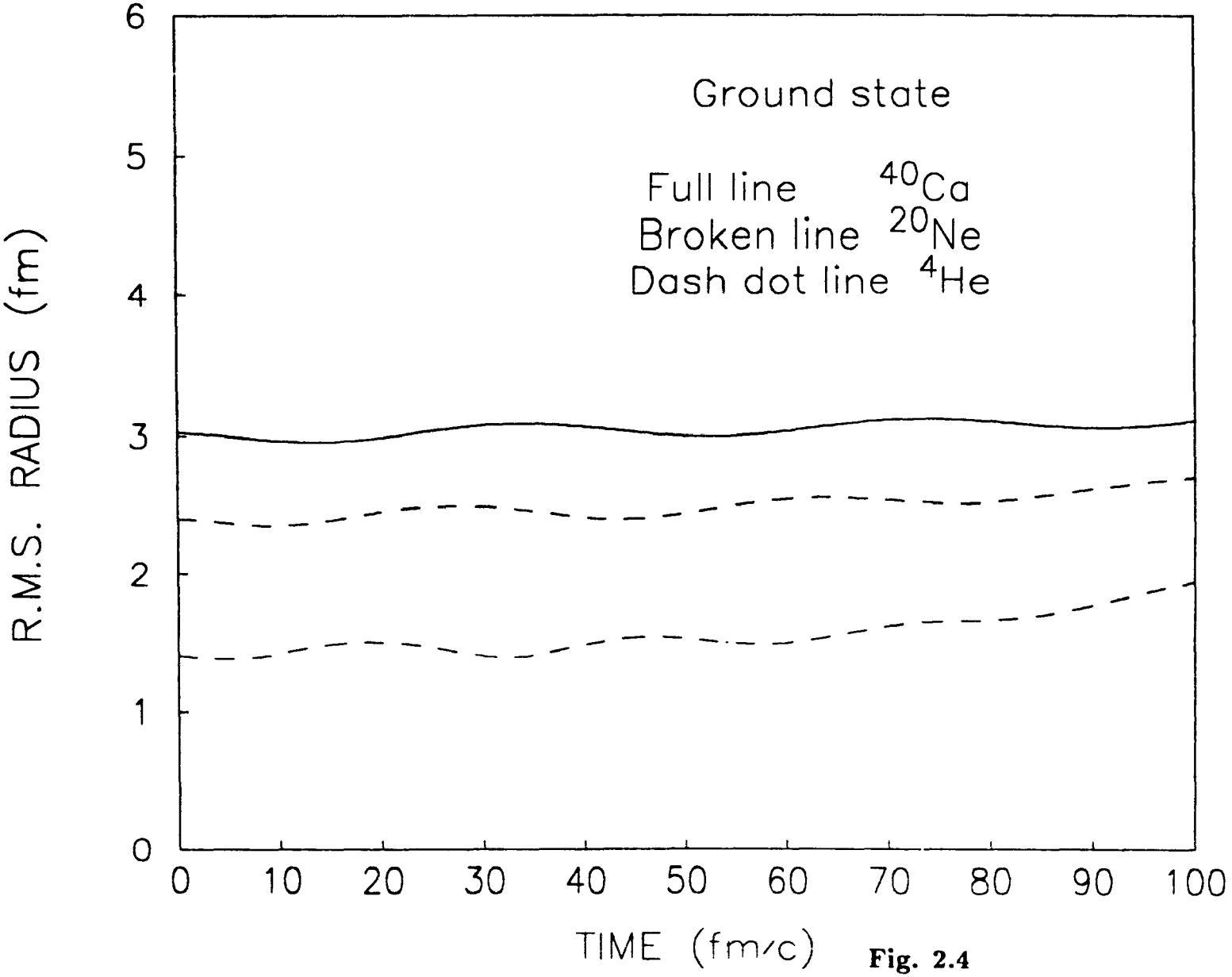
Ground state
Full line ^{40}Ca
Broken line ^{20}Ne
Dash dot line ^{4}He
R.M.S. RADIUS (fm)
TIME (fm/c)
0
1
2
3
4
5
6
0
10
20
30
40
50
60
70
80
90
100

Fig. 2.4

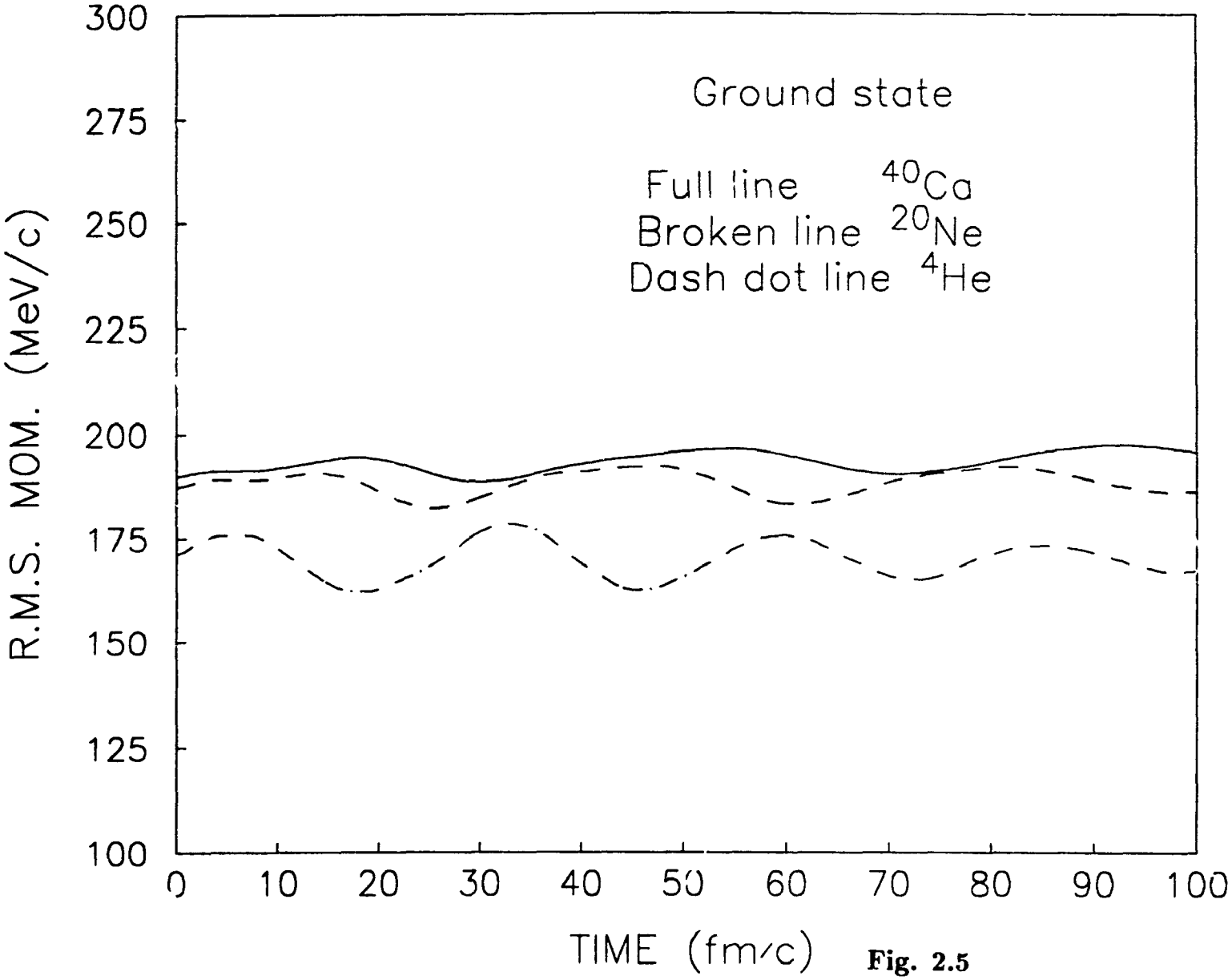
Ground state
Full line ^{40}Ca
Broken line ^{20}Ne
Dash dot line ^{4}He
R.M.S. MOM. (MeV/c)
TIME (fm/c)
300
275
250
225
200
175
150
125
100
0
10
20
30
40
50
60
70
80
90
100

Fig. 2.5

Table 3.1a The intrinsic width σ_0 in X, Y and Z directions obtained from the BUU simulations are displayed. The results are for the reaction $^{20}Ne +^{20} Ne$ at different beam energies without Coulomb potential. The impact parameter in all cases is $4.31fm$ and with a total of 42 events.

Table 3.1b Same as in Table 3.1a but for components of the averaged momentum per nucleon.

Table 3.1a

$b = 4.31fm$

	E_{lab}/A (MeV)	σ_{0X} (MeV/c)	σ_{0Y} (MeV/c)	σ_{0Z} (MeV/c)
No Coulomb	50	65.6	53.1	49.1
No Coulomb	100	70.3	75.1	68.2

Table 3.1b

$b = 4.31fm$

	E_{lab}/A (MeV)	$\langle P_{XK}/K \rangle$ (MeV/c)	$\langle P_{YK}/K \rangle$ (MeV/c)	$\langle P_{ZK}/K \rangle$ (MeV/c)
No Coulomb	50	−51.1	−2.0	−53.1
No Coulomb	100	−29.4	1.3	−33.0

Figure Captions: Chapter 3

Fig. 3.1 Histogram shows the mass distribution of fragments from ^{20}Ne+^{20}Ne at $E_{lab}/A = 100MeV$ with a fixed impact parameter $b = 4.31fm$. The total number of events in this histogram is 42.

Fig. 3.2 The momentum distribution in the Z-component of the projectile-like fragments is shown here. These events (or fragments) are the same as those shown in Fig. 3.1

Fig. 3.3 The yield function $d^2\sigma/dEd\Omega$ of the projectile-like fragments according to the Gaussian conjecture is plotted at various angles. The incident energy of the ^{20}Ne projectile is $E_{lab}/A = 100MeV$. Parameters $\sigma_0, \langle P_{\perp K}/K\rangle$ and $\langle P_{ZK}/K\rangle$ of the Gaussian distributions are obtained from the BUU calculations as displayed in Table 3.1a and 3.1b. The mass number K = 15. The graphs are all normalized to unity at their peaks.

Fig. 3.4 Angular distribution of the projectile-like fragments with (b) and without (a) the inclusion of the Coulomb potential. The smooth curves are derived from the Gaussian conjecture where its parameters are determined from the BUU calculations. Events in the histogram are from the BUU calculation of ^{20}Ne + ^{20}Ne at $E_{lab}/A = 100MeV$. The mass number K = 15.

Fig. 3.5 The mass distributions of $^{40}Ca + ^{40}Ca$ at $92MeV/A$ are displayed. These results come from 30 runs spanning the impact parameter b from 0 to 4.2 fm. The upper histogram displays the mass distribution of all fragments and in the lower histogram the contributions from the spectators (dashed line) and the participants (full line) are separated. In the latter histogram a cut in the momentum of the fragments in the CM of the colliding ions is imposed for this distinction.

Fig. 3.6 Same as in Fig. 3.5 but for a lower beam energy, $E_{lab}/A = 72MeV$.

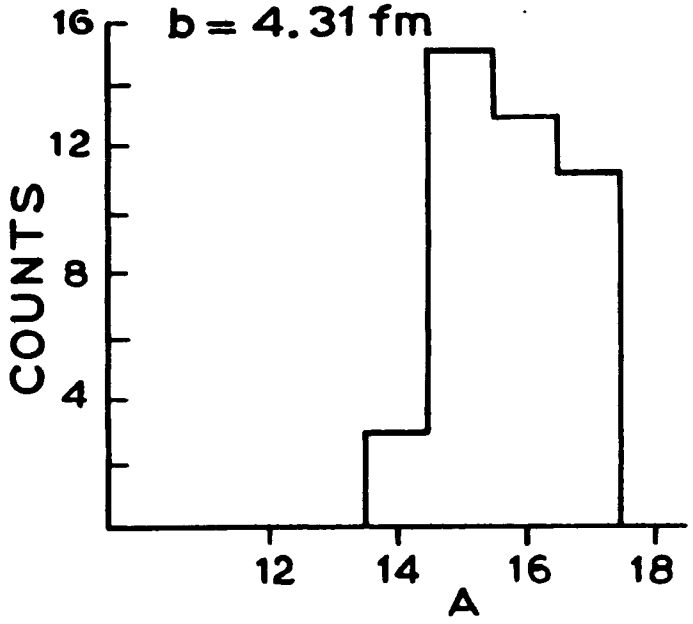

Fig. 3.1

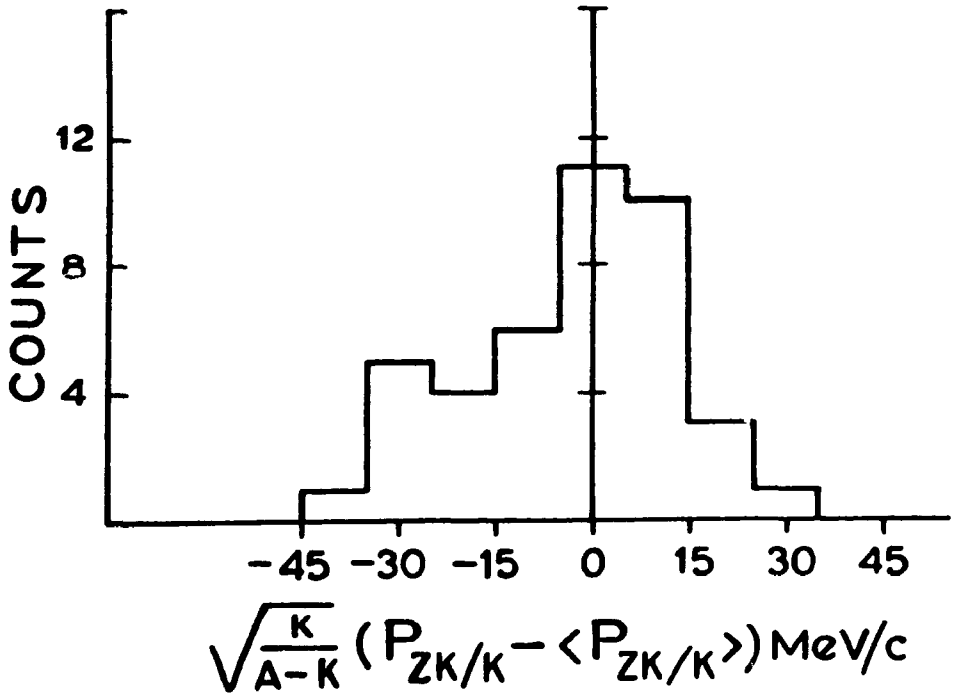
COUNTS
12
8
4
-45
-30
-15
0
15
30
45
$\sqrt{\frac{K}{A-K}}(P_{ZK/K} - \langle P_{ZK/K} \rangle)$ MeV/c

Fig. 3.2

Fig. 3.3

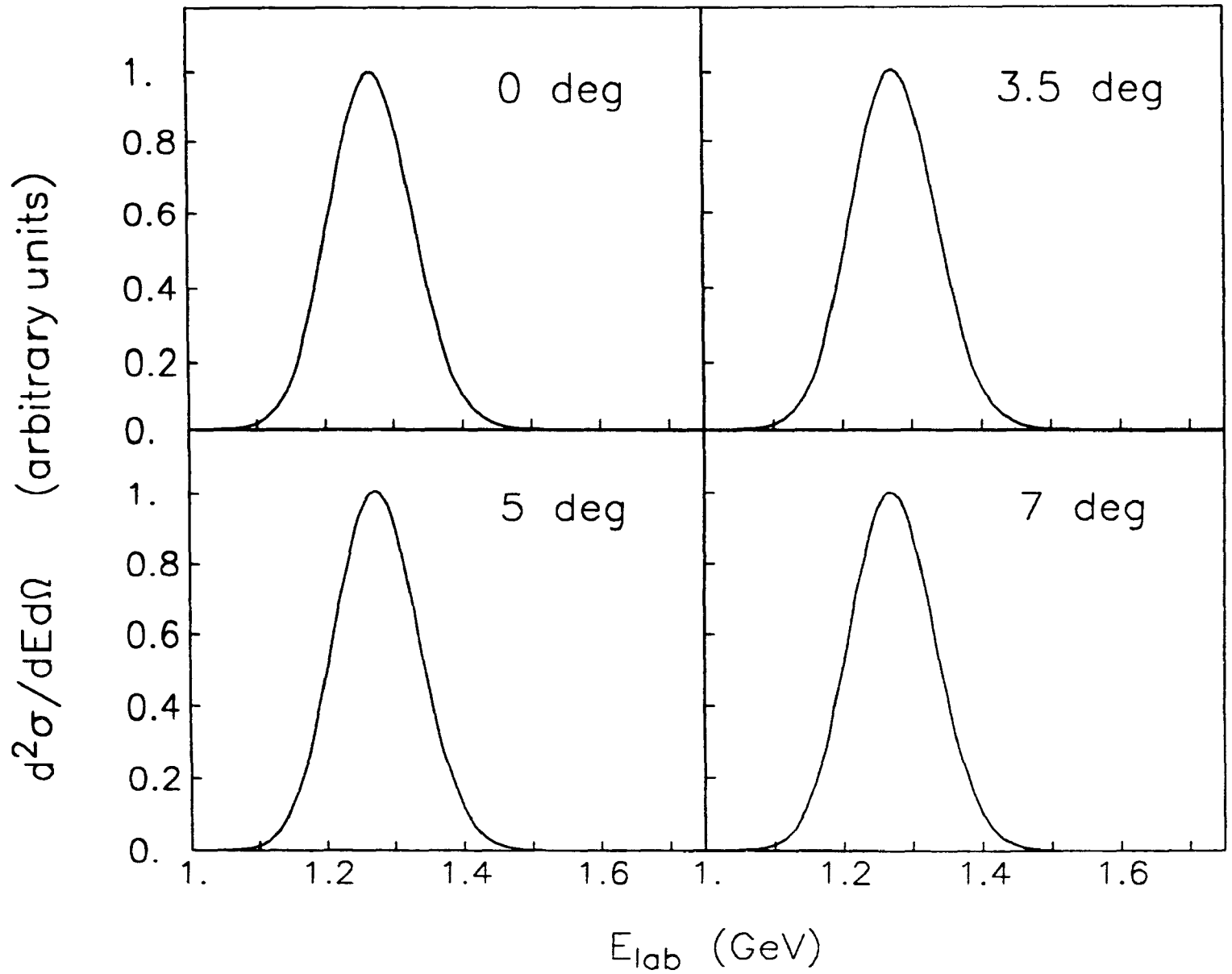
0 deg
3.5 deg
5 deg
7 deg
1.
0.8
0.6
0.4
0.2
0.
1.2
1.4
1.6
$d^2\sigma/dEd\Omega$ (arbitrary units)
E_{lab} (GeV)

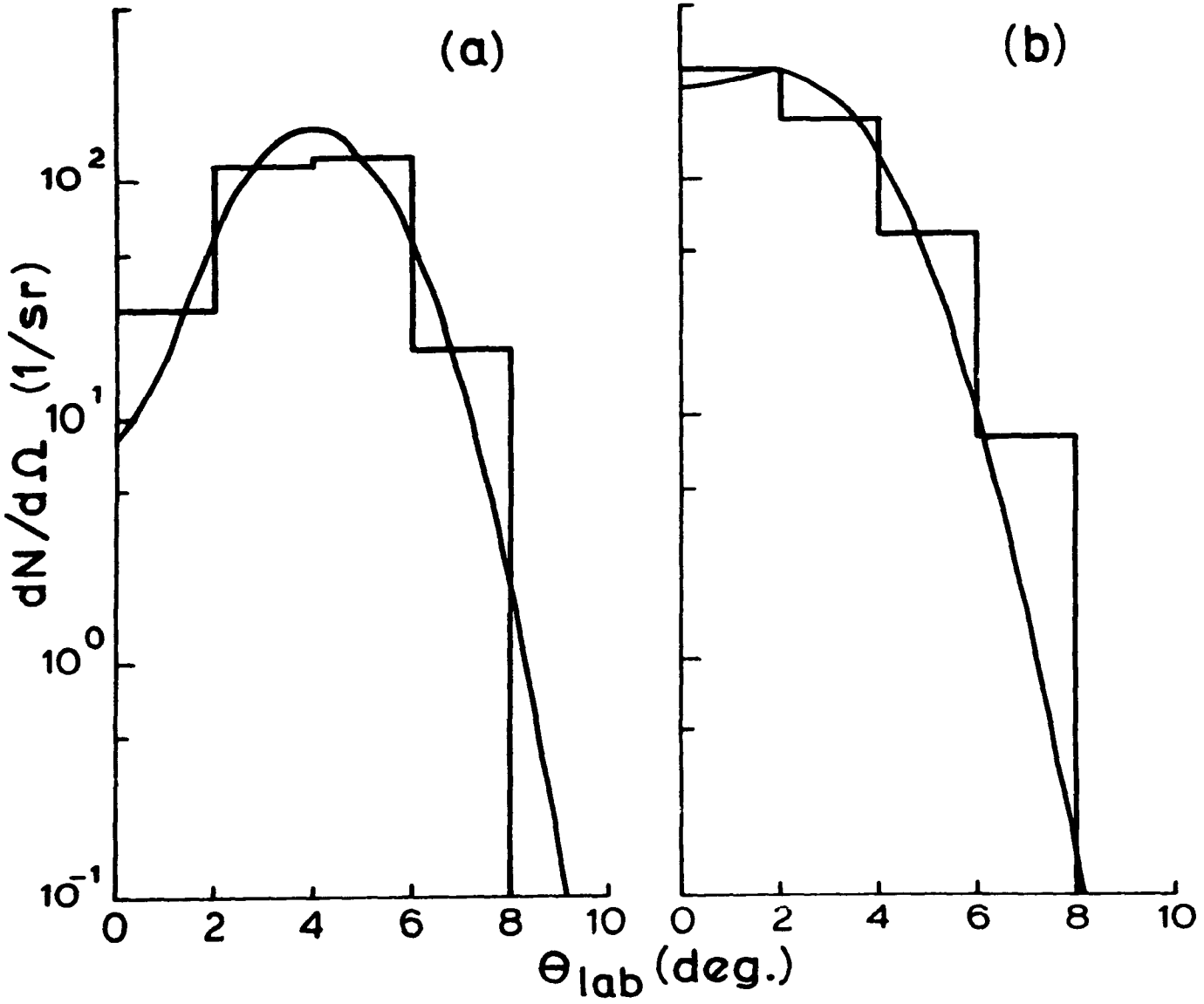

Fig. 3.4

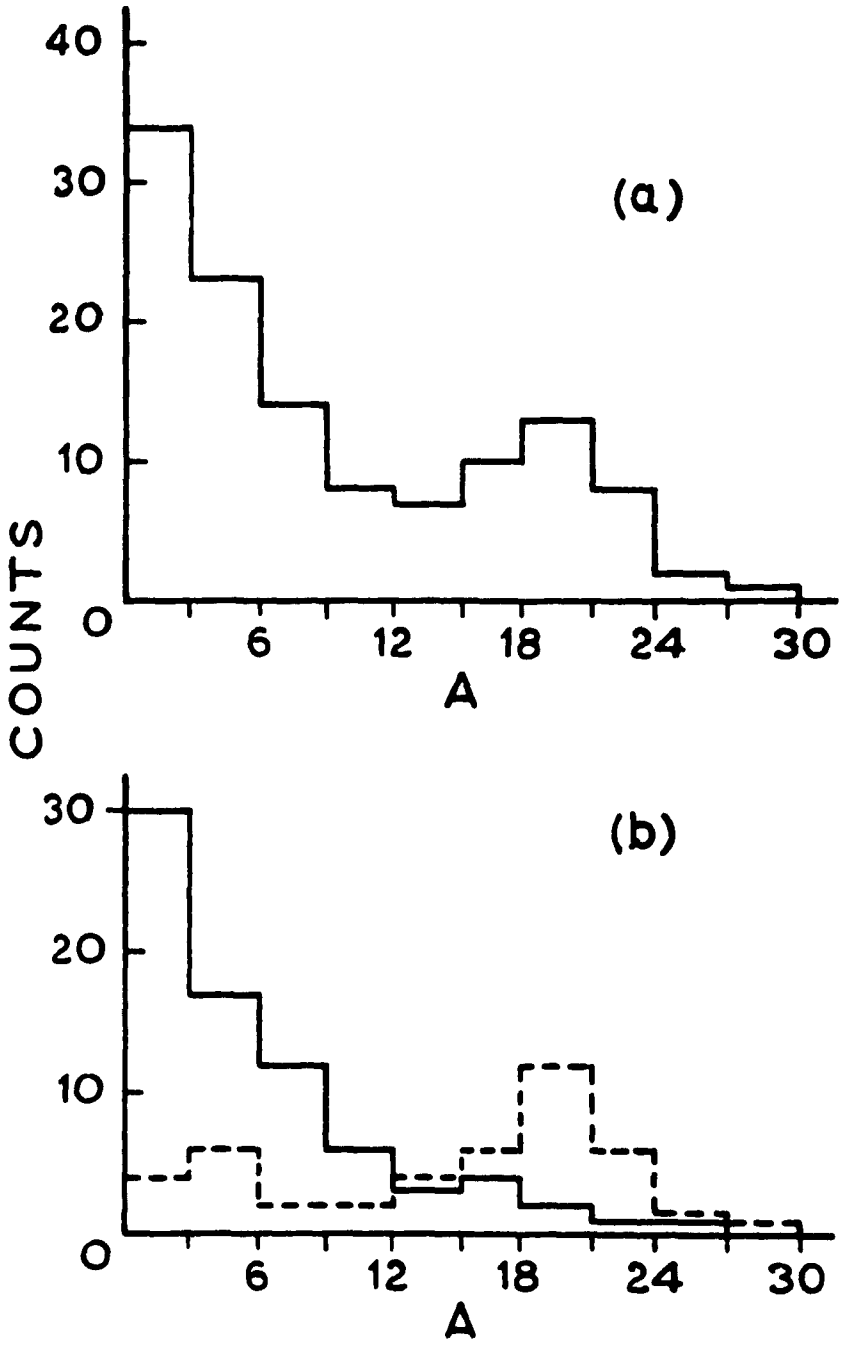

Fig. 3.5

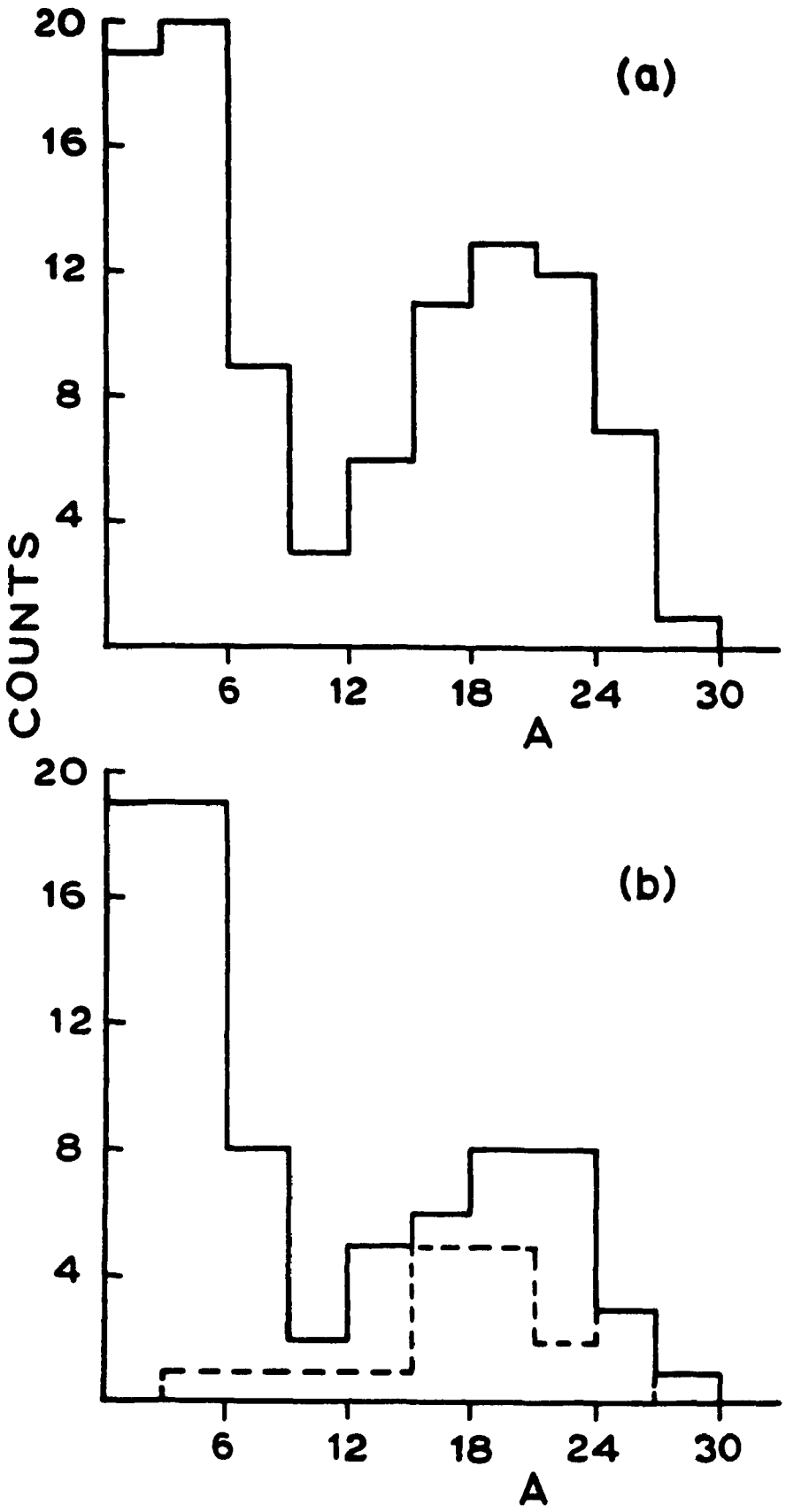

Fig. 3.6

Table 4.1 This table summarizes six sets of parameters used to generate self-consistent densities. The stiff potentials are those with $\sigma = 2$ and the soft potentials with $\sigma = 7/6$. These potentials are given names as appear in the first row. The total number of parameters in each set is five but not all of them are independent. The combination $(A + 4\pi a^3 V_0)$ is always fixed but with different values between soft and stiff potentials; and similarly for the B parameter.

Table 4.2 The parameter sets exhibited in Table 4.1, except for the BKN, were used to evaluate the binding energies of nuclei and the results are displayed in this table. These calculations were done with the inclusion of Coulomb potential. The experimental binding energies are also shown here for comparison.

Table 4.1

	BKN	STIFF1	STIFF2	SOFT1	SOFT2	SOFT3
σ	2	2	2	7/6	7/6	7/6
A($MeV\,fm^3$)	−373.30	0.00	−300.00	−1936.80	−1563.60	−1428.20
B($MeV\,fm^{3\sigma}$)	3238.10	3238.10	3238.10	2805.30	2805.30	2805.30
$a(fm)$	0.45979	0.45979	0.45979	0.800	0.45979	0.45979
$V_0(MeV)$	−363.00	−668.65	80.50	−363.04	−668.65	−779.48

Table 4.2

$-E/A(MeV)$

	STIFF1	STIFF2	SOFT1	SOFT2	SOFT3	Expt.
^4He	4.43	3.04	6.25	6.02	5.63	7.07
^{16}O	7.25	5.62	9.80	8.43	7.89	7.98
^{40}Ca	8.22	6.76	10.78	9.08	8.65	8.55

Figure Captions: Chapter 4

Fig. 4.1 Self-consistent density distributions (solid line) with the stiff potential ($\sigma = 2$) are compared to the Myers' distributions (dashed line). The first column is with the BKN parameters, second column with the STIFF2, and the last column with the STIFF1. In all cases the Coulomb potential was included in the self-consistent calculation.

Fig. 4.2 The self-consistent proton (dash-doted line) and neutron (dashed line) densities of the STIFF1 potential for three nuclei are shown. Total density is shown in full line.

Fig. 4.3 The self-consistent proton (dashed line) and neutron (full line) potentials for three nuclei are shown. Parameter set STIFF1 was used in this calculation.

Fig. 4.4 Same as in Fig. 4.1 but for soft potentials. Results in coulmn one, two and three were calculated using SOFT1, SOFT2 and SOFT3 potentials respectively.

Fig. 4.5 The self-consistent density of the STIFF1 potential with Coulomb interaction (solid line) is compared to its density already evolved by the Vlasov equation. The quality of the evolved density is shown at various times.

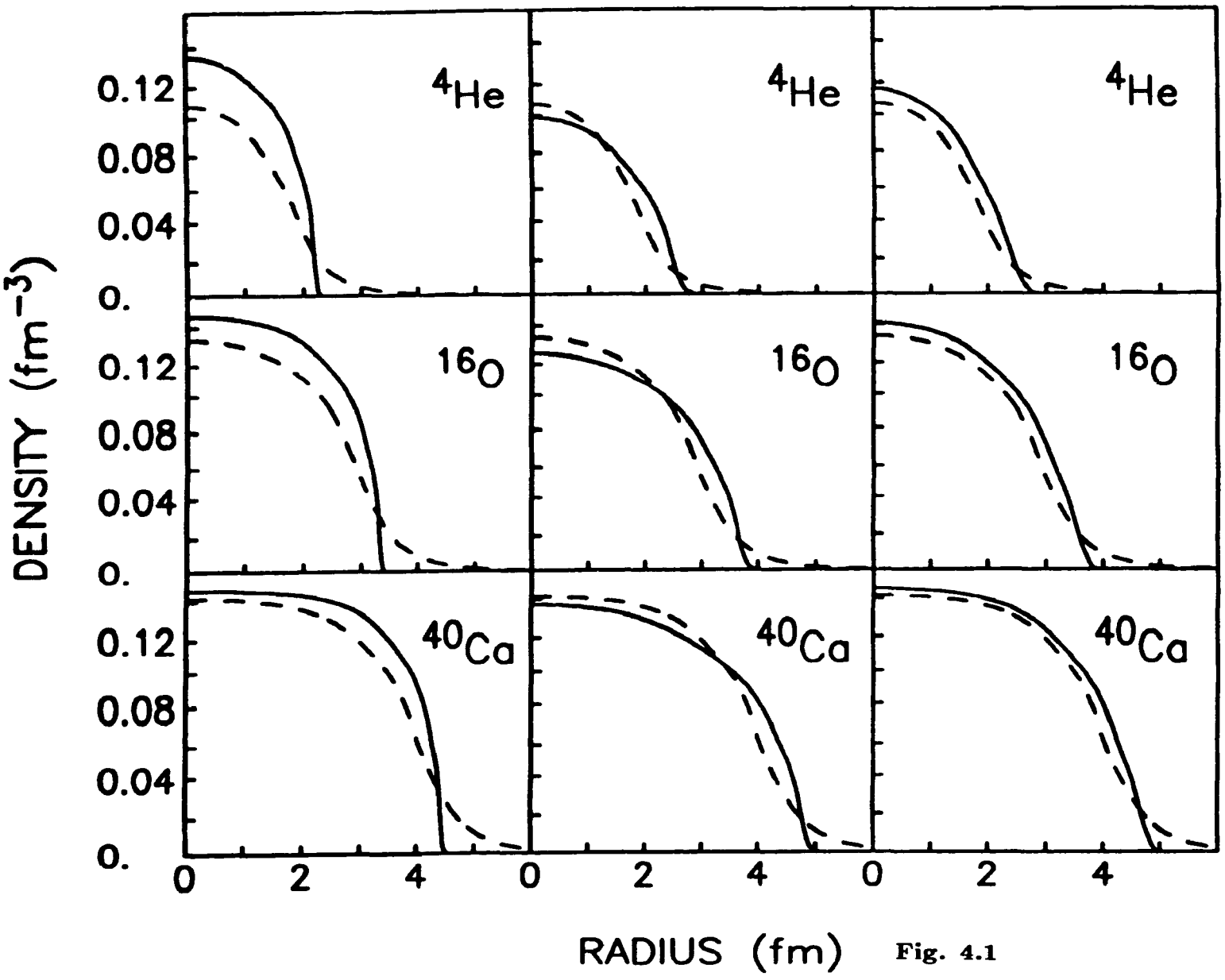

Fig. 4.1

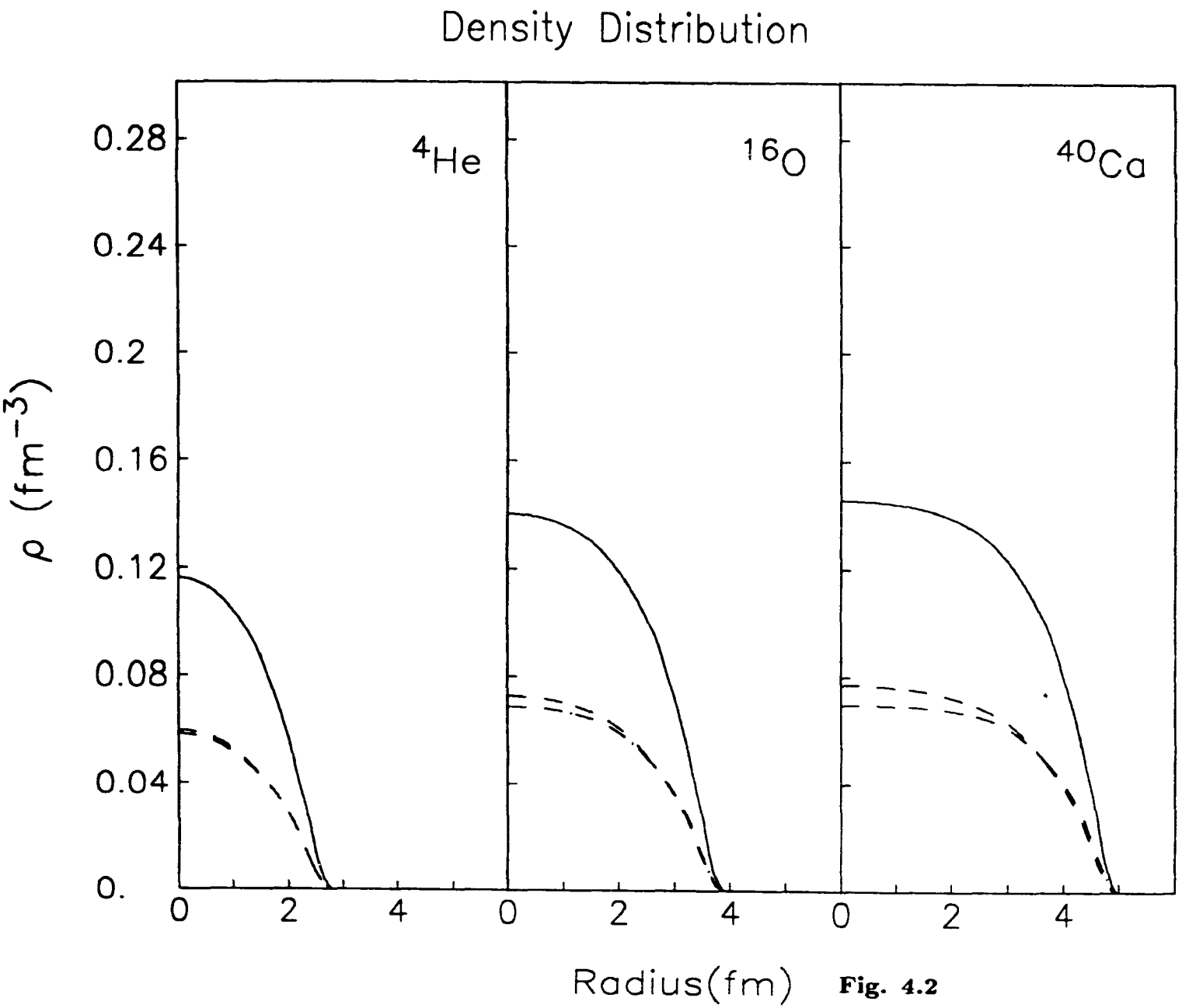
Density Distribution
^{4}He
^{16}O
^{40}Ca
0.28
0.24
0.2
0.16
0.12
0.08
0.04
0.
ρ (fm^{-3})
0
2
4
Radius(fm)

Fig. 4.2

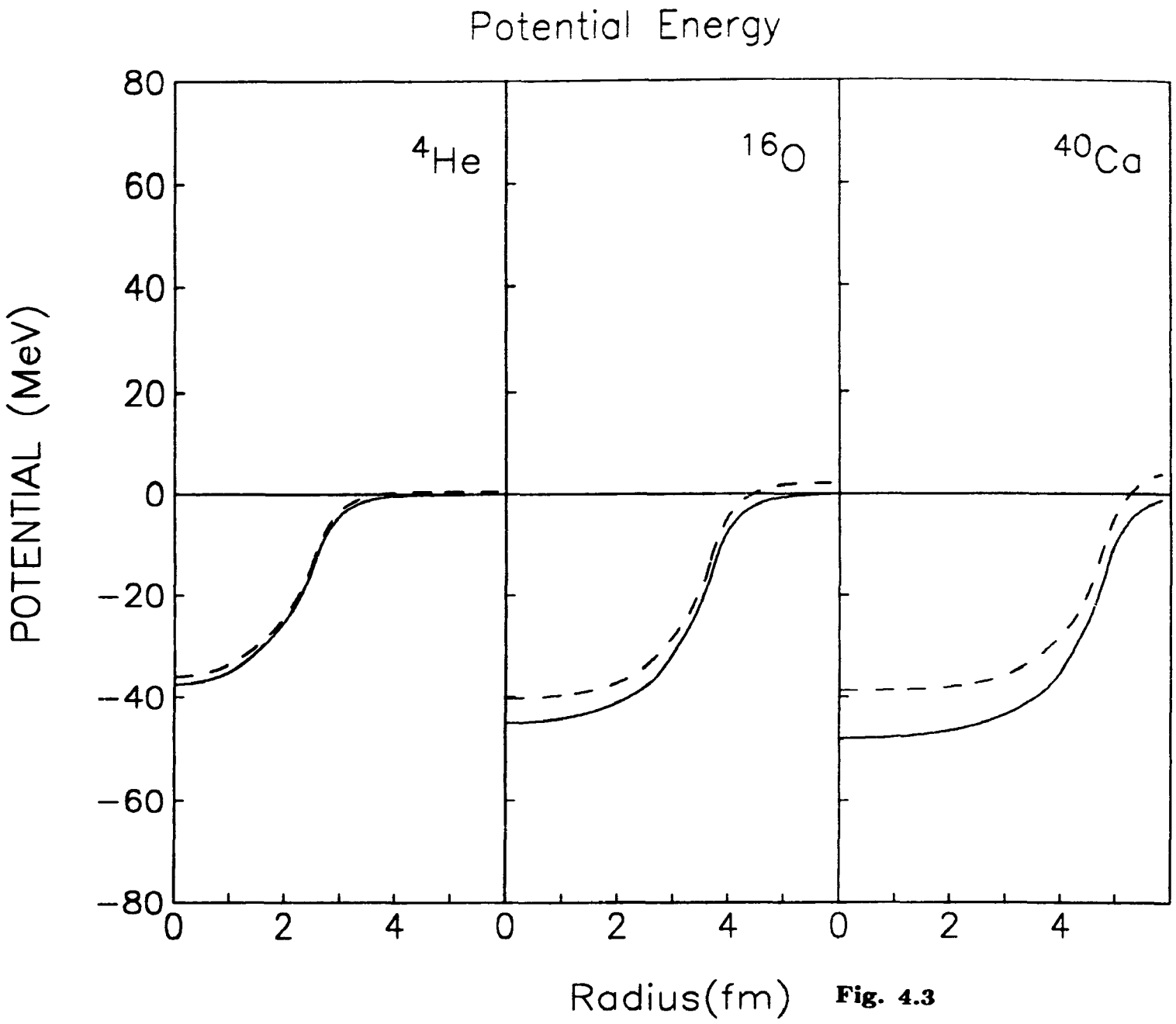
Potential Energy
POTENTIAL (MeV)
80
60
40
20
0
−20
−40
−60
−80
^{4}He
^{16}O
^{40}Ca
0
2
4
0
2
4
0
2
4
Radius(fm)

Fig. 4.3

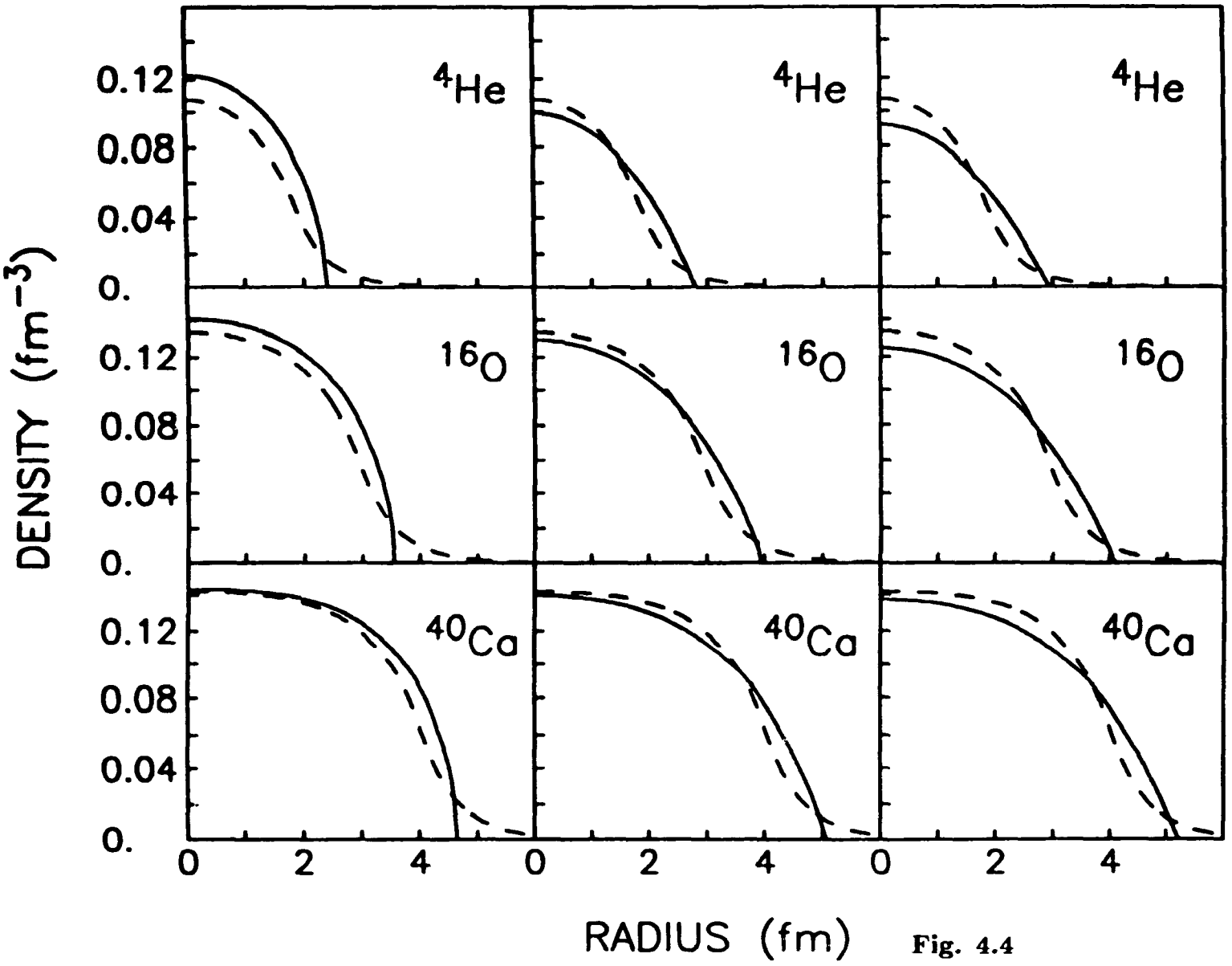

Fig. 4.4

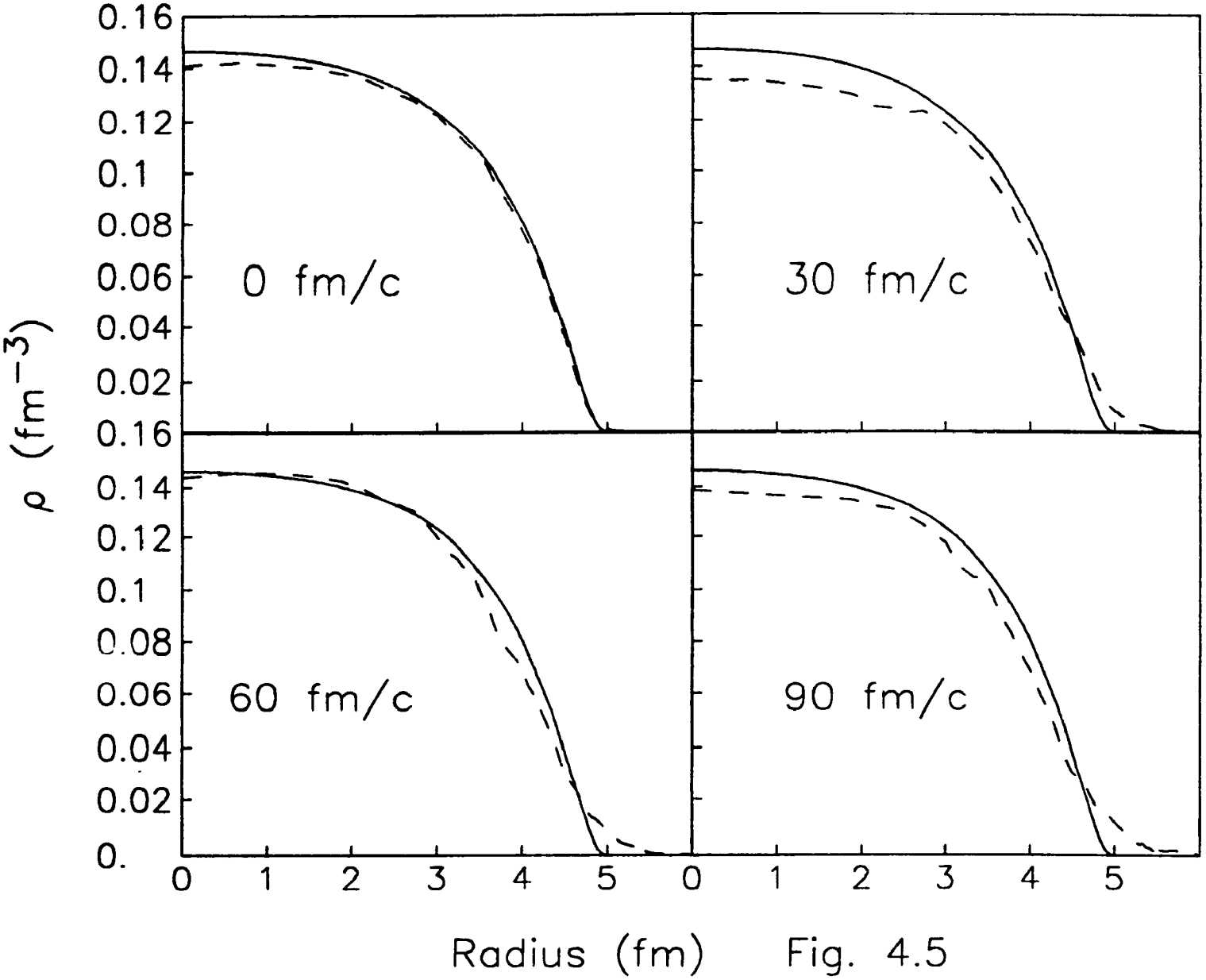
0.16
0.14
0.12
0.1
0.08
0.06
0.04
0.02
0.16
0.14
0.12
0.1
0.08
0.06
0.04
0.02
0.
ρ (fm⁻³)
0 fm/c
30 fm/c
60 fm/c
90 fm/c
0 1 2 3 4 5
0 1 2 3 4 5
Radius (fm)

Fig. 4.5

Table 5 The eigenvalues of the stability matrix (eqn. 5.2.16) for monopole ($\ell = 0$) and multipole ($\ell = 1 - 5$) modes are displayed. These eigenvalues are in units of $MeVfm^3$. First column labels the number of nodes of their corresponding eigenfunctions for each ℓ; a maximum of up to three nodes are shown. The table displays results from three symmetric systems: ^{16}O,^{40}Ca and ^{208}Pb. The eigenvalues of ^{208}Pb for $\ell = 5$ case suffer large numerical error, and they are omitted for this reason.

Table 5

no. of nodes	ℓ=0	1	2	3	4	5
			^{16}O			
0		0.17	37.14	78.80	120.19	158.67
1	239.63	294.47	325.10	349.79	368.80	383.15
2	372.65	407.80	418.98	424.85	428.12	430.07
3	429.18					
			^{40}Ca			
0		−0.11	22.54	50.98	82.04	113.45
1	220.16	286.73	310.21	332.13	351.04	366.69
2	361.10	400.69	413.97	421.68	426.18	428.91
3	427.46					
			^{208}Pb			
0		0.24	8.50	20.18	34.61	
1	168.19	276.30	287.30	300.27	313.89	
2	330.45	372.19	389.29	402.62	412.34	
3	403.72					

Figure Captions: Chapter 5

Fig. 5.1 The eigenfunctions of the stability matrix for ^{40}Ca nucleus corresponding to the lowest (full line) and its next higher (dashed line) eigenvalue are shown. These modes are displayed for ℓ=0, 1 and 2 cases. Dotted lines are the self-consistent densities of ^{40}Ca.

Fig. 5.2 The lowest level eigenfunctions of the stability matrix for $\ell = 2$ (upper curves) and $\ell = 3$ (lower curves) are plotted in full lines. For each case, the results of three symmetric systems are shown. Transition densities of the liquid drop model are shown in dash-dotted lines. The eigenfunctions of the corresponding modes ($\ell = 2$ and 3) from the linearized Vlasov equation (5.3.49) are indistinguishable from those obtained by diagonalizing the stability matrix; this is the case for all three systems shown here. The dotted lines are the self-consistent densities of the nuclei.

Fig. 5.3 The monopole ($\ell = 0$) vibration modes of the stability matrix (full line), scaling model (dash dotted line) and linearized Vlasov equation (dashed line) are compared for three symmetric systems. The dotted lines are again the self-consistent densities of the nuclei.

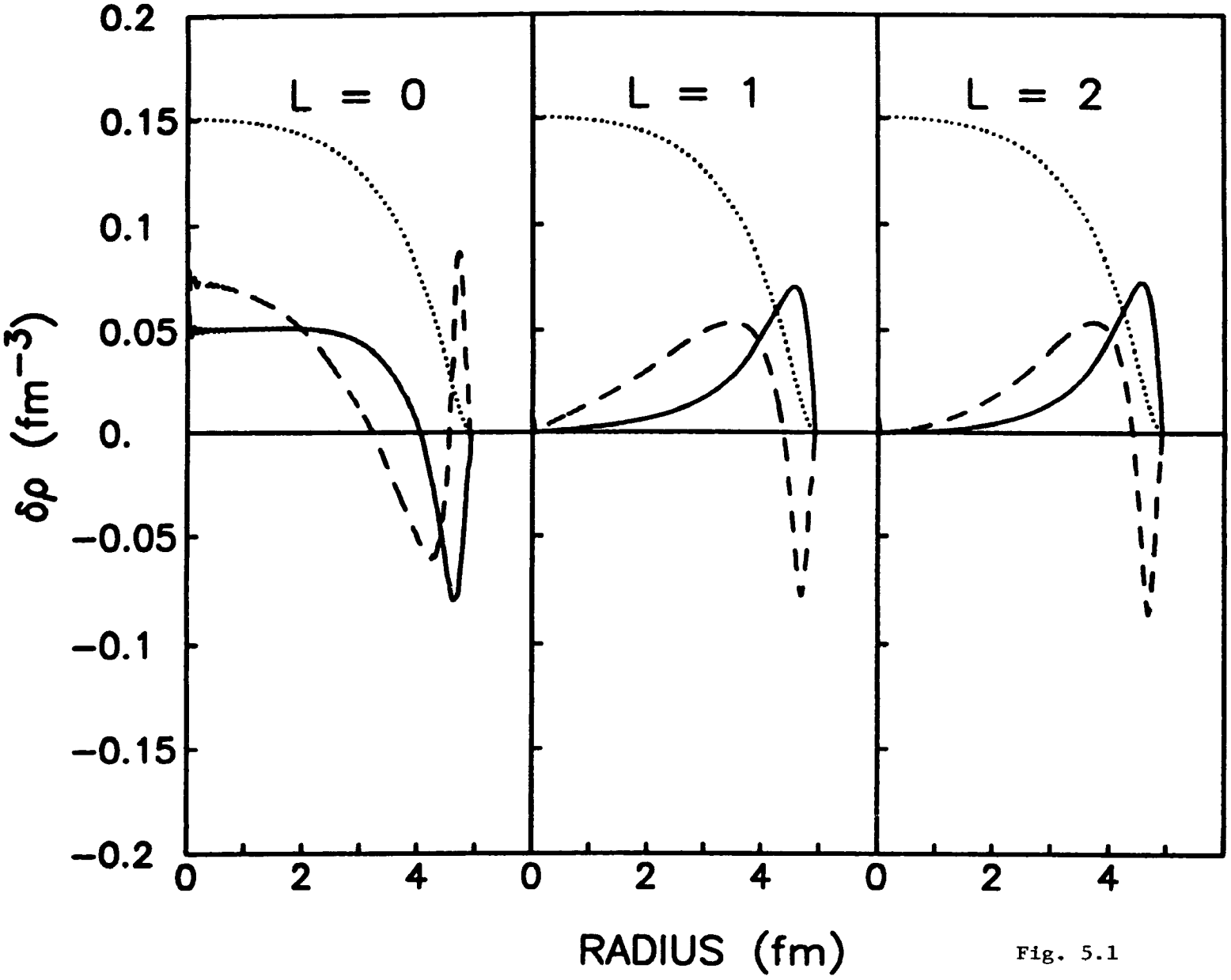

Fig. 5.1

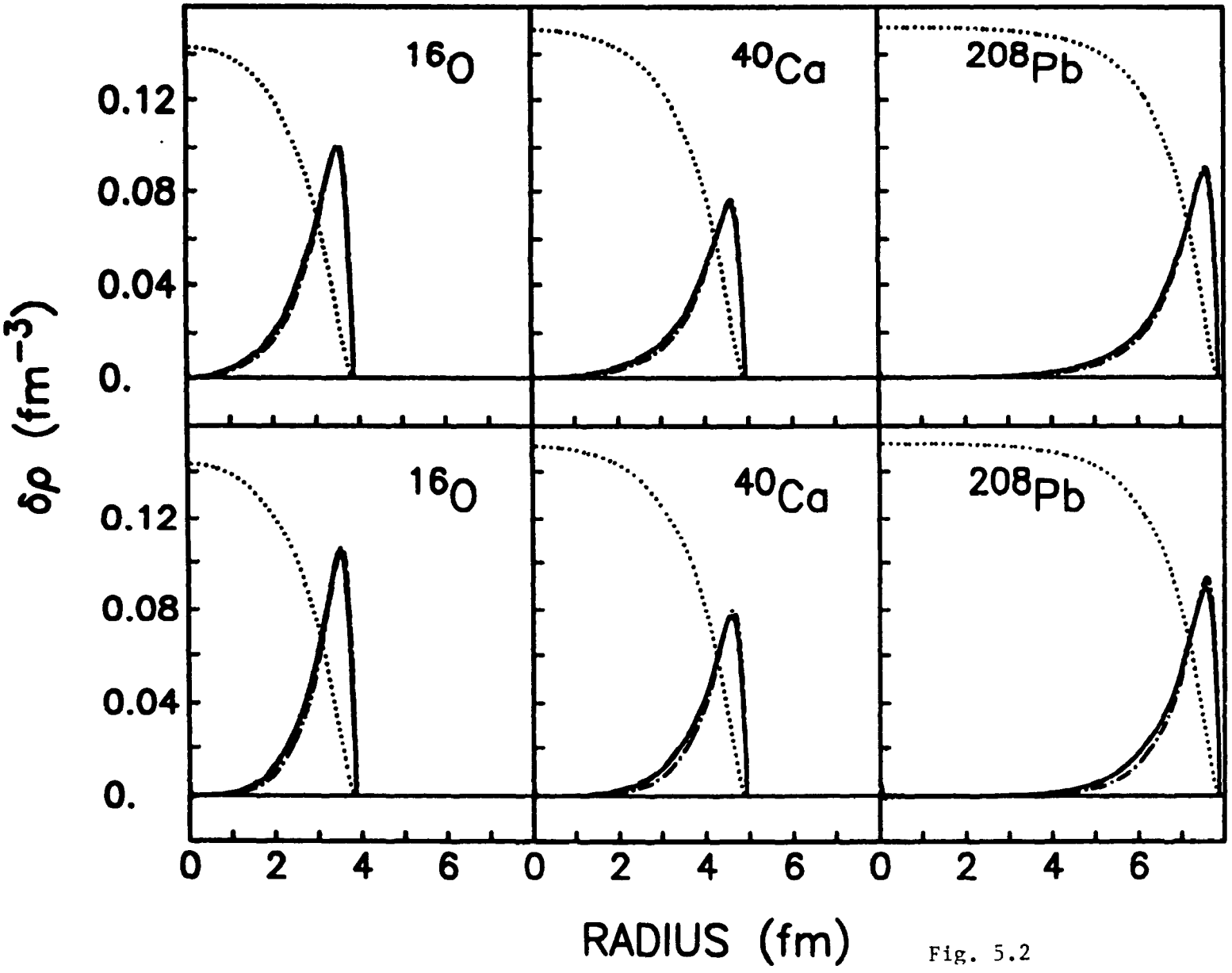
^{16}O
^{40}Ca
^{208}Pb
^{16}O
^{40}Ca
^{208}Pb
0.12
0.08
0.04
0.
0.12
0.08
0.04
0.
$\delta\rho$ (fm^{-3})
0
2
4
6
0
2
4
6
0
2
4
6
RADIUS (fm)

Fig. 5.2

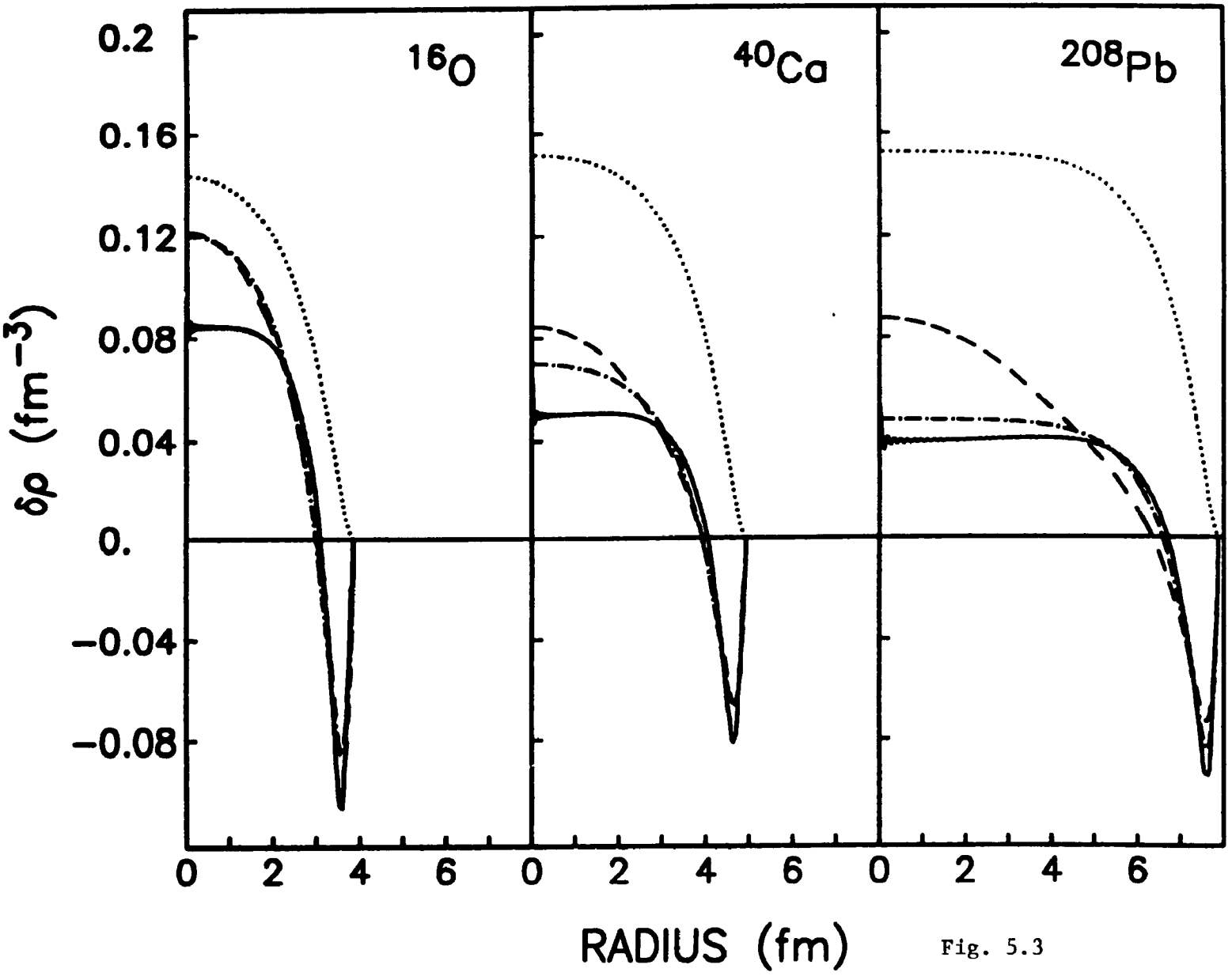
^{16}O
^{40}Ca
^{208}Pb
0.2
0.16
0.12
0.08
0.04
0.
−0.04
−0.08
δρ (fm^{-3})
0
2
4
6
RADIUS (fm)

Fig. 5.3

Figure Captions: Chapter 6

Fig. 6.1 The mass correlation of the projectile-like fragments to the impact parameter for the reaction $^{40}Ar(44MeV/A) +^{27} Al$ is shown. The events here come from the impact paremeter range 5.76-7.76 fm. In this range, the contribution from each impact parameter is correctly weighted. The total number of similations is 110.

Fig. 6.2 Mass distributions of the projectile and target-like fragments are shown. The events shown here are exactly the same as those in Fig. 6.1. The distribution in the middle comes exclusively from the target-like fragments. Very small fragments ($A \leq 5$) are participant clusters. Total number of events is 110.

Fig. 6.3 Angular distribution of the projectile-like fragments of size A = 32-36 is displayed in the histogram. All scattering angles are negative. Events in the histogram comes from 81 simulations after momentum and mass cut. Experimental data are shown as filled circles for A = 34.

Fig. 6.4 The angular distribution of the target-like fragments in coincident with those in Fig. 6.3. Experimental data are shown as filled circles for A = 32.

Fig. 6.5 Angular distribution of the projectile-like fragments as a function of impact parameter. This calculation was performed in the BUU model without the collision cascade.

Fig. 6.6 Correlation between the angles of the target-like fragments and the masses of the projectile-like fragments is shown. No cuts are imposed so they are 110 events in total. Comparison with the experiment should only be made for $M_{PLF} = 32 - 36$ because of the selection of the range of impact parameter (see Fig. 6.1).

Fig. 6.7 Same as in Fig. 6.6 but for correlation between their masses.

Fig. 6.1

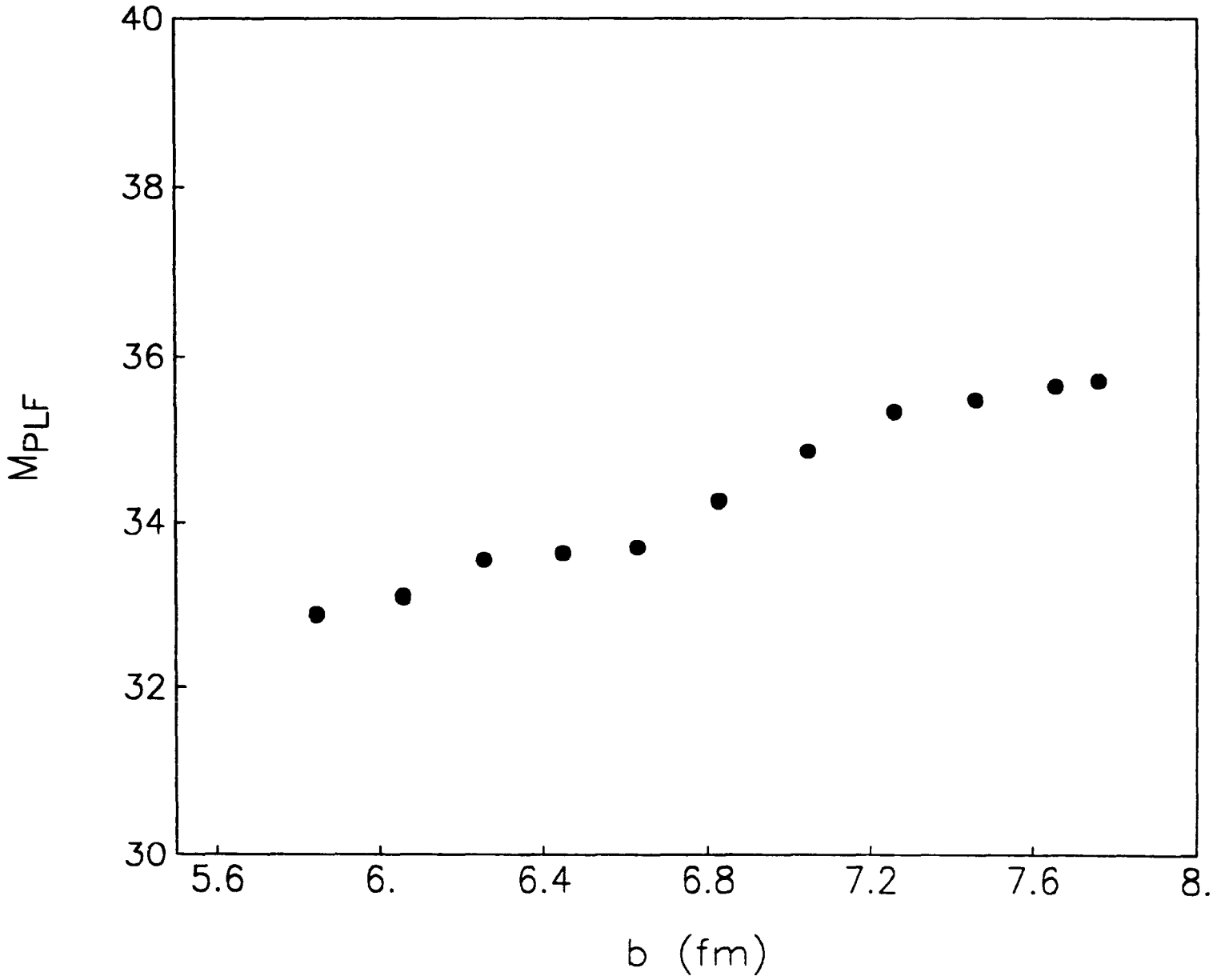

Fig. 6.2

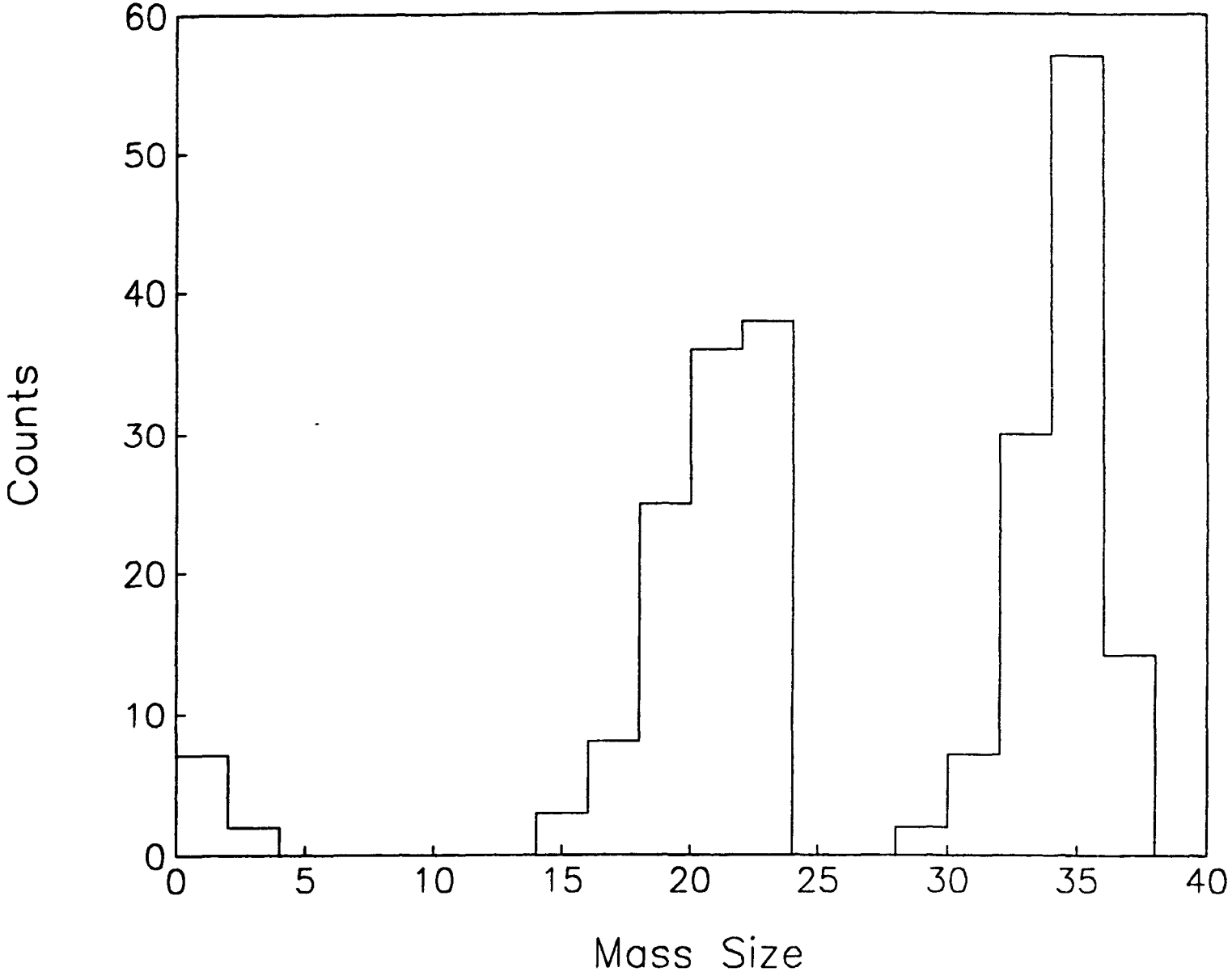

Fig. 6.3

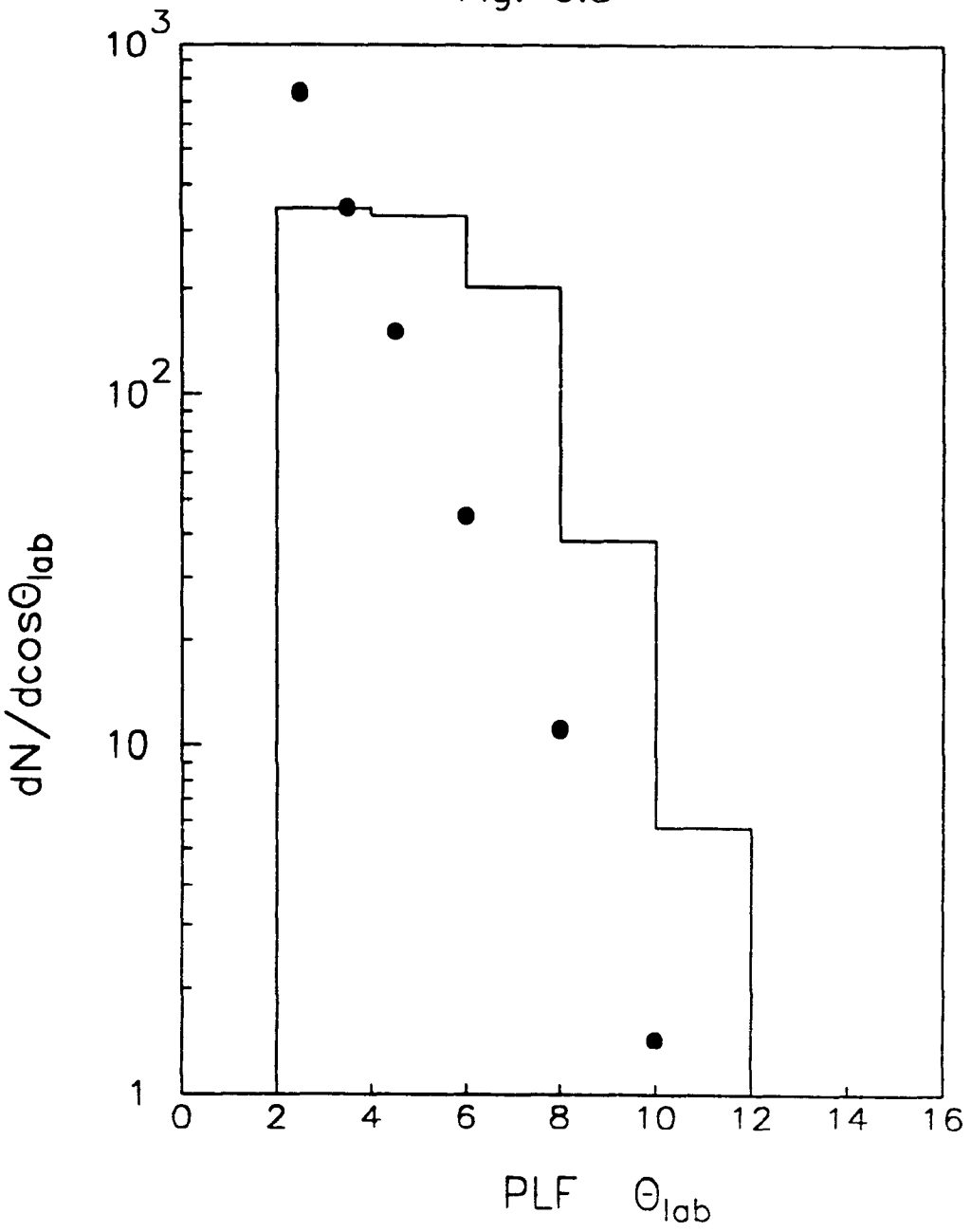

Fig. 6.4

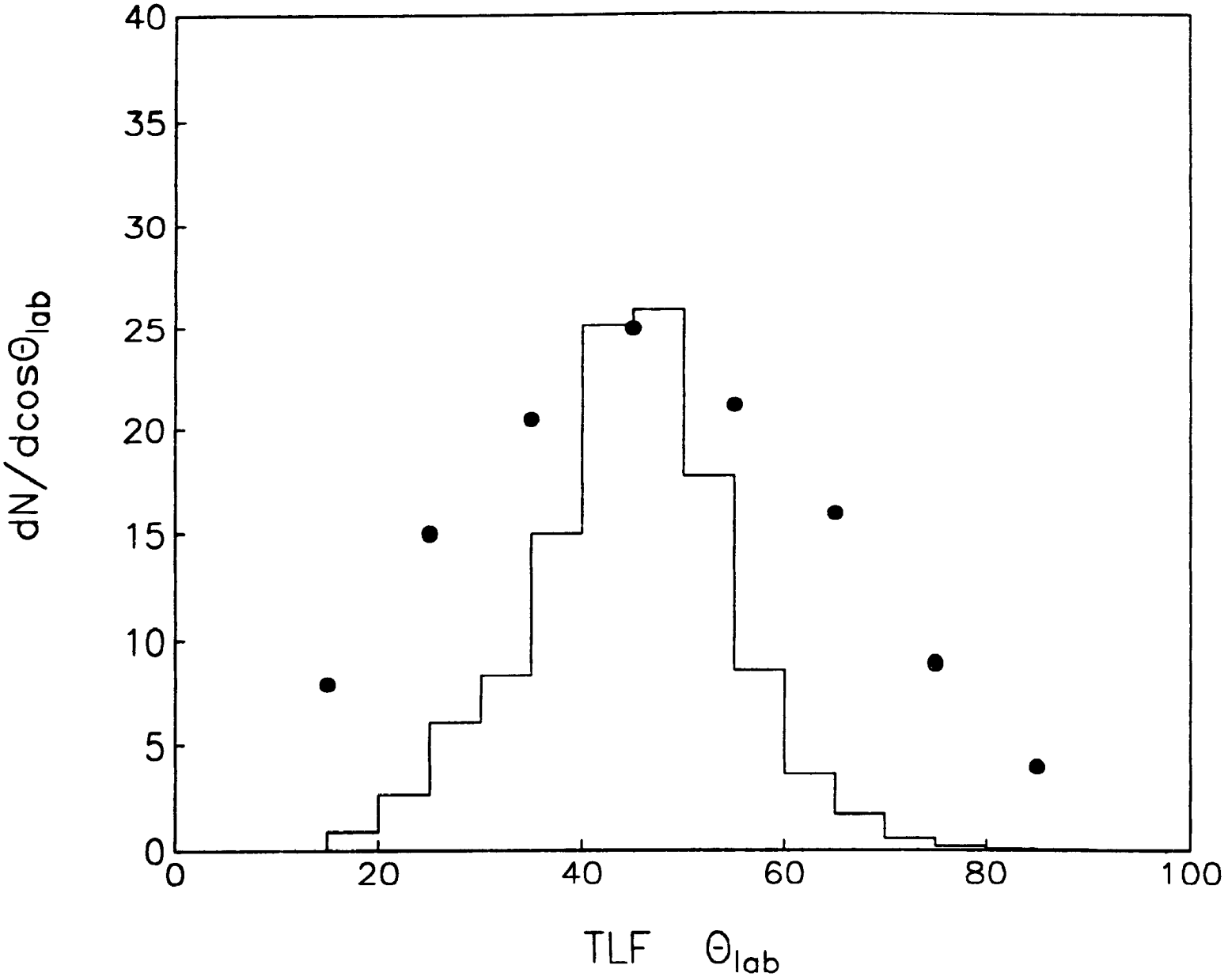

Fig. 6.5

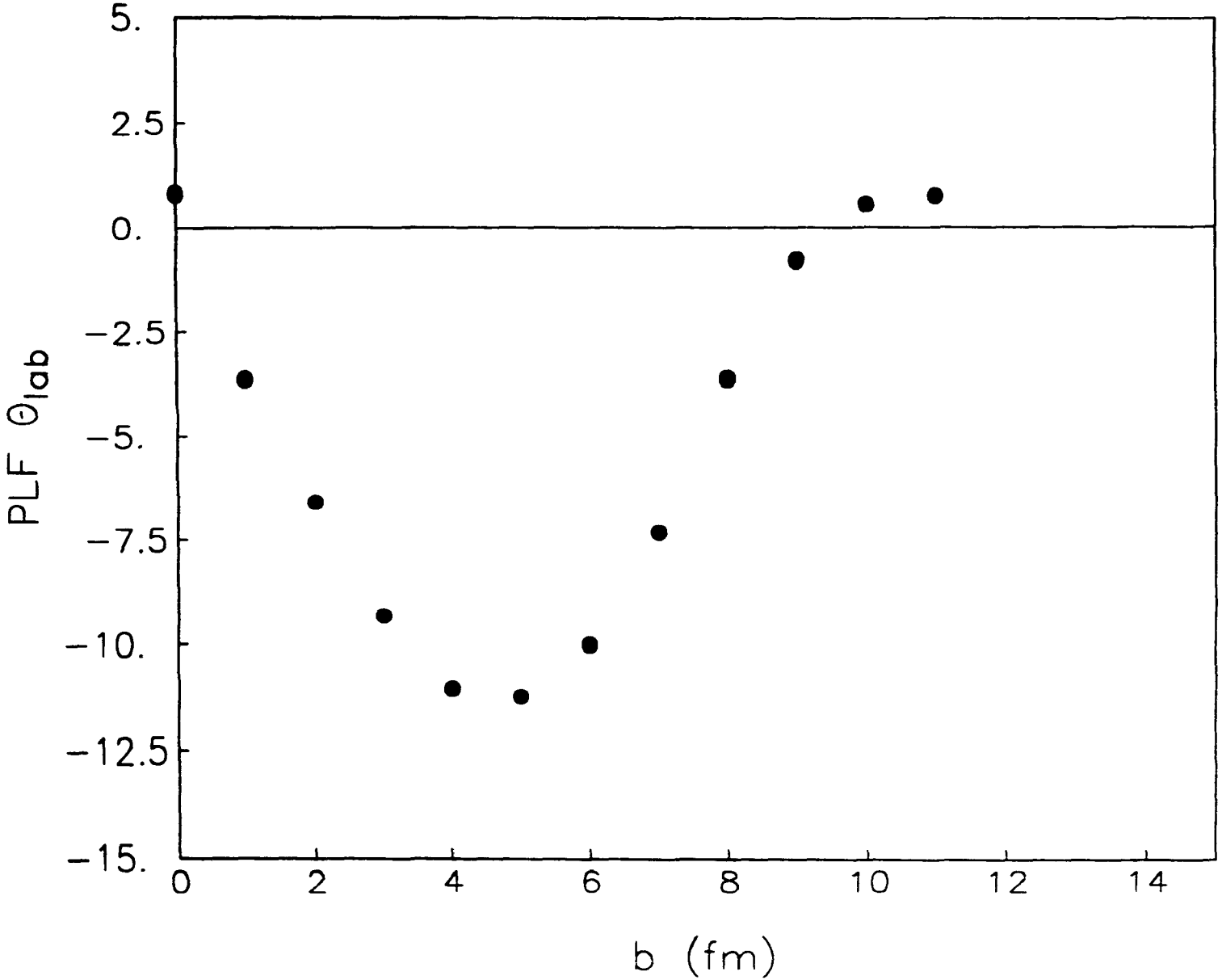

Fig. 6.6

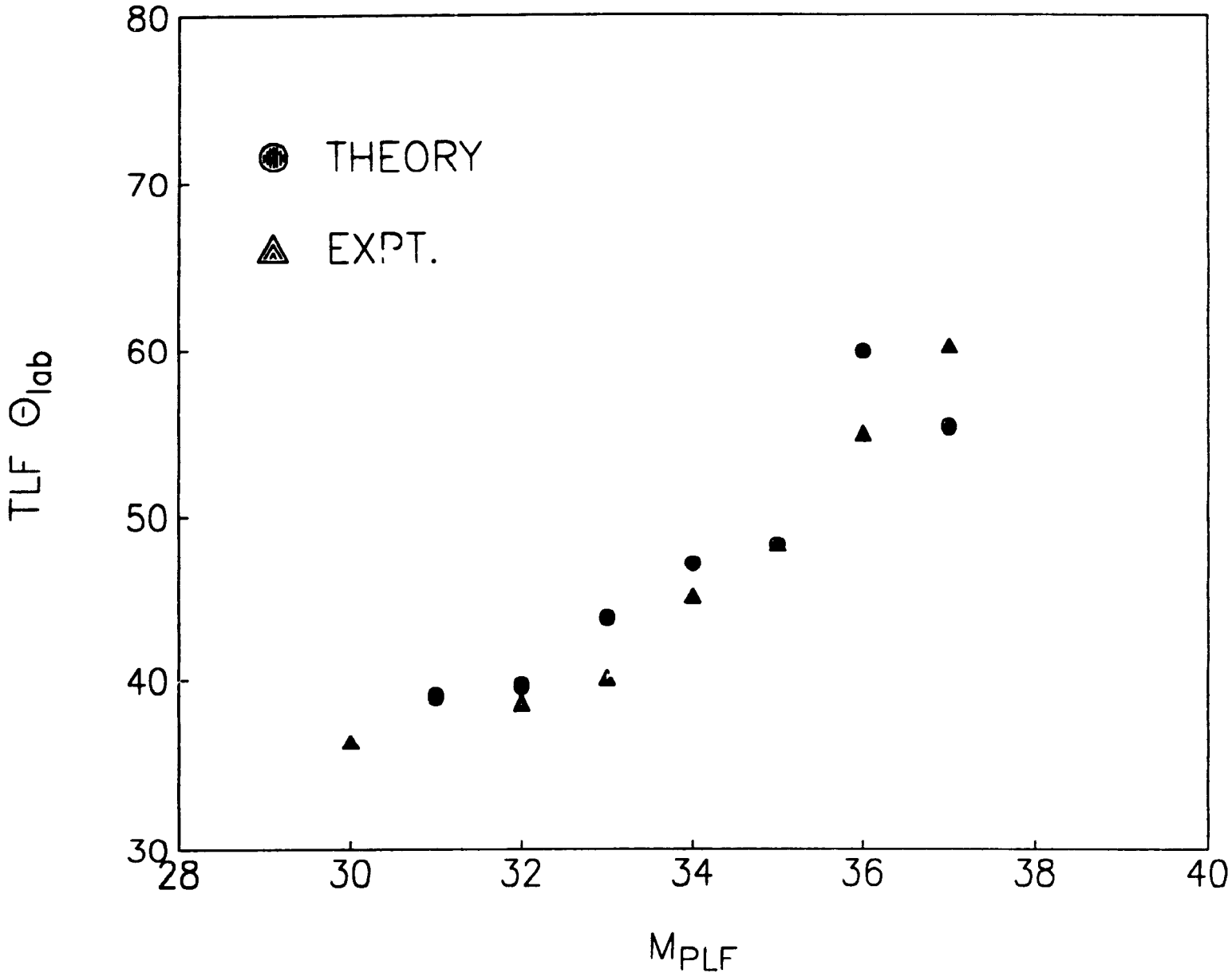
80
70
60
50
40
30
28
30
32
34
36
38
40
THEORY
EXPT.
TLF Θ_{lab}
M_{PLF}

Fig. 6.7

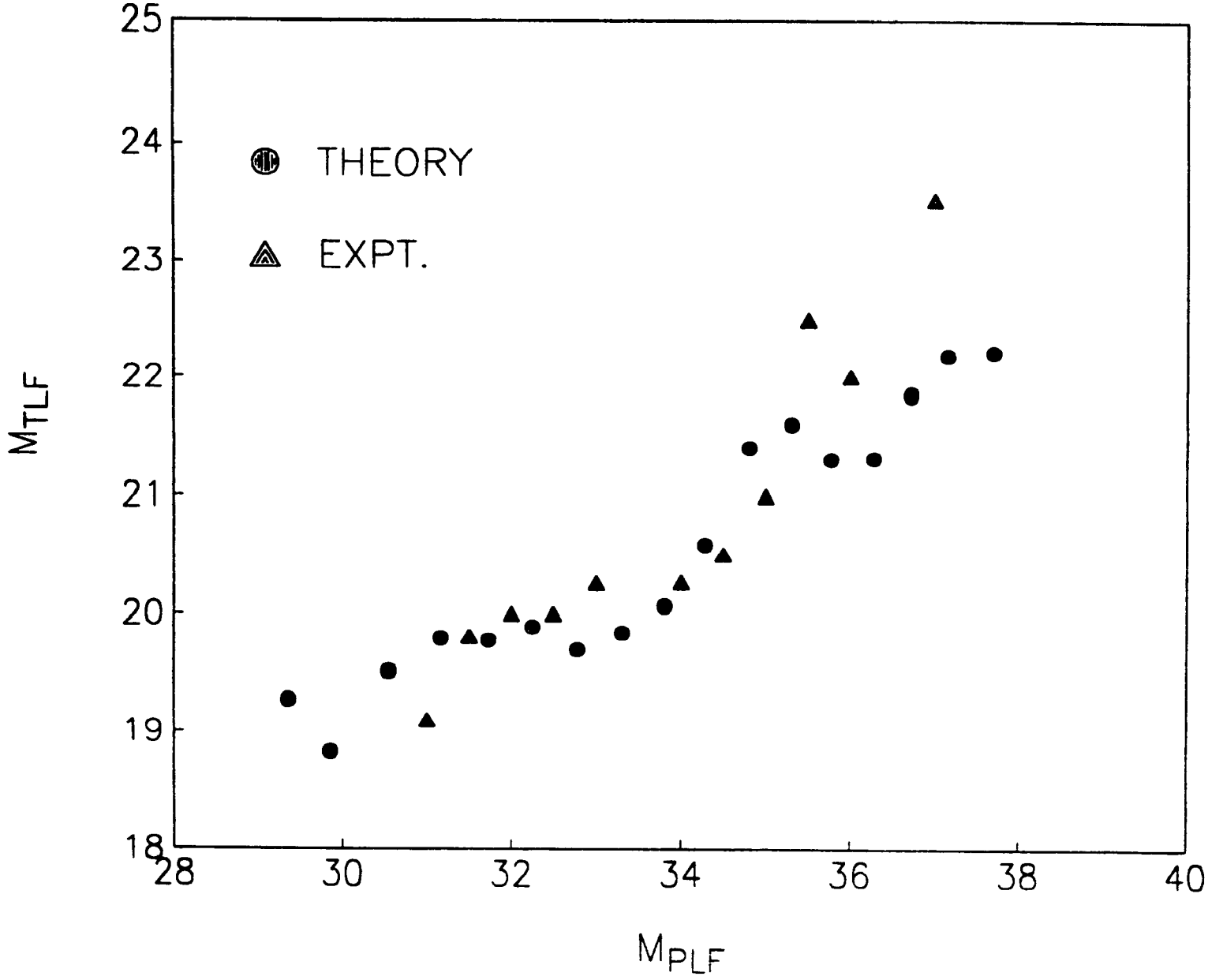

Applications of the extended Boltzmann-Uehling-Uhlenbeck model to participant and spectator dynamics

H. H. Gan, S. J. Lee, and S. Das Gupta
Physics Department, McGill University, Montreal, Quebec, Canada H3A 2T8
(Received 28 May 1987)

The Boltzmann-Uehling-Uhlenbeck model is extended to include fluctuations. The model is then applied to study both spectator and participant physics. The model is capable of providing a unified, parameter-free description of wide-ranging phenomena in intermediate energy heavy-ion collisions.

I. INTRODUCTION

In this paper, we present some results from a model in which at initial time we have two ions approaching each other; at the end the nuclei break up into fragments moving with different velocities. The model is essentially parameter-free in the sense that the ingredients for the calculation are the nuclear mean field and scattering cross sections which are fixed by other data.

The model allows us to examine theoretically many aspects of heavy ion collisions. Experience at Bevalac energy has taught us that for nonzero impact parameters we expect to see spectators which are only mildly perturbed as opposed to participants which are at the seat of violent collisions. As the beam energy decreases such clear distinction ultimately will vanish. Our model allows us to study this transition region. We are able to calculate the velocity distribution of the spectators and their slowing down in a fully microscopic model. Likewise we are also able to study, simultaneously, the fragmentation of the participants. This last topic has become the subject of much study in recent years. The model gives a mass distribution; for reasons to be explained later, quantitative fits, isotope by isotope, are not expected. Nonetheless gross features are expected to emerge. At the very least, the model is useful for understanding the change of dynamics as the beam energy is altered. In the present study we have analyzed ^{20}Ne on ^{20}Ne and ^{40}Ca on ^{40}Ca in the energy range 50–100 MeV/nucleon.

The model is a straightforward generalization of the Boltzmann-Uehling-Uhlenbeck (BUU) model[1,2] which has proven to be very useful in the theoretical analysis of heavy ion collisions.

II. THE EXTENDED BUU MODEL

The work presented here is based on the model reported in Ref. 3 except for some changes. We first need to describe some details of the numerical methods to solve the BUU model before we can explain the modifications needed for the extended version. The mean field is taken to be of the form

$$U(\rho)=[-124(\rho/\rho_0)+70.5(\rho/\rho_0)^2]\ \text{MeV} . \quad (1)$$

The collision cross section between nucleons is taken to be 40 mb,[3] although we have also used energy dependent total cross sections to ascertain if any significant differences would be seen. There were none. In the usual BUU model, the initial phase space density is represented by a large number of test particles. If the nucleus A has nucleon number N_A then we represent the initial phase-space density of this nucleus by $N_A\tilde{N}$ test particles. Similarly the phase-space density of the nucleus B is represented by $N_B\tilde{N}$ test particles. For Ne on Ne we take $\tilde{N}=200$; for Ca on Ca we take $\tilde{N}=100$. Each test particle carries an isospin index. The density is defined in cubes of volume 1 fm^3; $\rho(r)=n/(\delta l)^3\tilde{N}$ where n is the number of test particles in the cube and $\delta l=1$ fm. In the BUU model the test particles propagate in time according to $\dot{\mathbf{p}}(t)=-\nabla_r U$ and $\dot{\mathbf{r}}(t)=\mathbf{p}/m$ except when they collide. This collision cross section is $\sigma_{nn}/\tilde{N}$. The Pauli blocking is checked for each collision. When two test particles collide they change from $(\mathbf{r}_1,\mathbf{p}_1)(\mathbf{r}_2,\mathbf{p}_2)$ to $(\mathbf{r}_1,\mathbf{p}_1')(\mathbf{r}_2,\mathbf{p}_2')$. We build a sphere of radius r around $\mathbf{r}_1$ and radius p around $\mathbf{p}_1'$ such that eight test particles in this phase space volume imply complete filling. Define $f_1=n_1/(8-1)$, where n_1 is the number of test particles not including the test particle at $(\mathbf{r}_1,\mathbf{p}_1')$. Similarly $f_2=n_2/7$. The probability of scattering is taken to be $(1-f_1)(1-f_2)$. For low beam energy we have also sometimes used the following preselection rule. Let $\pm\mathbf{p}_0$ be the beam momentum per particle in the c.m. of colliding ions. In a collision we have $\mathbf{p}_1+\mathbf{p}_2=\mathbf{p}_1'+\mathbf{p}_2'$ and $p_1^2+p_2^2=p_1'^2+p_2'^2$. For 1 and 2 to be thrown out of the two Fermi spheres we need $(\mathbf{p}_1'\pm\mathbf{p}_0)^2\geq p_F^2$ and $(\mathbf{p}_2'\pm\mathbf{p}_0)^2\geq p_F^2$. Using the conservation laws, a necessary (but by no means sufficient) condition for this to happen is

$$(\mathbf{p}_1\pm\mathbf{p}_0)^2+(\mathbf{p}_2\pm\mathbf{p}_0)^2>2p_F^2 .$$

At high energy this is not a good rule as it neglects the depletion in the Fermi sphere, but at low energy we find this is a useful preselection and cuts down on computing. Once the preselection rule is satisfied the test particles are allowed to scatter; afterwards the Pauli blockings for $\mathbf{p}_1'$ and $\mathbf{p}_2'$ are tested by drawing spheres in phase space as described earlier. The numbers of collisions we

find in our calculation are consistent with what has appeared in the literature before.[3,4]

The BUU model treats collisions as a continuous source and will show no fluctuations. In the extended BUU model collision is treated stochastically. The following is the basic prescription. We suppress collisions between two test particles by a factor of $1/\tilde{N}$, but if a collision occurs after the suppression not only do two test particles suffer momenta change but $2(\tilde{N}-1)$ other test particles change momenta also. Physically this corresponds to two actual particles colliding. Suppose two test particles i and j with isospin indices τ_i and τ_j successfully collided and suffered momenta change $\Delta\mathbf{p}$ and $-\Delta\mathbf{p}$. We choose $(\tilde{N}-1)$ test particles with the same isospin τ_i closest to i in phase space and ascribe to all of them the same momentum change $\Delta\mathbf{p}$. This requires defining a distance in phase space. We define

$$d_{ik}^2 \propto (\mathbf{p}_i-\mathbf{p}_k)^2+(p_F/R)^2(\mathbf{r}_i-\mathbf{r}_k)^2 .$$

Here p_F is the Fermi momentum and R the normal radius of the nucleus. The process is repeated for test particles closest to j and they are ascribed a momentum change $-\Delta\mathbf{p}$.

The prescription above conserves total momentum but usually not the total energy. With a slight modification both the total momentum and the total energy can be conserved. We choose $\tilde{N}-1$ particles closest to i as before. Now calculate the average momentum of these particles (including the ith test particle). Call this

$$\langle \mathbf{p}_i \rangle \equiv \left| \sum_{i=1}^{\tilde{N}} \mathbf{p}_i \right| /\tilde{N} ;$$

similarly calculate $\langle \mathbf{p}_j \rangle$. We now recalculate $\Delta\mathbf{p}$ and $-\Delta\mathbf{p}$ from a collision between $\langle \mathbf{p}_i \rangle$ and $\langle \mathbf{p}_j \rangle$. This $\Delta\mathbf{p}$ is now attributed to all the test particles in the ith set and $-\Delta\mathbf{p}$ to all the particles in the jth set. It is easy to verify that this procedure conserves both total momentum and total energy.

We have done calculations both with and without the Coulomb force. We compute $\rho_c(\mathbf{r})$ in 1 fm^3 boxes where $\rho_c(\mathbf{r})$ is the charge density. The Coulomb potential is then obtained from numerical solution of Poisson's equation. The numerical technique is the same as used in time dependent Hartree-Fock (TDHF) calculations[5] except that in our case no symmetry is assumed.

In the beginning of the calculation we have two nuclei approaching each other; the initial phase-space density of each nucleus is modeled to be sharp spheres in configuration and momentum space. For further details, see the Appendix of Ref. 6. At the end one has a few local pockets of density comparable to normal nuclear density against a diffuse background. We interpret such local pockets as clusters. A fragment is defined as the connected volume in space where the density exceeds a certain threshold value (10% of normal nuclear density). The number of nucleons in this connected volume gives the number of nucleons in the cluster. We ignore all clusters where the total nucleon number is less than 0.5. Depending upon the situation, the code is run up to time 80–150 fm/c after the two nuclei initially touch each other. On Vax 785 each run takes 45 min without the Coulomb interaction. Inclusion of the Coulomb interaction approximately doubles this time.

III. SPECTATOR DYNAMICS

For heavy ion collisions at high energy, the participant spectator model proved to be very useful. Consider the collision of two heavy ions at a given impact parameter (Fig. 1). A given part A of one ion will meet a certain part B of the other ion. Now the binding energy per nucleon in nuclei is about 8 MeV. Thus if the energy of collision is high, the fact that A' was attached to A is incidental; A' will fly off after the collision with essentially unchanged velocity. Thus A' can be called the spectator in this collision. Similarly there will be a spectator B' from the other ion. A, however, will hit B. They are the participants. The participants will usually disintegrate, giving rise to many objects.

We do not expect such a clear picture to emerge in the energy range we are considering. Clearly, below a certain beam energy the model of the whole of $(A+A')$ interacting with the whole of $(B+B')$ is more appropriate. An intermediate picture between these two extremes is also possible. Further, the applicability of each model depends not only upon the beam energy but also upon the masses of the colliding ions involved. These complications become important at intermediate impact parameters. We will deal with such situations later. For the moment we turn to more peripheral collisions where one clearly sees spectatorlike fragments. Experimental results for projectilelike spectators in the beam energy of interest here can be found in Refs. 7–9.

Comparison with experimental data requires integration over impact parameters and (depending upon the charges of the ions and the beam energy) inclusion of the Coulomb force in addition to the nuclear force. To be able to discuss the physics easily we will first consider a fixed impact parameter and ignore the Coulomb force.

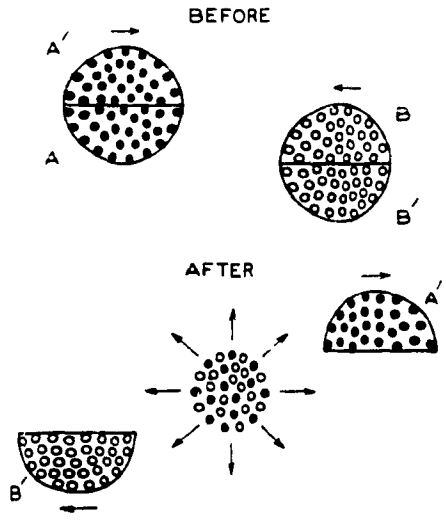

FIG. 1. Participants and spectators. Part A overlaps with part B. They are participants. Parts A' and B' are spectators.

The effect of impact parameter integration and the Coulomb force will be indicated later. We consider Ne on Ne at impact parameter

$$b = R(\sqrt{2/3} + \sqrt{1/3}) = 4.31 \text{ fm}$$

at 100 MeV/nucleon laboratory energy. Here R is the radius of each ion. In a simple geometrical model (Fig. 1) the participants are decided by the geometrical overlap of the two ions; the rest are spectators. There are two spectators; one projectilelike and one targetlike. The number of nucleons in each spectator is predicted to be 16.6 in the geometrical model for this specific b. In a dynamical model one would expect a distribution in mass numbers. The distribution obtained from 21 runs is shown in Fig. 2. Each run produces two pieces of data since we are considering equal ion collisions and we can include both projectilelike and targetlike spectators to increase statistics. The spectators have a distribution of momenta. In the Goldhaber model[10] the width of this momentum spread in the projectile frame is

$$\langle P_{ZK}^2 \rangle = \frac{K(A-K)}{A-1}\sigma_{\eta}^2 . \tag{2}$$

Here A is the mass of the projectile, K is the mass of the spectator, P_{ZK} is the momentum of the spectator in the Z direction in the projectile frame, and $\sigma = \sigma_Z \approx 80$ MeV/c in the high energy situation.

In our case we have a distribution of K values and we find it more convenient to rewrite the above equation

$$\left\langle \frac{K(A-1)}{A-K}(P_{ZK}/K - \overline{P_{ZK}/K})^2 \right\rangle = \sigma_{\eta}^2 . \tag{3}$$

Here $\overline{P_{ZK}/K}$ is the average slowing down in the projectile frame. The Goldhaber model is based solely on counting and thus cannot predict a slowing down. However, this is expected in dynamical models and also seen in experiments. We expect $\overline{P_{ZK}/K}$ to be independent of K but dependent on b, the impact parameter. Hence for this fixed b value we calculate $\overline{P_{ZK}/K}$ from all K values and use this in Eq. (3) to estimate σ_{η}. We find $\sigma_{\eta} \approx 70$ MeV/c. A decrease in the value of σ_{η} at lower energy was predicted on theoretical grounds.[11] The quantity $\overline{P_{ZK}/K}$ is found to be -33 MeV/c compared to the experimental value of -23 MeV/c seen in experiments at 92 MeV/nucleon beam energy.[9] Precise comparison with experiment should not be made at this stage as $\overline{P_{ZK}/K}$ is dependent upon b, the magnitude falling with increasing b.

We digress here temporarily to indicate the numerical accuracy in our calculation. The collision subroutine conserves momenta and energy. The only inaccuracy in our calculations is in solving the Vlasov propagation. This was tested by calculating conserved quantities for an isolated nucleus at time $t = 0$ and $t = 100$ fm/c at which time the majority of our calculations can be stopped. We have also considered more complicated situations where again one can test conserved quantities. Of interest here is the fluctuation in the total momentum in a direction, say y, and the loss in the number of particles due to numerical inaccuracy in the Vlasov propagation. Both of these effects are small, at a less than 5 percent level of the value of the observables we are trying to calculate.

It is likely that the spectators will also have an average transverse momentum. This, of course, is outside the scope of the Goldhaber model. In our calculation we take b to be in the X direction. It is possible for $\overline{P_{YK}/K} \equiv \bar{p}_X$ to be nonzero. Naturally we expect $\bar{p}_y = 0$. This is borne out in our calculations. In the present example we find $\bar{p}_X = -29.4$ MeV/c. (Similar results have been found by Tsang in BUU calculations.[12]) However, the value of $\bar{p}_X$ is a function of both the impact parameter and the energy. For this energy it has a negative value; the magnitude initially grows with impact parameter, reaches a maximum (near $b = 4.31$ fm), and then begins to fall. A net nonzero value of $\bar{p}_Y$ will tend to deviate the spectators away from the forward direction. This would imply that $d\sigma/d\Omega$ maximizes not at 0°, but at some finite angle. Relevant experimental data[7-9] indicate that the maxima, if not at 0°, are between 0° and 2°. We will later show that, at this energy, the Coulomb interaction acts the opposite way and integration over impact parameter will push the maximum of $d\sigma/d\Omega$ to-

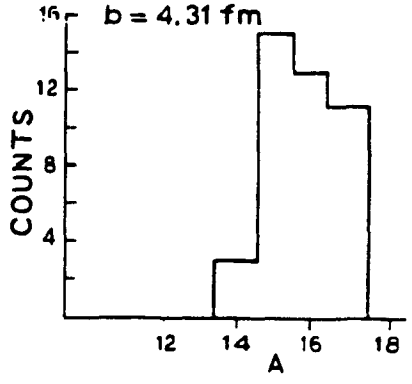

FIG. 2. For Ne on Ne collisions at 100 MeV/nucleon the distribution in masses of the spectators for impact parameter $b = 4.31$ fm. The results from 21 runs are shown. Each run gives two spectators.

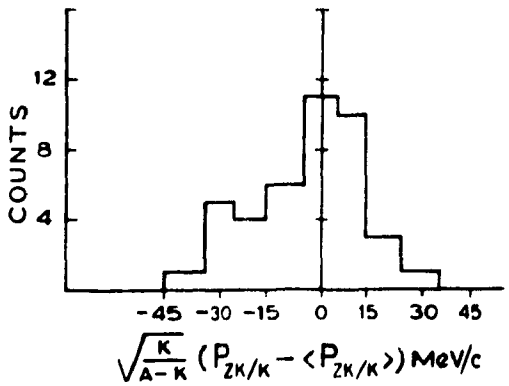

FIG. 3. Distribution of the z component of the momentum of the spectatorlike fragments. The case shown is for Ne on Ne at $b = 4.31$ fm; the beam energy is 100 MeV/nucleon.

wards 0°. For the moment, we will continue discussing this one impact parameter and without the Coulomb force.

A formula similar to Eq. (3) can be used to calculate σ_X^2 and σ_Y^2. In this specific case we verify that $\sigma_X^2 \approx \sigma_Y^2 \approx \sigma_Z^2$. One can test if the momentum distribution is Gaussian,

$$\sigma(P_{ZK}) \propto \exp[-(P_{ZK}-\bar{P}_{ZK})^2/2(\langle P_{ZK}-\bar{P}_{ZK})^2\rangle] \quad (4)$$

A histogram of the distribution seen in the present example is shown in Fig. 3. A Gaussian conjecture appears to be a reasonable approximation, although many more runs are required to establish a shape unambiguously.

Experimentally one usually measures $d^2\sigma/dE\,d\Omega$ for projectilelike fragments at a small angle θ with respect to the beam axis. To calculate this directly in Monte Carlo simulation would take prohibitively long. Instead we extract $\bar{p}_Z$, $\bar{p}_X$, and width from the Monte Carlo simulations and use the Gaussian assumption [Eq. (4)] to compute $d^2\sigma/dE\,d\Omega$. Let θ be the angle the detector makes with respect to the beam axis and $Z-X$ be the plane containing the beam and the detector, then a fragment of momentum $\mathbf{P}_K$ reaching the detector has the following momentum decomposition:

$$\mathbf{P}_K = P_K\cos\theta\hat{Z} + P_K\sin\theta\hat{X} .$$

The cross section for the event is

$$\frac{d^3\sigma}{d^3P_K} \propto \exp[-(\mathbf{P}_K-\bar{P}_{ZK}\hat{Z}-\bar{P}_{\perp K}\hat{n}_\perp)^2/2\sigma_K^2] . \quad (5)$$

In Eq. (5), $\bar{P}_{ZK}$ is the average momentum in the Z direction, $\bar{P}_{\perp K}$ is the average transverse momentum, and $\hat{n}_\perp$ is the direction of the impact parameter which is not known and needs to be averaged. When this is done, Eq. (5) leads to

$$\frac{d^2\sigma}{dE\,d\Omega} \propto E^{1/2}\exp[-(P_K^2+\bar{P}_{ZK}^2+\bar{P}_{\perp K}^2-2P_K\bar{P}_{ZK}\cos\theta)/2\sigma_K^2]\int_0^{2\pi}\exp(2P_K\sin\theta\bar{P}_{\perp A}\cos\theta_1/2\sigma_K^2)\,d\theta_1/2\pi . \quad (6)$$

The last integral in Eq. (6) is the Bessel function $J_0(-iP_K\sin\theta\bar{P}_{\perp K}/\sigma_K^2)$. In our specific example we choose $K=15$; at $\theta=3.5°$ numerical calculation using Eq. (6) gives a full width at half maximum (FWHM) of 143 MeV. This is to be compared with the value ≈ 160 MeV seen in experiments at 85 MeV/nucleon laboratory energy.[8] Again, since impact parameter integration has not been done, 143 MeV is a rough estimate.

We now return to the discussion of a net $\bar{p}_\perp$ in the spectator. If this is large it signifies a measurable deflection away from the forward direction. (We have verified that at higher energy, 200 MeV/nucleon, the effect is negligible.) We have chosen $b=4.31$ fm, where $p_\perp(b)$ due to nuclear forces is about maximum in magnitude. It has a negative value which implies negative angle scattering. A quantitative estimate of the deflection away from the 0 degree can be obtained by plotting a histogram of the spectator angles as obtained in Monte Carlo simulations directly; alternatively we calculate σ_K^2, $\bar{P}_{ZK}$, and $\bar{P}_{\perp A}$ from our simulations, use these values in Eq. (6), and integrate $\int(d^2\sigma/dE\,d\Omega)dE$ to obtain $d\sigma/d\Omega$ as a function of θ. In Fig. 4 we have done both and obtained the results with and without the Coulomb force. The Coulomb force by itself would impart a positive $p_\perp$ and thus, in this example, brings the maximum closer to 0°.

Several other representative calculations were done which lead us to believe that the model can at least semiquantitatively describe spectator dynamics. We can account for the slowing down of the spectators. In experiments the slowing down per particle is the largest for smaller fragments.[7] This is easily explained in the model; the lighter projectilelike fragments originate from lower impact parameter and the mean field is more effective in decelerating the projectile. We have seen that apart from the Coulomb field, the nuclear mean field, can, by itself, impart a transverse momentum. This depends upon the beam energy but also upon the nuclear masses; this has an important effect on the angular distribution. In the future we will make detailed calculations to compare with all the available experimental data[7-9] in this energy range.

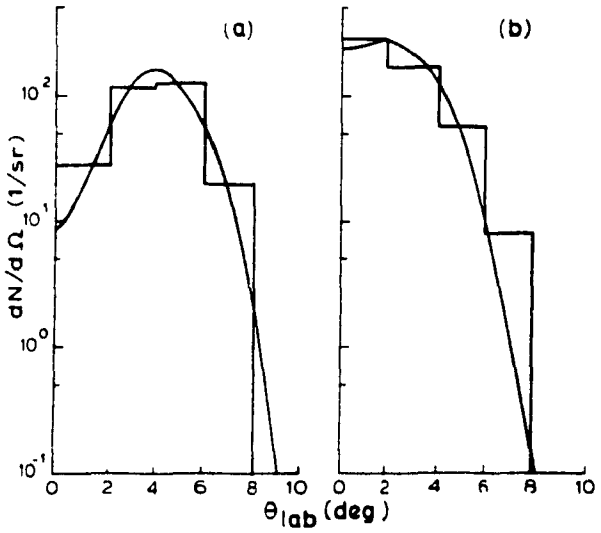

FIG. 4. Distribution in angle for spectatorlike fragments without (a) and with (b) the Coulomb force included. The histograms are obtained by binning the spectator angles as obtained from the runs; the continuous curves are obtained from the Gaussian assumption [Eq. (6)] where the constants σ_K^2, $\bar{P}_{\perp A}$, and $\bar{P}_{ZK}$ are determined from the runs. Here $K=15$.

IV. MASS DISTRIBUTION OF PARTICIPANTS

We now turn to more central collisions and ask the following question: What is the mass distribution of fragments which are not spectatorlike? A variety of approaches have been used to answer this question: microcanonical ensemble simulations,[13-15] the evaporation model,[16] various models of liquid-gas phase transition (see Ref. 17 and references therein), the Cascade-Vlasov approach,[6] and various other models.[18,19]

For central collisions ($b=0$), a mass distribution was obtained in Ref. 3 for Ne on Ne collision at 100 MeV/nucleon in a calculation very similar to the present one. To be able to compare with experimental data we need to integrate over impact parameter. We would also like to see how the theoretical predictions change as the beam energy is varied.

Figure 5 shows our results for Ca on Ca collision at 92 MeV/nucleon. Thirty runs spanning the impact parameter $b=0$ to 4.2 fm were taken. To reduce statistical fluctuations, the results have been averaged over 3 mass units for each bin. Figure 5 gives the histogram of all the clusters and also a filtered histogram where we remove spectatorlike fragments. We use the following criterion: In the c.m. of the colliding ions, the initial momentum per particle in each ion is $\pm p_Z$. After the collision if the absolute value of the Z component of the momentum per particle in the cluster is $> 0.6p_Z$ in the c.m., we leave them out. This means (a) we rule out those projectilelike fragments whose Z component of momentum per particle in the laboratory is greater than $0.8(p_Z)_{\text{lab}}$, and (b) we rule out targetlike spectators which are slowly moving in the lab. For this beam energy this amounts to ruling out targetlike spectators whose kinetic energy in the laboratory is less than ($3.65A$ MeV), where A is the number of nucleons in the cluster.

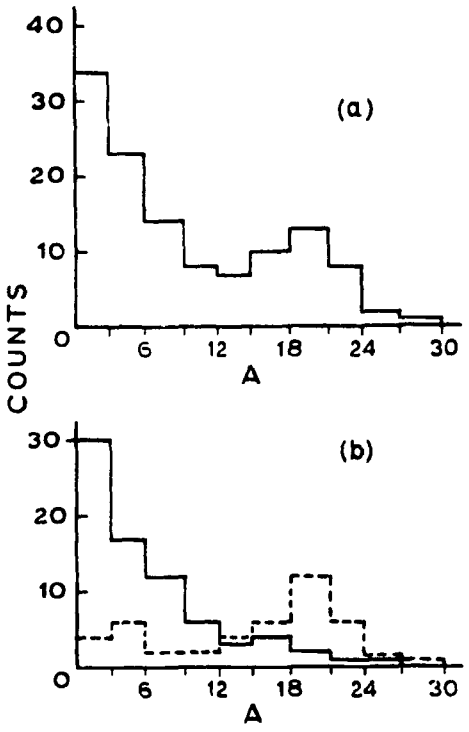

FIG. 5. Mass distributions for Ca on Ca collisions at 92 MeV/nucleon. This is the result from 30 runs spanning the impact parameter b from 0 to 4.2 fm; the top curve (a) includes all clusters; in (b) we separate out contributions from participants (solid line) and spectators (dashed line); for the latter a cut in the momentum of the fragments in the c.m. of the colliding ions is imposed for the distinction. The yield $Y(A)$ given by the solid curve in (b) falls off slower than what is seen in experiment (Ref. 20).

In our calculation (Fig. 5), we see that the yield $Y(A)$ from participants falls off with A with some leveling occurring around $A \approx 12$. There are some recent data obtained in experiments of Ar on Ca at 92 MeV/nucleon.[20] The falloff seen in experiments is faster than what the calculation gives. If we constrain ourselves to fit both the experimental data and the theoretical calculation by a power law $Y(A) \approx A^{-\tau}$, then experiment gives $\tau \approx 3.0$, whereas theory gives $\tau \approx 1.5$. Experimental data do not go beyond $A=12$, but there is some indication of the cross section flattening out around $A \approx 10$. The main failure of the model therefore is that the initial falloff is too slow.

Figure 6 shows results of a similar calculation for Ne on Ne at 100 MeV/nucleon. Here 25 runs spanning $b=0$ to 3.9 fm were taken. In the data shown in Fig. 6 the Coulomb interaction is included; however, for fragmentation of Ca on Ca or Ne on Ne, the Coulomb interaction is unimportant. Remembering that in the latter case the total number of nucleons is half compared to the case for Ca on Ca, the mass distribution in the case of Ne on Ne is similar to that of Ca on Ca.

The model fails at low beam energy. At high energy, the two nuclei, upon impact, quickly break up and nu-

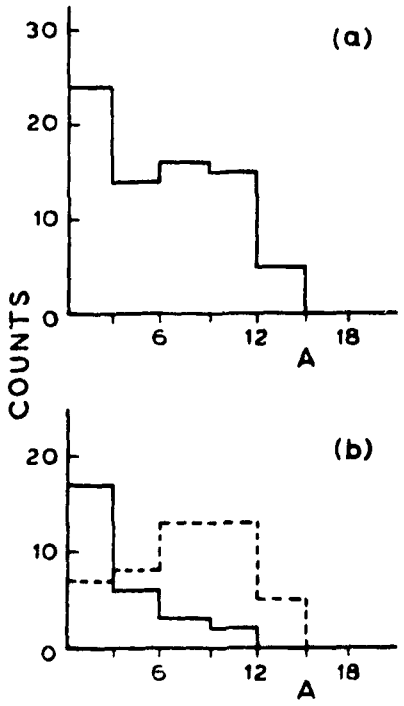

FIG. 6. Same as in Fig 5 except that we consider Ne on Ne at 100 MeV/nucleon.

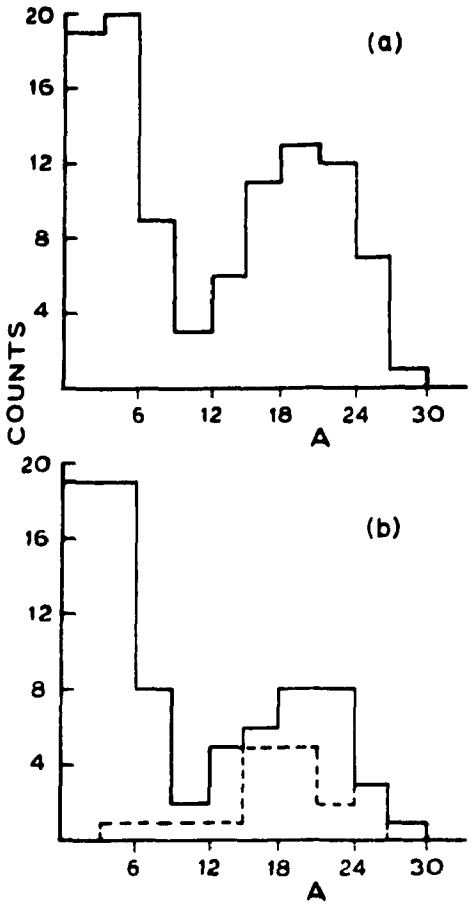

FIG. 7 Same as in Fig. 5 except that this is for Ca on Ca at 72 MeV/nucleon. Note that the yield $Y(A)$ vs A for the participantlike fragments [solid curve in (b)] shows a minimum around $A \approx 12$.

cleons which are close together in phase space will remain bound to produce clusters. At low beam energy the scenario is different; energy is dumped into a region of configuration space but it is not enough to break up the system quickly. Consequently, other processes like evaporation, which cannot be accommodated in the present framework, will become a major mechanism in deciding the mass distribution. A beam energy of 50 MeV/nucleon is already too low for this model.

Figure 7 shows our calculation for Ca on Ca at 72 MeV/nucleon. We have no reason to believe that at this energy the model will break down qualitatively. The most noticeable feature is the U shape of the reaction cross section as a function of A. This shape remains after one removes from the histogram spectatorlike fragments. Recent experimental data[20] have not established this increase of $Y(A)$ vs A beyond $A \approx 12$, but there is at least a hint of this occurring in the experiment[20] of Ar on Ca at 42 MeV/nucleon. Unfortunately the data do not go beyond $A = 12$; for equal ion collisions data up to $A \approx 24$ would be a very useful test of the model.

V. SUMMARY AND DISCUSSION

The extended BUU model is a direct generalization of the BUU model which has become a very useful theoretical tool for intermediate energy heavy ion collisions. We therefore felt that it is important to test the predictive power of the extended BUU model. It is a parameter-free model which addresses a very complex problem. It is gratifying to see that the main features of spectator physics come out rather well from the model. In future work we will include the diffuseness of the surface carefully, as one expects this to play a significant role for precise comparison with experiments. Our present treatment does not treat the surface properly. This is related with the larger problem of treating the surface in the Vlasov prescription. For mass distributions in more central collisions between equal ions, the most interesting prediction is that we expect to see a minimum in the $Y(A)$ vs A curve. This should happen between 50 and 100 MeV/nucleon beam energy.

Note added. The average properties of spectators can be studied in the standard BUU model. Recent work can be found in Refs. 21 and 22. We thank C. Grégoire for bringing this to our attention.

ACKNOWLEDGMENTS

S. Das Gupta acknowledges many discussions with G. F. Bertsch. This work was supported in part by NSERC and in part by the Quebec Department of Education.

[1]G. F. Bertsch, H. Kruse, and S. Das Gupta, Phys. Rev. C **29**, 673 (1984).
[2]H. Kruse, B. V. Jacak, and H. Stocker, Phys. Rev. Lett. **54**, 289 (1985).
[3]W. Bauer, G. F. Bertsch, and S. Das Gupta, Phys. Rev. Lett. **58**, 863 (1987).
[4]J. Aichelin and G. F. Bertsch, Phys. Rev. C **31**, 1730 (1985).
[5]S. E. Koonin, K. T. R. Davies, V. Maruhn Rezwani, H. Feldmeier, S. J. Krieger, and J. W. Negele, Phys. Rev. C **15**, 1359 (1977).
[6]S. Das Gupta, C. Gale, J. Gallego, H. H. Gan, and R. D. Ratna Raju, Phys. Rev. C **35**, 556 (1987).
[7]R. Dayras *et al.*, Nucl. Phys. **A460**, 299 (1986).
[8]C. Guet, Nucl. Phys. **A400**, 191C (1983).
[9]K. Van Bibber *et al.*, Phys. Rev. Lett. **43**, 840 (1979).
[10]A. S. Goldhaber, Phys. Lett. **53B**, 306 (1974).
[11]G. F. Bertsch, Phys. Rev. Lett. **46**, 472 (1981).
[12]M. B. Tsang, Nucl. Phys. (to be published).
[13]G. Fai and J. Randrup, Nucl. Phys. **A381**, 557 (1982).
[14]S. E. Koonin and J. Randrup, submitted to Nucl. Phys.
[15]D. H. E. Gross, Nucl. Phys. (to be published).
[16]W. A. Friedman and W. G. Lynch, Phys. Rev. C **28**, 950 (1983).
[17]L. P. Csernai and J. I. Kapusta, Phys. Rep. **131** 224 (1986).
[18]J. Aichelin and H. Stoecker, Phys. Lett. B **176**, 14 (1986).
[19]G. E. Beauvais, D. H. Boal, and J. C. K. Wong, Phys. Rev. C **35**, 545 (1987).
[20]B. V. Jacak *et al.*, Phys. Rev. C **35**, 1751 (1987).
[21]C. Grégoire, B. Rémaud, F. Sébille, and L. Vinet, Phys. Lett. B **186**, 14 (1987).
[22]A. Bonasera, M. di Toro, and C. Grégoire, Nucl. Phys. **A463**, 653 (1987).